Aspects and Implementations for Accelerating Image Acquisition in Microscopy

Inauguraldissertation
zur Erlangung des akademischen Grades
eines Doktors der Naturwissenschaften
der Universität Mannheim

vorgelegt von

Dipl.-Inf. Eike Slogsnat
aus Heidelberg

Mannheim, 2012

Dekan: Prof. Dr. Heinz Jürgen Müller, Universität Mannheim
Referent: Prof. Dr. Karl-Heinz Brenner, Universität Heidelberg
Korreferent: Prof. Dr. Cornelia Denz, Universität Münster

Tag der mündlichen Prüfung: 6. Mai 2013

Abstract

Subject of this thesis is to shorten the execution time of biological experiments which are performed with fluorescence microscopy. Especially when genome-wide screens are run, a huge amount of prepared cells has to be observed. Therefore, speeding up the image acquisition will have the strongest impact on the time which is needed to execute the experiments. The approaches presented here are the elimination of the time-consuming focus search, and two parallel microscope systems, one with standard macro-optics and spectral-parallelization and the other one with highly miniaturized optical components arranged in an array for fast-scanning microscopy.

Zusammenfassung

Thema dieser Arbeit ist die Verkürzung der Ausführungszeit biologischer Experimente, die mit Hilfe der Fluoreszenzmikroskopie vollzogen werden. Besonders bei der Durchführung genomweiter Experimente muss eine sehr große Anzahl präparierter Zellen untersucht werden. Daher wird eine beschleunigte Bildaufnahme die stärkste Auswirkung auf die Zeit haben, die benötigt wird, um die Experimente auszuführen. Die hier präsentierten Ansätze sind: die Eliminierung der zeitintensiven Fokussuche sowie zwei parallele Mikroskope – eines mit Standard-Makrooptiken und spektraler Parallelisierung und das andere mit hochgradig miniaturisierten optischen Komponenten, arrangiert in einem Array, für schnell scannende Mikroskopie.

Contents

Introduction and Overview

Fluorescence microscopy is a key technology in biology. It enables the study of different parts of fixed or living cells with a high signal-to-noise ratio as the fluorescent molecules – bound to different functional components in the cell – are the only source of light. A lot of effort has been put in the development of specialized and more efficient fluorophores. Its impact on scientific research can clearly be seen by the awarding of the Nobel prize in chemistry for the discovery and the development of the green fluorescent protein (GFP) in the year 2008.

In the field of optical technology new high resolution microscopy methods were developed in the past decades. These include the 4Pi microscope and the stimulated-emission-depletion microscope (STED). The 4Pi microscope is a confocal fluorescent microscope, where two opposing objectives are used to illuminate the object and collect the fluorescence light from both sides [Hell et al. 1992], thus enhancing the axial resolution to $\sim 100nm$ [Egner et al. 2002]. The STED microscope uses a doughnut-shaped spot to deplete the outer regions of the excitation spot. By this procedure particles with a distance of $65nm$ can be resolved [Klar et al. 2001]. By combining these two methods spherical focal spots of $40 - 45nm$ in diameter were reached [Schmidt et al. 2008].

Another important performance parameter is the acceleration of the image acquisition. In systems biology a multitude of single experiments have to be observed, especially when a genome-wide screen is run [Simpson, Joggerst, et al. 2012]. And when performing time-lapse screens [Neumann et al. 2006], the time needed for the image acquisition becomes even more important, as the time between the repeated observation of one experiment should be small. The demand for speeding up microscopy leads to automated high-content screening platforms, which use standard automated wide-field microscopes with one objective lens [Simpson, Cetin, et al. 2007].

Three approaches to accelerate the image acquisition are presented in this thesis. In the first part, a method to eliminate the time-consuming focus search is introduced. The second and third part cover the possibility of accelerating microscopy by parallelizing the image acquisition on one substrate. In the second part, off-the-shelf macro-optic components were used to build a system capable of taking pictures of four fluorophores at the same point in time, whereas a miniaturized parallel fluorescence microscope using micro-optic components is presented in the third part.

Part I.

Elimination of the Focus Search in Microscopy

1. Deflectometry

1.1. Introduction

In conventional microscopes cover glasses are used to flatten the samples, to hold them in place and to prevent them from drying-out. These cover glasses typically have a thickness between $100\mu m$ and $200\mu m$. Objective lenses are corrected to compensate the aberrations which are introduced by this additional glass layer. In inverted microscopes, which are commonly used in biology, the observed objects lie on the cover glass and the objective lens is located underneath. Due to this setup and the thinness the glass layer is bent. These deformations typically are 50 to 100 times larger than the depth of field, thus it is necessary to search the focus at every individual position on the substrate. This focusing step is the most time-consuming factor in microscopy.

One possibility of avoiding the focus search is to switch to thick glass layers, but as standard objective lenses are optimized for the use of thin cover glasses this would require new designs of the objective lenses. Therefore a deflectometric method was developed to determine the height deviations of the sample substrates, thus eliminating the focus search. Considering that the focal search can last seconds the data throughput could be enhanced significantly by this approach.

1.2. Principle of Deflectometric Measurement

In deflectometry, the normals and thus the slopes of a specular surface can be measured by observing a regular known pattern reflected from the surface (Figure 1.1).

If the light ray $\mathbf{s}_1$ from the pattern and the light ray $\mathbf{s}_2$ to the observation is known, the normal at the incident point (x, y) on the surface can be calculated by:

$$\mathbf{N}(x, y) = \frac{\mathbf{s}_2 - \mathbf{s}_1}{|\mathbf{s}_2 - \mathbf{s}_1|} \tag{1.1}$$

Once the normal is known the gradient at this position is determined by (see 1.7.3 for the derivation):

$$\vec{\nabla} h(x, y) = -\frac{1}{N_z(x, y)} \begin{pmatrix} N_x(x, y) \\ N_y(x, y) \end{pmatrix} \tag{1.2}$$

The height distribution $h(x, y)$ is then computed by integrating the gradients.

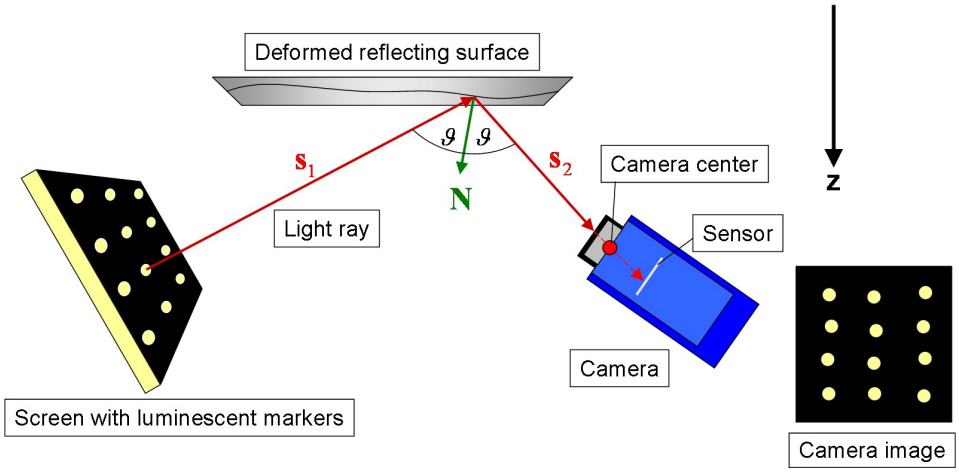

Figure 1.1.: Schematic deflectometry setup

1.3. Ambiguity of Normal Determination

In general deflectometric methods which use a scattering pattern are subject to an ambiguity regarding the determination of the surface normals. This is due to the fact that the camera ray $\mathbf{s}_2$ is known, but the ray $\mathbf{s}_1$ from the pattern is ambiguous.

Assuming that the position of one point in the pattern is found in the sensor plane, the corresponding camera ray can directly be calculated. Back-tracing this ray yields many possible surfaces - and therefore normals - which reflect the pattern point into the camera (Figure 1.2).

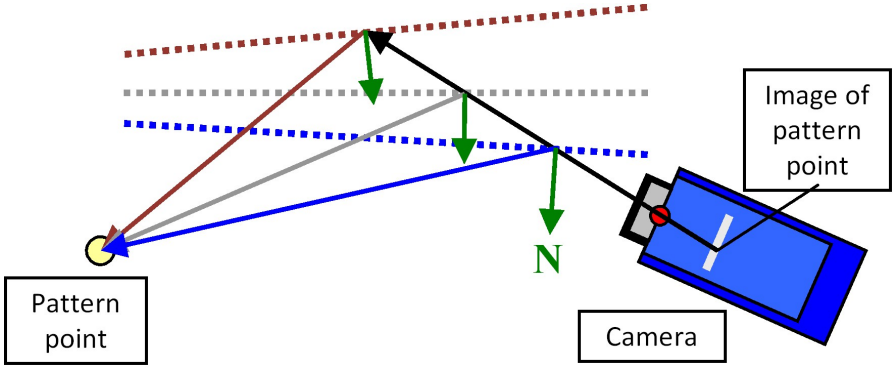

Figure 1.2.: Back-traced pattern point with three possible surfaces and their related normals

Existing approaches to resolve this ambiguity include the use of a stereoscopic setup with two cameras (Stereo Deflectometry [Knauer et al. 2004]) and the use of direct coding of the illumination direction together with a telecentric observation (Richtungscodierte Deflektometrie [Seßner et al. 2004]).

The approach which is presented here uses a priori information about the surface and an iterative algorithm to resolve the ambiguity.

1.4. Non-stereoscopic Surface Reconstruction

It is assumed that the surface has a smooth height distribution without discontinuities and that its borders lie on a holding frame (Figure 1.3).

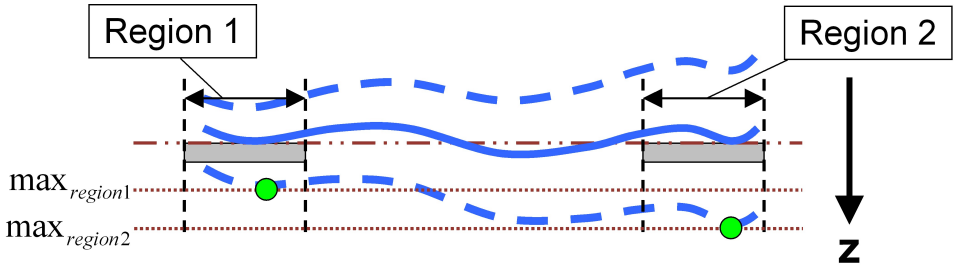

Figure 1.3.: Correct surface lying on a frame and two reconstructed surfaces with wrong start heights

All possible reconstructed surfaces show a slight deformation and - important here - a characteristic tilt, which is visible in the difference between the maxima at the regions of the surface above respectively below the holding frame:

$$\Delta h_{max} = max_{region1} - max_{region2} \tag{1.3}$$

Only the correct surface features no tilt, as the maxima have the same value that corresponds to the holding frame position (Figure 1.3). This criterion is used to determine if the correct surface was found.

This approach consists of two nested iterative algorithms (Figure 1.4). The inner iteration loop uses a self-consistent method to reconstruct a surface corresponding to a given start height H_{start}, which is defined as the arithmetic average of the reconstructed surface's heights. The outer iteration loop finds the best start height for the inner loop by evaluating the differences of the maxima at the holding frame regions Δh_{max}.

The first outer loop run is done with the holding frame's z-position as start height. The position of the holding frame is obtained by a calibration of the whole deflectometric setup (2.7). After a full run of the inner loop Δh_{max} is evaluated and the iteration continues until the absolute value of Δh_{max} is equal or below a given threshold. Then the height distribution of the measured surface is obtained with high accuracy. If the criterion is not fulfilled, the start height is modified in respect to the distances of the found maxima $max_{region1}$ and $max_{region2}$ towards the frame region's z-position. The shortest distance d_{min} gives the amount and through its sign the direction of the adjustment.

The new start height $H_{start,i+1}$ is calculated as follows:

$$H_{start,i+1} = H_{start,i} - d_{min} \tag{1.4}$$

The inner loop starts with a plane surface at the start height. The normals are then calculated by ray tracing the camera rays and the pattern rays assuming that they cross at the plane surface. The normals are then converted to gradients, which are used to approximate the height distribution of the surface with shifted base functions [Brenner 2008]. The bias B of the surface is unknown, because gradients were used to reconstruct it. Therefore the bias is set to the difference of the start height H_{start} and the arithmetic average of the surface's heights $S_{average}$. This fulfills the definition of the start height.

$$B = H_{start} - S_{average} \tag{1.5}$$

The following runs of the inner loop are using the reconstructed surface of the preceding run instead of the plane surface. The inner iteration loop stops when the root mean square of the difference of the heights of the current surface and the previous reconstructed surface is below a given threshold.

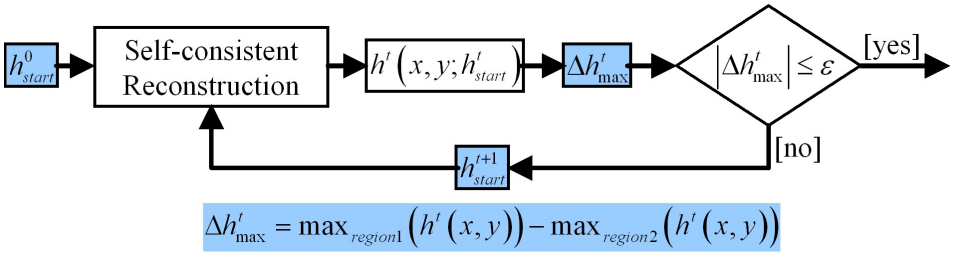

Figure 1.4.: Finding the best start height

1.5. Marker Identification

The surface reconstruction requires to find marker positions in the camera image and to match them to the observed markers. The markers are spots, whose intensity fades out towards the outer bound. The algorithm is divided into four steps. The first one provides the centroid coordinates of all markers. In the second step markers which are are too large or too small in size because of being not completely reflected are sorted out. The periods in both directions and the tilt angle of the pattern are found in the third step. In the last step the knowledge about the tilt angle and the periods is utilized to index the found centroids relative to the reference marker, which is identified in this step through its size. This results in a correlation between markers found in the camera image and markers on the observed pattern.

1.5.1. Centroid Search

Since a marker is a conglomerate of pixels with gray values above a threshold, all pixels relating to one marker can be found by scanning the image pixel-wise and by looking at the neighboring pixels. If a pixel has a gray value above the given threshold, its position and gray value is saved and the direct neighbors are checked for also having a gray value above the threshold. This is repeated until no more neighboring pixels with values above the threshold are found. Now the centroid $\mathbf{r}_s$ of the marker is calculated with the equation for the center of mass [Meschede 2006], substituting the masses with the gray values of the N found pixels:

$$\mathbf{r}_s = \frac{1}{G} \sum_{i}^{N} g_i \mathbf{r}_i$$

with

$$G = \sum_{i}^{N} g_i$$

with $\mathbf{r}_i$ being the coordinate and g_i the gray value of the i^{th} found pixel. This procedure is repeated until every pixel of the image was checked. Then a list of the centers of all found possible markers is obtained with $N_{candidates}$ entries.

1.5.2. Marker Filtering

After all possible markers have been found, it is necessary to filter them by size. On the one hand, there might be some clusters of pixels above the threshold, which result from noise or other structures in the image. On the other hand, the observed pattern is larger than the reflecting surface. The markers reflected at the edges of the substrate are only reflected partially. This leads to wrong centers of gravity and thereby inaccuracy in the determination of the gradients.

Therefore these markers must be filtered out. In order to accomplish this, the area of the $N_{candidates}$ markers is calculated and compared to the median area of all markers. Those not inside a given range around the median area are then sorted out. This leads to a number of markers $N_{markers} \leq N_{candidates}$.

1.5.3. Grid Identification

Periods

The periods p_x and p_y of the pattern in both directions and the tilt angle is obtained by analyzing the Fourier transformation of the image. Despite the geometric deformations caused by the reflection, the image of the pattern still has periodic features. For the

determination a coarse estimate of the x-axis and y-axis vectors of the pattern is needed. Since the x-axis is due to the experimental setup always almost $\begin{pmatrix}1\\0\\0\end{pmatrix}$ and the y-axis $\begin{pmatrix}0\\1\\0\end{pmatrix}$, these vectors are used. The lowest frequency components give a coarse evidence of the pattern's periods.

1.5.4. Marker Indexing

The marker indexing is done by looking at the proximity relationship of the markers. The direct neighbors are found by looking at the angle in respect to the axes and the distance (Figure 1.5(a)). Only those markers are taken into account which are within a given search radius r_s (red circle in Figure 1.5(a)). The search radius is calculated from the periods p_x and p_y:

$$r_s = \sqrt{(1.5p_x)^2 + (1.5p_y)^2}$$

These candidates are then classified into eight angle categories representing the eight possible neighbors. The angle categories take the tilt angle into account. If more than one candidate is in one angle category, only the closest marker is kept. After all neighbors of one marker are found, the algorithm continues with the markers found in the edges (Figure 1.5(b)). The algorithm stops, when no more neighbors are found. The indexing starts at the reference marker (identified by the largest area), which gets the index $[0, 0]$.

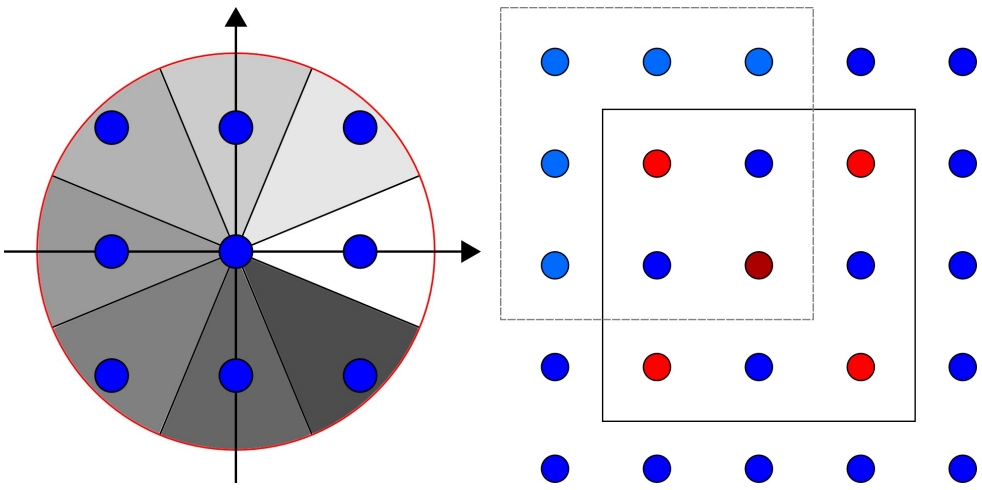

(a) Angle categories (b) Neighbors

Figure 1.5.: Marker indexing

1.6. Ray Tracing

Ray tracing is used to calculate the normals and the gradients of the measured surface respectively. It is also used to render images for simulating the deflectometric measurement.

1.6.1. Transformation of Coordinates

It is necessary to transform global coordinates to local coordinates and vice versa at planes, so that the local features like markers at the intersection point $\mathbf{r}_i$ can be taken into account. The parameters of the planes, which are needed for the transformation, are the position of the center $\mathbf{r}_c$, and the vectors of the local coordinate system's axes $\mathbf{T}_x$, $\mathbf{T}_y$ and $\mathbf{N}_z$.

Global to Local

To get the local coordinate $\mathbf{r}_i^{local} = \begin{pmatrix} x_i^{local} \\ y_i^{local} \\ z_i^{local} \end{pmatrix}$ of a point $\mathbf{r}_i$ in global coordinates, first the local vector $\mathbf{r}_p^{local}$ is calculated:

$$\mathbf{r}_p^{local} = \mathbf{r}_i - \mathbf{r}_c$$

Then $\mathbf{r}_p^{local}$ is projected onto the axes $\mathbf{T}_x$, $\mathbf{T}_y$ and $\mathbf{N}_z$:

$$\begin{aligned} x_i^{local} &= \mathbf{r}_p^{local} \cdot \mathbf{T}_x \\ y_i^{local} &= \mathbf{r}_p^{local} \cdot \mathbf{T}_y \\ z_i^{local} &= \mathbf{r}_p^{local} \cdot \mathbf{N}_z \end{aligned}$$

The z-component z_i^{local} of $\mathbf{r}_i^{local}$ is zero when the point lies in the plane, so this can be used as a check.

Local to Global

The transformation of a local coordinate $\mathbf{r}_i^{local} = \begin{pmatrix} x_i^{local} \\ y_i^{local} \\ z_i^{local} \end{pmatrix}$ to the global coordinate is $\mathbf{r}_i$:

$$\mathbf{r}_i = \mathbf{r}_c + \left(x_i^{local} \cdot \mathbf{T}_x\right) + \left(y_i^{local} \cdot \mathbf{T}_y\right) + \left(z_i^{local} \cdot \mathbf{N}_z\right)$$

1.6.2. Camera Model

Parameters

For the camera a pin-hole model is assumed (Figure 1.6). The parameters are the camera center position $\mathbf{r}_c$, the tangential vectors of the sensor $\mathbf{T}_x$ and $\mathbf{T}_y$, the normal vector of the sensor $\mathbf{N}_z$, the image distance b, the pixel count NP_x and NP_y and the pixel sizes Δpx and Δpy.

In contrast to a real camera the camera center is behind the sensor plane to get an upright image when rendering scenes.

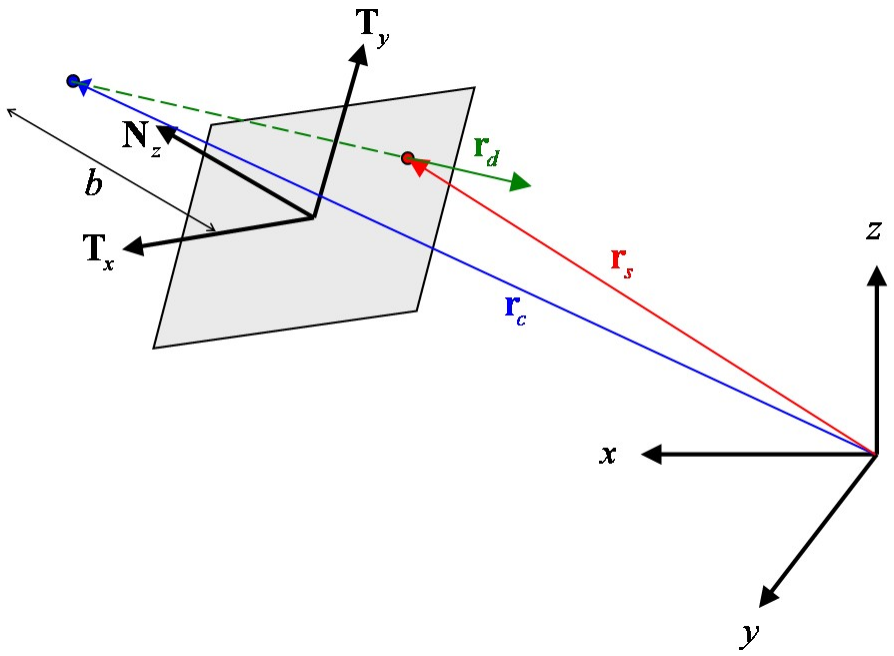

Figure 1.6.: Camera model

Calculating Camera Rays

Camera rays in the global coordinate system have to be calculated from local coordinates in the sensor plane for surface reconstruction and for simulations of a measurement. First the local coordinates x_s^{local} and y_s^{local} are transformed to global coordinates x_s^{global}, y_s^{global} and z_s^{global}. The starting point of the camera ray $\mathbf{r}_s$ is:

$$\mathbf{r}_s = \begin{pmatrix} x_s^{global} \\ y_s^{global} \\ z_s^{global} \end{pmatrix}$$

The direction of the camera ray is determined by $\mathbf{r}_s$ and the camera center $\mathbf{r}_c$:

$$\mathbf{r}_d = \frac{1}{|\mathbf{r}_s - \mathbf{r}_c|} (\mathbf{r}_s - \mathbf{r}_c)$$

1.6.3. Pattern Model

Parameters

The parameters of the pattern surface are the position of the center $\mathbf{r}_c$, the tangential vectors $\mathbf{T}_x$ and $\mathbf{T}_y$ to define the local coordinate system, the normal vector $\mathbf{N}_z$, the sizes ms_x and ms_y, the period of the marker pattern in both directions P_x and P_y and the number of markers in both directions NM_x and NM_y.

Calculating Intersection Points

The pattern is a plane surface. Therefore the intersection point is calculated by inserting the linear equation of the incoming ray $\mathbf{r} = \mathbf{r}_0 + \lambda \mathbf{r}_d$ into the Hesse normal form of the pattern plane:

$$\begin{aligned}
(\mathbf{r} - \mathbf{r}_c)\,\mathbf{N}_z &= 0 \\
[(\mathbf{r}_0 + \lambda \mathbf{r}_d) - \mathbf{r}_c]\,\mathbf{N}_z &= 0 \\
\mathbf{r}_0\mathbf{N}_z + \lambda \mathbf{r}_d\mathbf{N}_z - \mathbf{r}_c\mathbf{N}_z &= 0 \\
\lambda &= \frac{\mathbf{r}_c\mathbf{N}_z - \mathbf{r}_0\mathbf{N}_z}{\mathbf{r}_d\mathbf{N}_z}
\end{aligned}$$

The intersection point $\mathbf{r}_i$ then is:

$$\begin{aligned}
\mathbf{r}_i &= \mathbf{r}_0 + \lambda \mathbf{r}_d \\
&= \mathbf{r}_0 + \left(\frac{\mathbf{r}_c\mathbf{N}_z - \mathbf{r}_0\mathbf{N}_z}{\mathbf{r}_d\mathbf{N}_z} \right) \mathbf{r}_d
\end{aligned}$$

Rendering the Markers

The local coordinate of the intersection point $\mathbf{r}_i^{local}$ together with the knowledge about the marker periods P_x and P_y is used to determine at which marker (indexes IX and IY) and at which position inside the marker the ray hits the pattern.

Marker Index If NM_x is odd the marker with the index $IX = 0$ is in the center of the pattern. The index IX of the hit marker is:

$$IX = trunc \left(\frac{x_i^{local} + sign\left(x_i^{local}\right) \cdot \frac{ms_x}{2}}{ms_x} \right)$$

If NM_x is even the left edge of the marker with the index $IX = 0$ is at the center of the pattern and the index IX of the hit marker is:

$$IX = \left\lfloor \frac{x_i^{local}}{ms_x} \right\rfloor$$

The same applies to the index IY. If NM_y is odd:

$$IY = trunc\left(\frac{y_i^{local} + sign\left(y_i^{local}\right) \cdot \frac{ms_y}{2}}{ms_y} \right)$$

And for the case if NM_y is even:

$$IY = \left\lfloor \frac{y_i^{local}}{ms_y} \right\rfloor$$

Relative Position inside a Marker If NM_x is odd the relative x-position x_{rel} inside the marker with index IX is:

$$x_{rel} = x_i^{local} - (P_x \cdot ms_x)$$

If NM_x is even:

$$x_{rel} = x_i^{local} - [(P_x + 0.5) \cdot ms_x]$$

This applies analogously for the relative y-position x_{rel}. If NM_y is odd:

$$y_{rel} = y_i^{local} - (P_y \cdot ms_y)$$

If NM_y is even:

$$y_{rel} = y_i^{local} - [(P_y + 0.5) \cdot ms_y]$$

Marker Shape The markers are round shaped with radius r_m and feature a linear gradient of gray values from 1 to 0 towards the outer bound. The gray value g corresponding to a given relative position x_{rel}, y_{rel} inside a marker is:

$$g = 1 - \frac{\sqrt{x_{rel}^2 + y_{rel}^2}}{r_m}$$

1.6.4. Surface Model

Parameters

The parameters of the surface, which has to be measured, are the position of the center $\mathbf{r}_c$, the tangential vectors $\mathbf{T}_x$ and $\mathbf{T}_y$ and the normal vector $\mathbf{N}_z$ of the base plane. To

represent the height distribution $h(\mathbf{r}_\perp)$ either an array with cubic interpolation (for simulation) or Shifted Base Functions [Brenner 2008] (for reconstruction, see 1.8 for details) are mapped onto the base plane.

The real substrate is partly obscured by the holding frame on which it lies. Taking this into account the length of the surface is adapted to the size of the gap between both sides of the frame so that only the parts which are not lying on the frame are used for ray tracing. In the simulations the part of the surface in this gap is called the region of interest (ROI) and has a length of $48mm$.

Calculating Intersections Points

The determination of an intersection point is reached by an iterative method described in [Brenner 2012]. The incoming ray is described by:

$$\begin{aligned} \mathbf{r}_{in}(\lambda) &= \mathbf{r}_0 + \lambda \mathbf{r}_d \\ &= \begin{pmatrix} \mathbf{r}_\perp(\lambda) \\ z(\lambda) \end{pmatrix} \end{aligned}$$

Now a function is defined which gives the z-distance between ray and surface:

$$f(\lambda) = h(\mathbf{r}_\perp(\lambda)) - z(\lambda)$$

In order to find λ which gives the intersection point, the root of function $f(\lambda)$ must be determined.

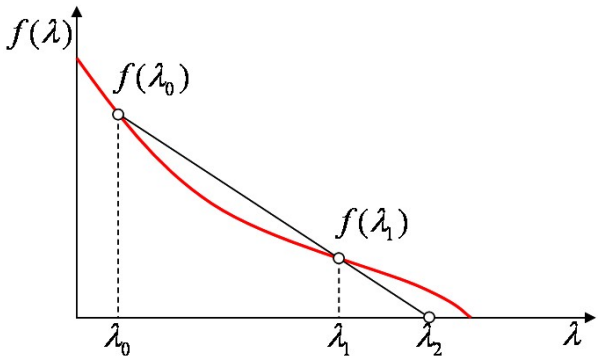

Figure 1.7.: Approximating the root of $f(\lambda)$

As it can be seen in Figure 1.7 it applies:

$$\frac{f(\lambda_0)}{\lambda_2 - \lambda_0} = \frac{f(\lambda_1)}{\lambda_2 - \lambda_1} \tag{1.6}$$

Solving Equation 1.6 for λ_2 produces:

$$\lambda_2 = \frac{\lambda_0 f(\lambda_1) - \lambda_1 f(\lambda_0)}{f(\lambda_1) - f(\lambda_0)}$$

In a general manner the next λ is calculated by:

$$\lambda_{n+1} = \frac{\lambda_{n-1} f(\lambda_n) - \lambda_n f(\lambda_{n-1})}{f(\lambda_n) - f(\lambda_{n-1})}$$

The starting points for the iteration are the origin of the ray and the intersection point of the ray with the base plane:

$$\begin{aligned} \lambda_0 &= 0 \\ \lambda_1 &= \frac{\mathbf{r}_c \mathbf{N}_z - \mathbf{r}_0 \mathbf{N}_z}{\mathbf{r}_d \mathbf{N}_z} \end{aligned}$$

The iteration stops if $f(\lambda)$ is smaller than a given threshold. After N iterations the intersection point is:

$$\mathbf{r}_{i,N} = \mathbf{r}_0 + \lambda_N \mathbf{r}_d$$

1.6.5. Reflection

Once the intersection point is found, the reflection at this position has to be calculated. With the incoming ray $\mathbf{r}_{in}$, the normal $\mathbf{N}$ at the intersection point and according to

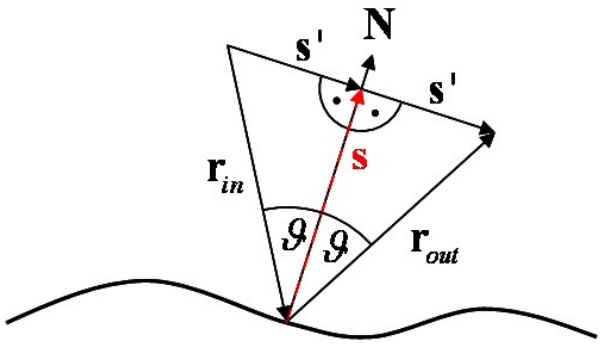

Figure 1.8.: Calculation of the reflection

Figure 1.8 it follows for the reflected ray $\mathbf{r}_{out}$:

$$\mathbf{r}_{out} = \mathbf{s} + \mathbf{s}' \tag{1.7}$$

with

$$\begin{aligned} \mathbf{s} &= \cos(\theta)\,\mathbf{N} \\ &= -(\mathbf{r}_{in}\mathbf{N})\,\mathbf{N} \\ \mathbf{s}' &= \mathbf{r}_{in} + \mathbf{s} \end{aligned}$$

Inserting this in Equation 1.7 gives:

$$\begin{aligned} \mathbf{r}_{out} &= \mathbf{s} + \mathbf{r}_{in} + \mathbf{s} \\ \mathbf{r}_{out} &= 2\mathbf{s} + \mathbf{r}_{in} \\ \mathbf{r}_{out} &= 2\left(-(\mathbf{r}_{in}\mathbf{N})\,\mathbf{N}\right) + \mathbf{r}_{in} \\ \mathbf{r}_{out} &= \mathbf{r}_{in} - 2(\mathbf{r}_{in}\mathbf{N})\,\mathbf{N} \end{aligned}$$

1.7. Determination of the Gradients

The found and indexed markers together with the knowledge about the geometry of the whole setup, which is obtained through calibration, are used to calculate the gradients necessary to reconstruct the heights of the measured surface. This is done by using ray tracing in the iterative algorithm described in 1.4.

1.7.1. Calculating the Normals

In the inner loop of the reconstruction algorithm one surface normal is obtained as follows: First the intersection point $\mathbf{r}_i$ of one marker's camera ray, which has the direction vector $\mathbf{s}_c$, with the surface is determined by ray tracing. Then the global coordinate $\mathbf{r}_p$ of the corresponding marker at the pattern is used to calculate the direction vector $\mathbf{s}_p$ of the ray from $\mathbf{r}_i$ towards the marker at the pattern:

$$\mathbf{s}_p = \frac{1}{|\mathbf{r}_p - \mathbf{r}_i|} (\mathbf{r}_p - \mathbf{r}_i)$$

The surface normal at the intersection point is calculated from $\mathbf{s}_c$ and $\mathbf{s}_p$:

$$N = \frac{1}{|\mathbf{s}_p - \mathbf{s}_c|} (\mathbf{s}_p - \mathbf{s}_c)$$

1.7.2. Transformation of Gradients to Normals

The tangential vector $\mathbf{T}_x$ at a point of a surface is:

$$\begin{aligned} \mathbf{T}_x &= \frac{1}{\sqrt{dx^2 + dh^2}} \begin{pmatrix} dx \\ 0 \\ dh \end{pmatrix} \\ &= \frac{1}{dx\sqrt{dx^2 + dh^2}} \begin{pmatrix} 1 \\ 0 \\ \frac{dh}{dx} \end{pmatrix} \\ &= \frac{1}{\sqrt{1 + hx^2}} \begin{pmatrix} 1 \\ 0 \\ hx \end{pmatrix} \end{aligned}$$

with the gradient in x-direction $hx = \frac{dh}{dx}$. Analogously for T_y:

$$\begin{aligned}
\mathbf{T}_y &= \frac{1}{\sqrt{dy^2 + dh^2}} \begin{pmatrix} 0 \\ dy \\ dh \end{pmatrix} \\
&= \frac{1}{dy\sqrt{dy^2 + dh^2}} \begin{pmatrix} 0 \\ 1 \\ \frac{dh}{dy} \end{pmatrix} \\
&= \frac{1}{\sqrt{1 + hy^2}} \begin{pmatrix} 0 \\ 1 \\ hy \end{pmatrix}
\end{aligned}$$

with the gradient in y-direction $hy = \frac{dh}{dy}$. The normal $\mathbf{N}$ at this surface point is the vector product of the tangential vectors. The normalization of the tangential vectors has no influence on the vector product, therefore the normalization is omitted and the resulting vector is normalized:

$$\begin{aligned}
\mathbf{N} &= \mathbf{T}_x \times \mathbf{T}_y \\
&= \frac{1}{\sqrt{1 + hx^2}} \begin{pmatrix} 1 \\ 0 \\ hx \end{pmatrix} \times \frac{1}{\sqrt{1 + hy^2}} \begin{pmatrix} 0 \\ 1 \\ hy \end{pmatrix} \\
&= \frac{1}{\sqrt{1 + hx^2}} \frac{1}{\sqrt{1 + hy^2}} \begin{pmatrix} -hx \\ -hy \\ 1 \end{pmatrix} \\
&= \frac{1}{\sqrt{hx^2 + hy^2 + 1}} \begin{pmatrix} -hx \\ -hy \\ 1 \end{pmatrix}
\end{aligned}$$

1.7.3. Transformation of Normals to Gradients

The transformation from normals to gradients can be derived from the transformation from gradients to normals.

$$\begin{aligned}
\mathbf{N} &= \frac{1}{\sqrt{hx^2 + hx^2 + 1}} \begin{pmatrix} -hx \\ -hy \\ 1 \end{pmatrix} \\
&= \begin{pmatrix} N_x \\ N_y \\ N_z \end{pmatrix} \\
&= -N_z \begin{pmatrix} hx \\ hy \\ 1 \end{pmatrix}
\end{aligned} \tag{1.8}$$

From Equation 1.8 follows for the gradients:

$$\begin{aligned} hx &= -\frac{N_x}{N_z} \\ hy &= -\frac{N_y}{N_z} \end{aligned}$$

1.8. Height Reconstruction with Shifted Base Functions

To reconstruct a smooth surface from gradient data, shifted base functions, which are settled on a Cartesian grid, are used [Brenner 2008]. As this approach is a least-square approximation, measurement errors are reduced in contrast to interpolation schemes.

Configuration parameters are the base function Ψ itself, scaling factors σ in all dimensions (the base function may not be rotationally symmetric) and the number of grid points B.

The gradient data is represented as a list:

$$\left(\mathbf{r}_i, \mathbf{y}_i\right), i = 0..M-1$$

$\mathbf{r}_i$ is the position vector in a D-dimensional space and $\mathbf{y}_i$ the vector with the corresponding measured gradients. With $f_j = \frac{\partial f}{\partial x_j}$, where f is the height function, and $\Psi_j = \frac{\partial \Psi}{\partial x_j}$, where Ψ is the base function, the model for the gradient approximation is:

$$f_j\left(\mathbf{r}\right) = \sum_{k=0}^{B-1} c_k \Psi_j\left(\mathbf{r} - \mathbf{r}_k, \sigma\right)$$

Once the optimal coefficients c_k are obtained, the height function $f\left(\mathbf{r}\right)$ can be determined without explicit integration:

$$f\left(\mathbf{r}\right) = \sum_{k=0}^{B-1} c_k \Psi\left(\mathbf{r} - \mathbf{r}_k, \sigma\right)$$

To obtain the optimal coefficient c_k the error function

$$\Phi\left(c_k\right) = \sum_i \left(\mathbf{f}\left(\mathbf{r}_i\right) - \mathbf{y}_i\right)^T \left(\mathbf{f}\left(\mathbf{r}_i\right) - \mathbf{y}_i\right)$$

is minimized by solving the set of equations

$$\frac{1}{2}\frac{\partial \Phi}{\partial c_k} = 0$$

Inserting the definition of the model function and taking the partial derivative a linear set of equations is obtained:

$$\sum_{k'=0}^{B-1} c_{k'} M_{k,k'} = V_k$$

with

$$M_{k,k'} = \sum_{j=0}^{D-1} \sum_{i=0}^{M-1} \left(\Psi_j \left(\mathbf{r}_i - \mathbf{r}_{k'} \right) \Psi_j \left(\mathbf{r}_i - \mathbf{r}_k \right) \right)$$

$$V_k = \sum_{j=0}^{D-1} \left(\sum_{i=0}^{M-1} y_{j,i} \Psi_j \left(\mathbf{r}_i - \mathbf{r}_k \right) \right)$$

Matrix $\mathbf{M}$ is real and symmetric and thus the coefficients c_k can be solved with standard algebraic techniques.

Here an inverse multiquadric base function is used:

$$\Psi \left(x, y, \sigma_x, \sigma_y \right) = \frac{1}{\sqrt{1 + \left(\frac{x}{\sigma_x} \right)^2 + \left(\frac{y}{\sigma_y} \right)^2}}$$

1.9. Generation of the Simulated Surfaces

The simulated surfaces have to feature a smooth, continuous height distribution to appropriately model the deformed glass substrates. Another requirement is, that the two areas of the surface above the holding frame regions feature at least one maximum each with the value 0. These maxima represent the contact area of the substrate with the holding frame.

First a 2-dimensional array is filled with random numbers in the range $[0, 1]$. This is far away from a smooth distribution as this represents white noise (Figure 1.9(a)). Thus the array is Fourier transformed and the values are low-pass filtered (Figure 1.9(b)). To satisfy the requirement concerning the maxima at the frame regions the surface is tilted until the maximum values in both frame regions are both 0 (Figure 1.9(c)). In the last step the height distribution is scaled to the desired range (Figure 1.9(d)).

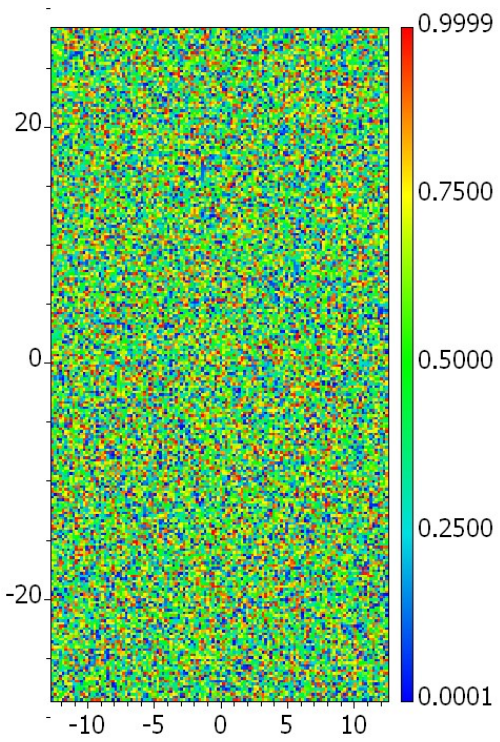

(a) Step 1: Random height distribution with values in the range $[0, 1]$

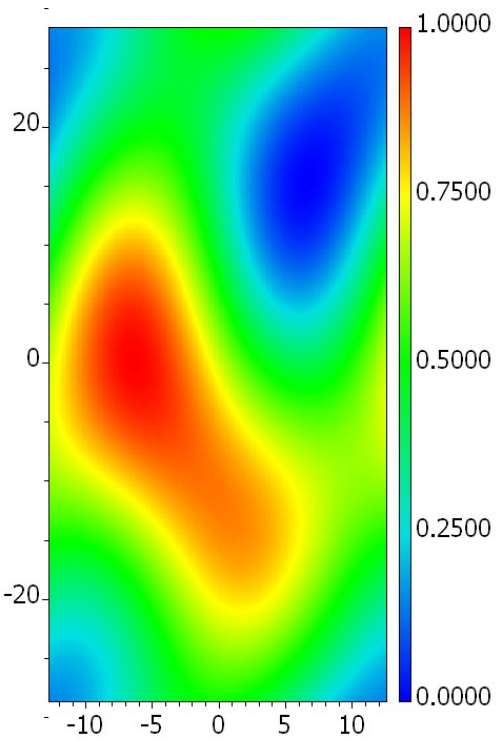

(b) Step 2: Height distribution after low-pass filtering

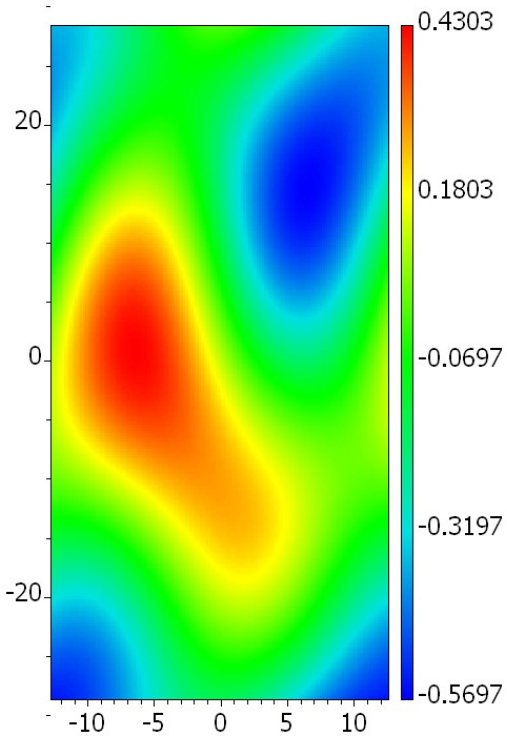

(c) Step 3: Tilted height distribution

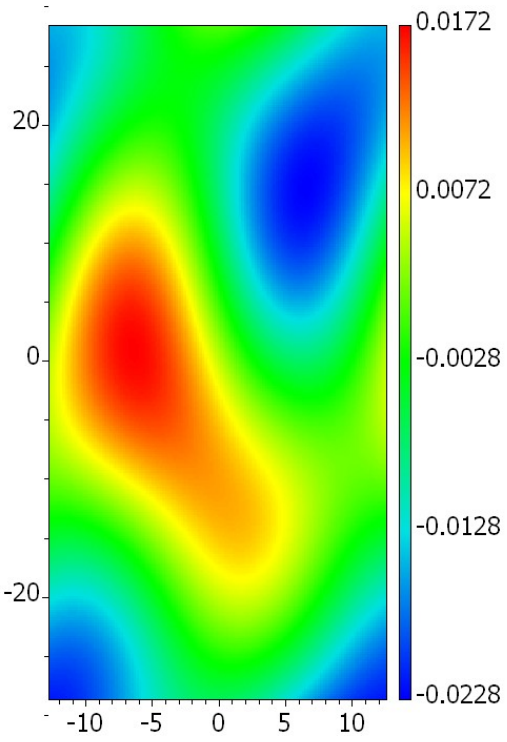

(d) Step 4: Height distribution after scaling it to the desired range

Figure 1.9.: Generating the simulated surface (units are *mm*)

1.10. Simulations

The positions and orientations of the camera and the pattern are chosen to fulfill the Scheimpflug principle. That means that the pattern is seen from the camera without perspective distortions and the pattern is imaged with the maximum possible sharpness.

Surface Parameters

The surface plane is by definition the global coordinate system. Thus the center is at $\mathbf{r}_c = \begin{pmatrix} 0 \\ 0 \\ 0 \end{pmatrix} mm$ and the vectors of the coordinate system are $\mathbf{T}_x = \begin{pmatrix} 1 \\ 0 \\ 0 \end{pmatrix}$, $\mathbf{T}_y = \begin{pmatrix} 0 \\ 1 \\ 0 \end{pmatrix}$ and $\mathbf{N}_z = \begin{pmatrix} 0 \\ 0 \\ 1 \end{pmatrix}$.

The dimensions of the surface are $25.2mm$ in x-direction and $57mm$ in y-direction. Two different height distributions are simulated, which both feature a range of $40\mu m$. They are depicted in Figure 1.10.

Camera Parameters

The center of the camera is $\mathbf{r}_c = \begin{pmatrix} 0 \\ -200 \\ 120 \end{pmatrix} mm$, the vectors describing the local coordinate system of the sensor are $\mathbf{T}_x = \begin{pmatrix} 1 \\ 0 \\ 0 \end{pmatrix}$, $\mathbf{T}_y = \begin{pmatrix} 0 \\ 0.5145 \\ 0.8575 \end{pmatrix}$ and $\mathbf{N}_z = \begin{pmatrix} 0 \\ -0.8575 \\ 0.5145 \end{pmatrix}$. The image distance is $b = 28mm$ and the focal length $f = 25mm$. The number of pixels in the x-direction is 1360, in the y-direction 1024. The pixels are square shaped with a size of $4.65\mu m$.

The rendered camera images for both height distributions are shown in Figure 1.11.

Pattern Parameters

The center of the pattern lies at $\mathbf{r}_c = \begin{pmatrix} 0 \\ 80 \\ 48 \end{pmatrix} mm$. The vectors defining the local coordinate system are $\mathbf{T}_x = \begin{pmatrix} 1 \\ 0 \\ 0 \end{pmatrix}$, $\mathbf{T}_y = \begin{pmatrix} 0 \\ -0.5145 \\ 0.8575 \end{pmatrix}$ and $\mathbf{N}_z = \begin{pmatrix} 0 \\ -0.8575 \\ -0.5145 \end{pmatrix}$.

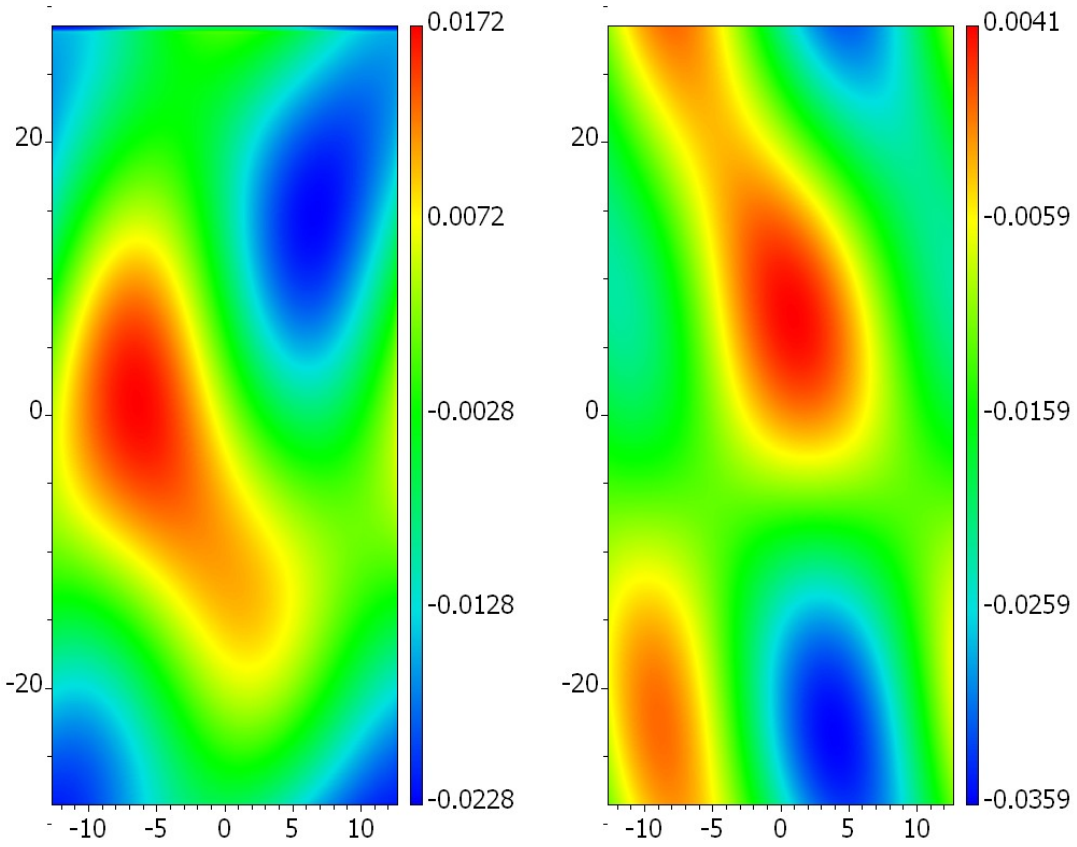

(a) Height distribution 1 (b) Height distribution 2

Figure 1.10.: Simulated surfaces (units are mm)

There are 33 markers in both directions with a spacing of $1.5mm$ and a radius of $0.5mm$. The reference marker is positioned at the center and its radius is $0.7mm$. The pattern features a square shape with an edge length of $50mm$.

Reconstruction

The count of shifted base functions in x-direction is 9, in y-direction 5. The scaling factors are $\sigma_x = 4$ and $\sigma_y = 3$.

Height Distribution 1 After 14 iterations of the start height, each with 3 iterations of the inner surface reconstruction loop, the height difference of the maxima is $-0.15\mu m$. Figure 1.12 shows the reconstructed surface and the absolute value of the difference between reconstructed and original surface. The maximum deviation from the original surface is $7.577\mu m$, the root-mean-square value of the difference is $4.578\mu m$. In the region of interest, which is the space between the frame regions, the maximum deviation is $0.697\mu m$ and the root-mean-square value of the difference is $0.097\mu m$. The values for the region of interest are much smaller, because no gradients in the frame regions are

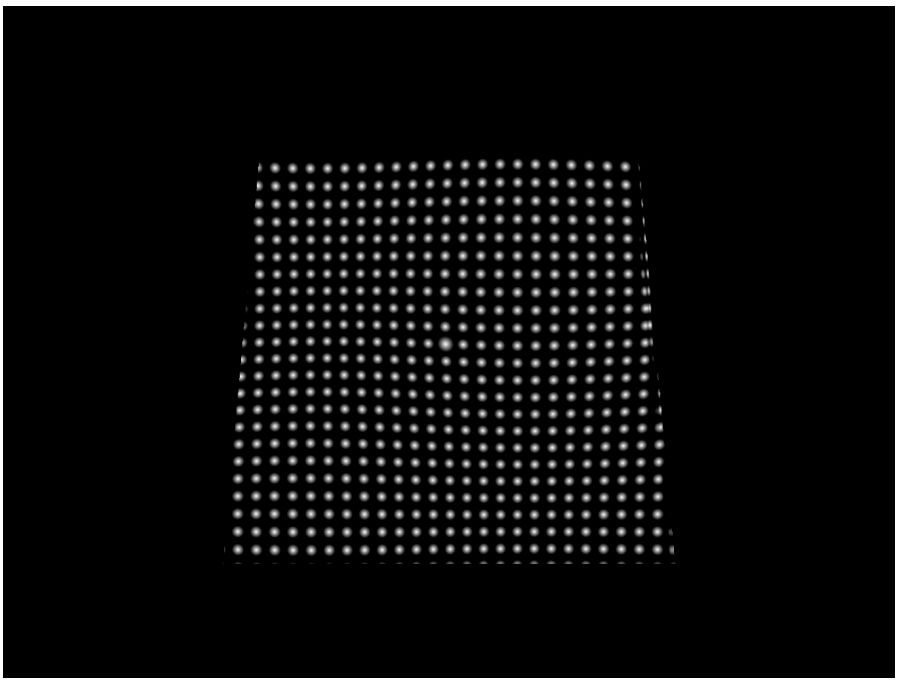

(a) Height distribution 1

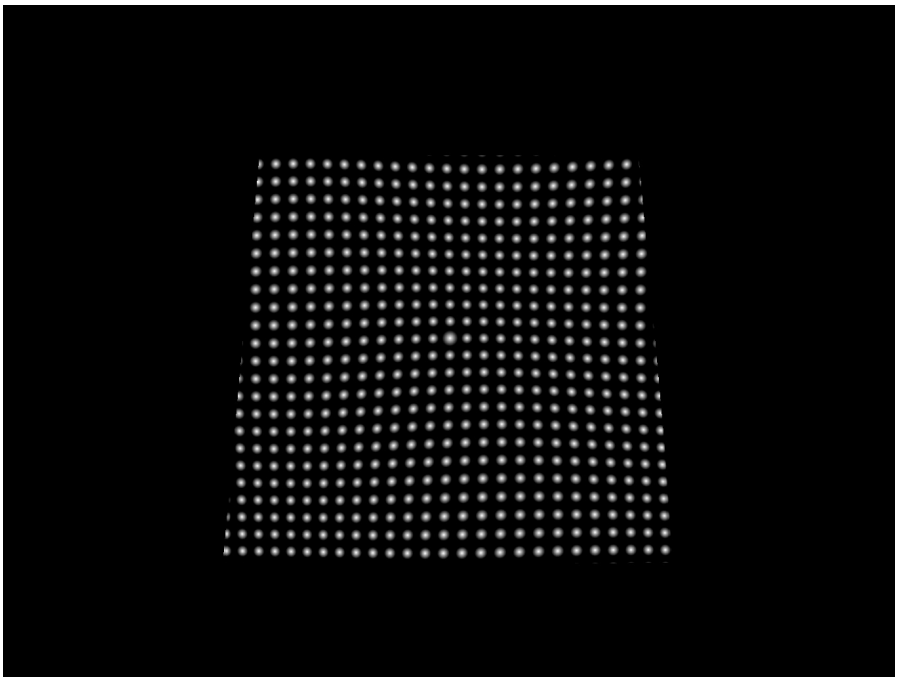

(b) Height distribution 2

Figure 1.11.: Rendered camera images

available as the frame covers the substrate.

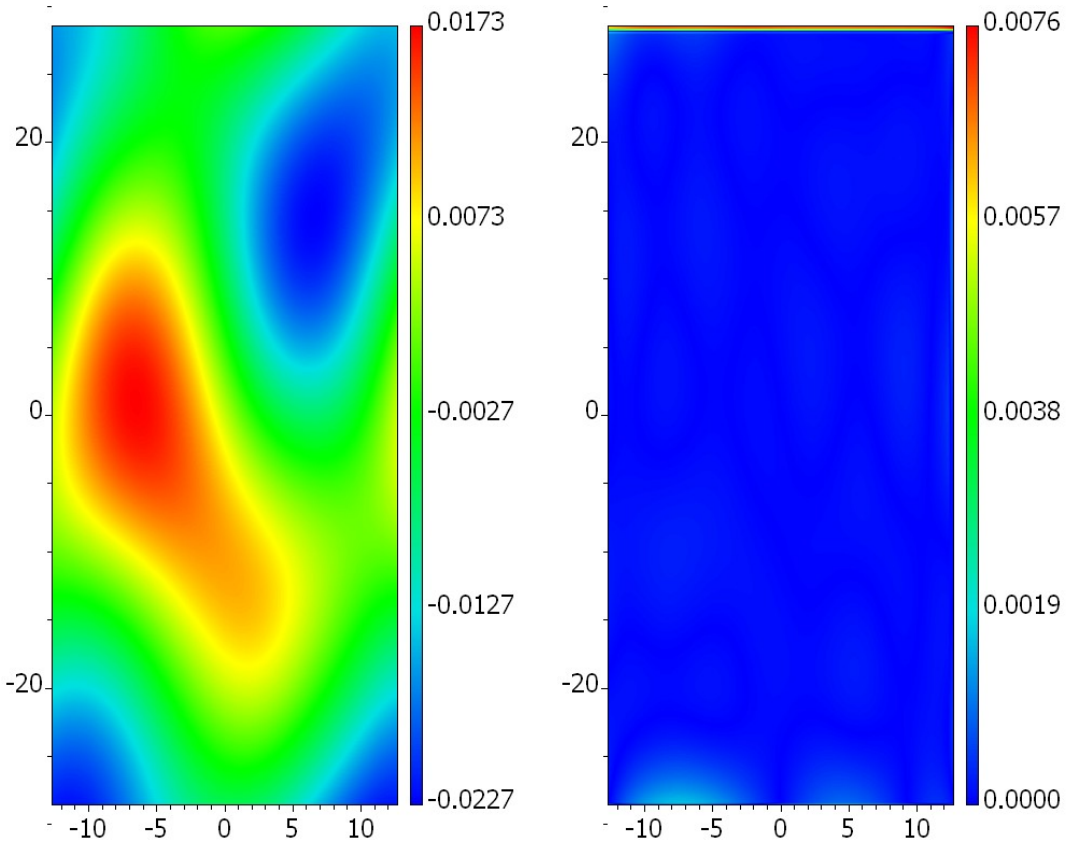

(a) Reconstructed surface

(b) Absolute value of the difference between reconstructed and simulated surface

Figure 1.12.: Reconstruction of height distribution 1 (units are mm)

Height Distribution 2 The start height iteration loop takes 9 runs, each with 3 iterations of the inner surface reconstruction loop. After the iterations the height difference of the maxima is $-0.009\mu m$. Figure 1.13 shows the reconstructed surface and the absolute value of the difference between reconstructed and simulated surface. The maximum deviation to the original surface is $1.943\mu m$, the root-mean-square value of the difference is $0.213\mu m$. In the region of interest the maximum deviation is $0.359\mu m$ and the root-mean-square value of the difference is $0.092\mu m$.

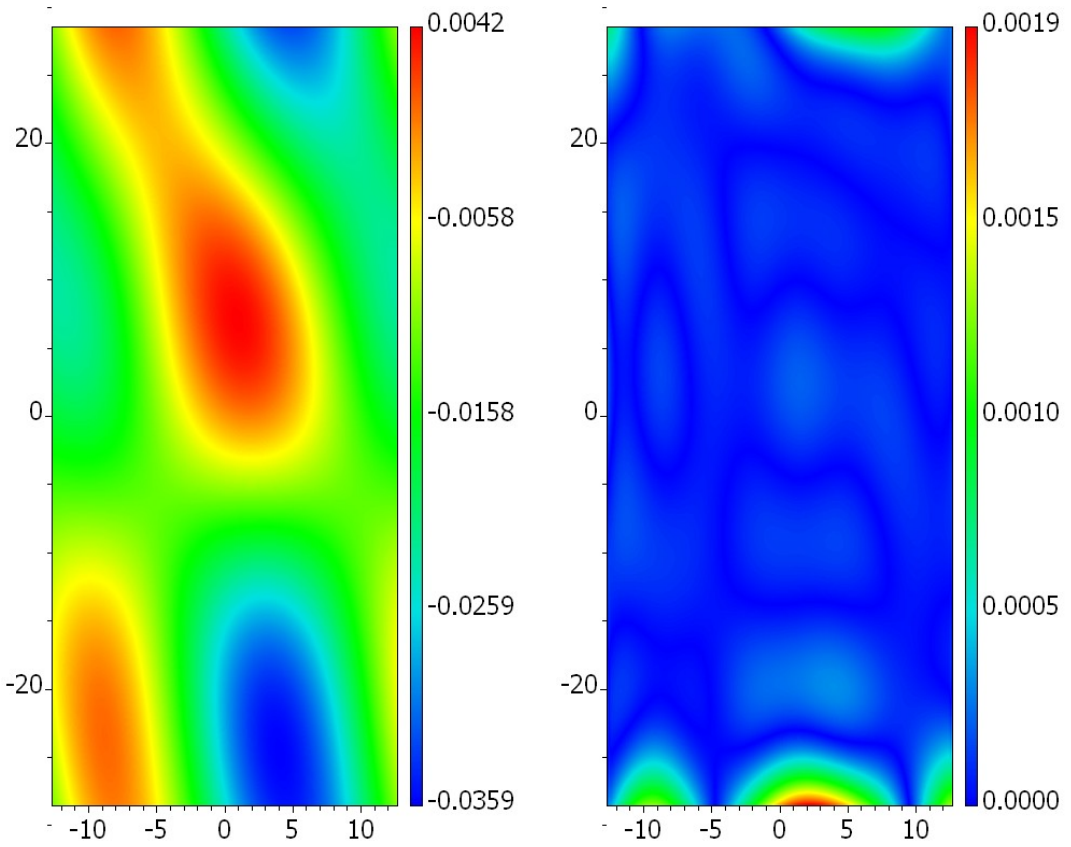

(a) Reconstructed surface

(b) Absolute value of the difference between reconstructed and simulated surface

Figure 1.13.: Reconstruction of height distribution 2 (units are mm)

1.11. Experimental Setup

The experimental setup, which is shown in Figure 1.14, uses the monochrome camera CFW-1312M from the company Scion. The image resolution is 1340 pixels in horizontal direction and 1024 pixels in vertical direction. The pixel size in the x-direction and the y-direction is $4.65\mu m$ and the bit-depth of the images is 12 bit. The objective lens is a MeVis-C from the company Linos with a focal length of $25mm$. The highest f-number of 16 is used in this setup to achieve a large depth of focus. As the illumination source for the pattern should fulfill Lambert's cosine law to illuminate the pattern homogeneously, an electroluminescence foil is used. This also applies for the illumination of the calibration pattern in the substrate plane.

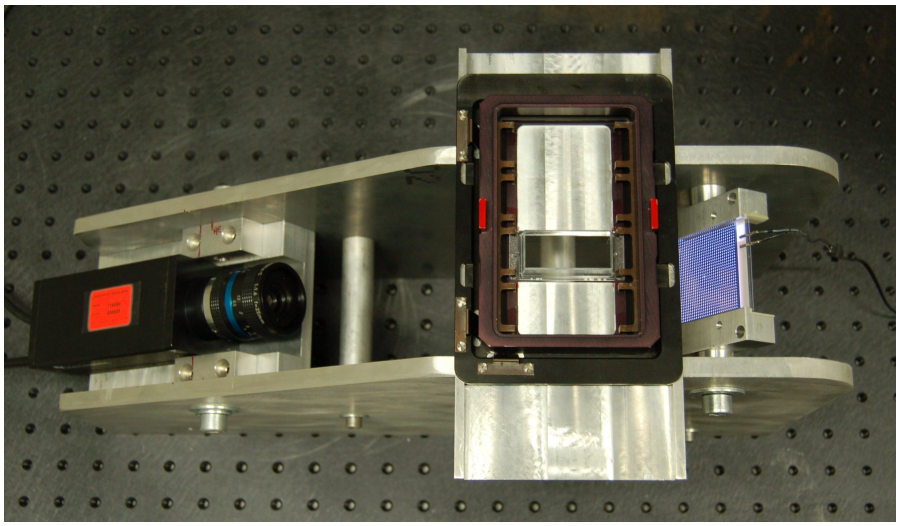

Figure 1.14.: Experimental defelctometry setup

1.12. Experimental Results

First the calibration of the setup, which is described in 2.9.2, was performed. Then the iterative reconstruction with the camera image of the pattern reflected by a substrate was started. The camera image is shown in Figure 1.15. The substrate is pushed against the holder by clamps, therefore it is ensured that the substrate lies on the frame.

The number of shifted base functions in the x-direction is 9, in the y-direction is 5. The scaling factors are $\sigma_x = 4$ and $\sigma_y = 3$. After 11 iterations of the start height, each with 3 iterations of the inner surface reconstruction loop, the height difference of the maxima was $-2.083\mu m$. The resulting surface is depicted in Figure 1.17(a). The height distribution shows a characteristic deformation of the measured substrate with a range of $65.9\mu m$, which fits to the refocusing range observed in the microscopes.

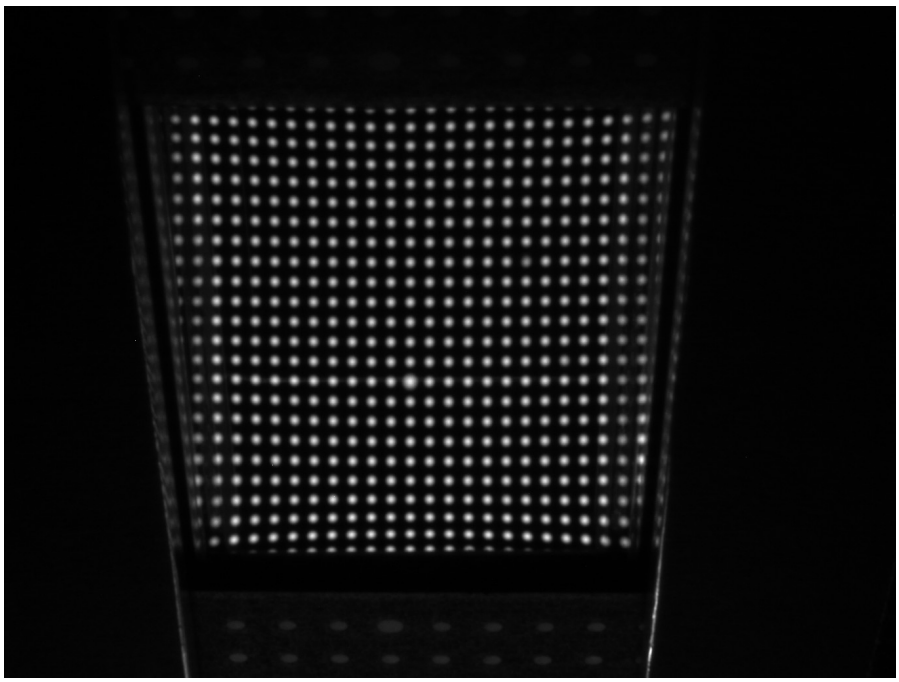

Figure 1.15.: Camera image (experiment)

The substrate was then rotated by an angle of 180° to compare the reconstructed surfaces. The captured camera image is shown in Figure 1.15.

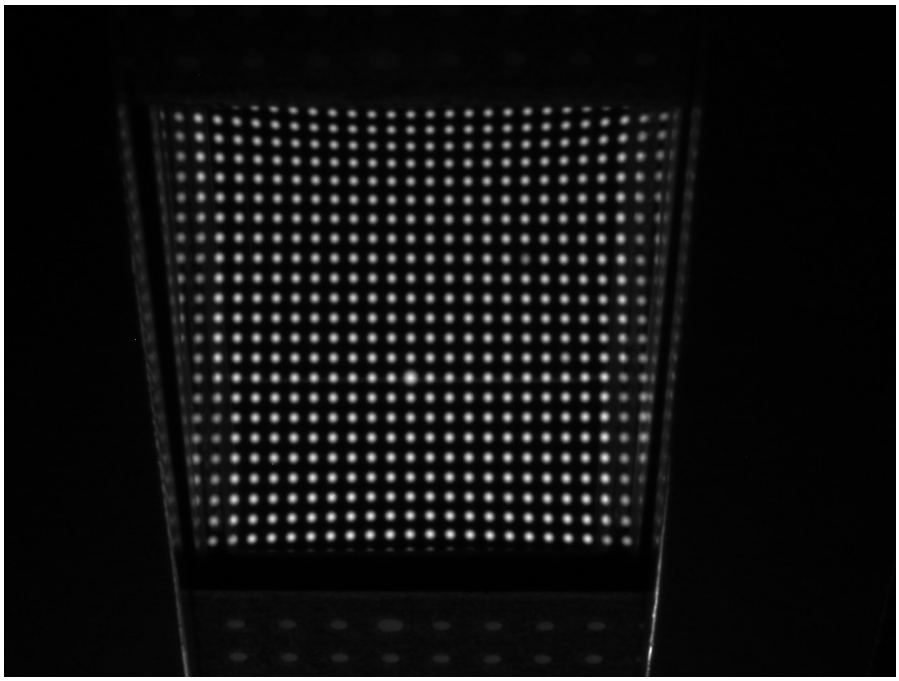

Figure 1.16.: Camera image after rotation (experiment)

It was not expected that the height distributions match completely, as the substrate was

turned around and fixed with the help of the clamps of the holder again, thus deforming the substrate in a slight different way. But it can be seen, that the main characteristics are found again and the same height range of $65.9\mu m$ is obtained (Figure 1.17(b)).

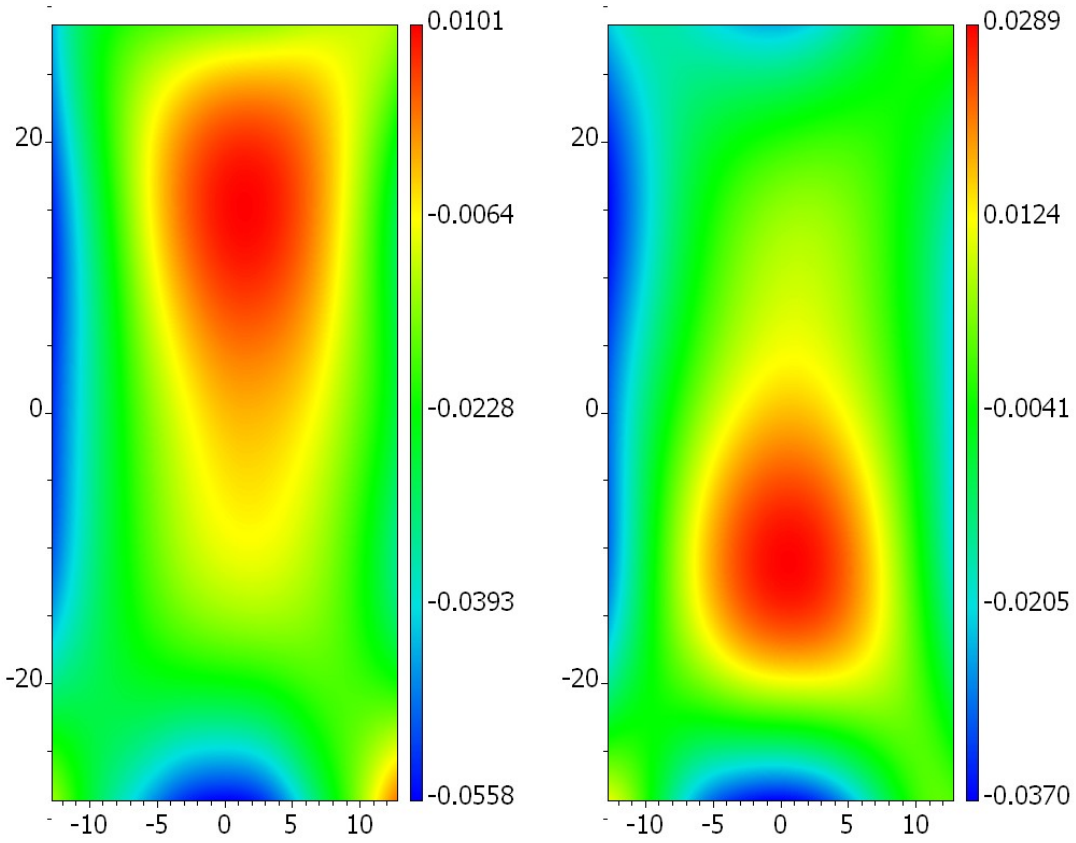

(a) Reconstructed surface

(b) Reconstructed surface after rotation

Figure 1.17.: Reconstructed surfaces (experiment) (units are mm)

1.13. Summary

The presented deflectometric method for measuring the height distribution of glass substrates needs only one camera image to obtain the gradients of the measured surface. This is accomplished by a priori information about the position of the surface, which lies on a holding frame. The position of the holding frame is obtained through a calibration. With this method it is possible to directly take a sharp image of the observed object located on the substrate without searching the correct focus plane.

The simulations show that the height distributions are reconstructed with an accuracy below $1\mu m$ in the region of interest. The self-consistent algorithm to reconstruct a surface corresponding to a given start height converges on an average of $3-4$ iterations, while the iteration count of the outer loop typically is around 10.

In the experiment the features of the reconstructed surface fit to the refocusing range found when this kind of substrates are used in a microscope. The comparison of one measurement with a second measurement with the same substrate rotated by an angle of 180° shows that the main characteristics and the same height range is obtained again. The differences result from the fixation with clamps which are used to fix the substrate to the frame.

2. One-Shot Camera Calibration

2.1. Introduction

For the deflectometric measurement of the deformed glass substrate it is necessary to know the positions and orientations of the camera, the pattern and the holding frame in the setup. To obtain these values, a camera calibration was developed, which needs just one captured camera image of an observed known pattern to get the relative position and tilt of the camera. The only a-priori parameters are the pixel size to get dimensioned coordinates in the sensor plane, the focal length f and a coarse estimate of the sensor's normal vector $\mathbf{N}_z$.

In contrast to the standard approach of Zhang [Zhang 2000], here the camera geometry is the basis for the derivation of the calibration and only one camera image is needed for the determination of the camera parameters, whereas Zhang's approach needs at least two images of the observed pattern from different viewing points.

2.2. Coordinate System

The coordinate system is defined by the calibration pattern, formed by a Cartesian grid of markers (Figure 2.1). The point of origin is located at the center of the pattern. To define the axes, a reference marker is used. It is the last spot in negative x- and negative y-direction. As this is a right-handed coordinate system the z-axis is pointing upwards.

2.3. Camera Parameters

The camera is described as a pinhole type camera. The parameters used for the derivation of the camera calibration are described in Table 2.1.

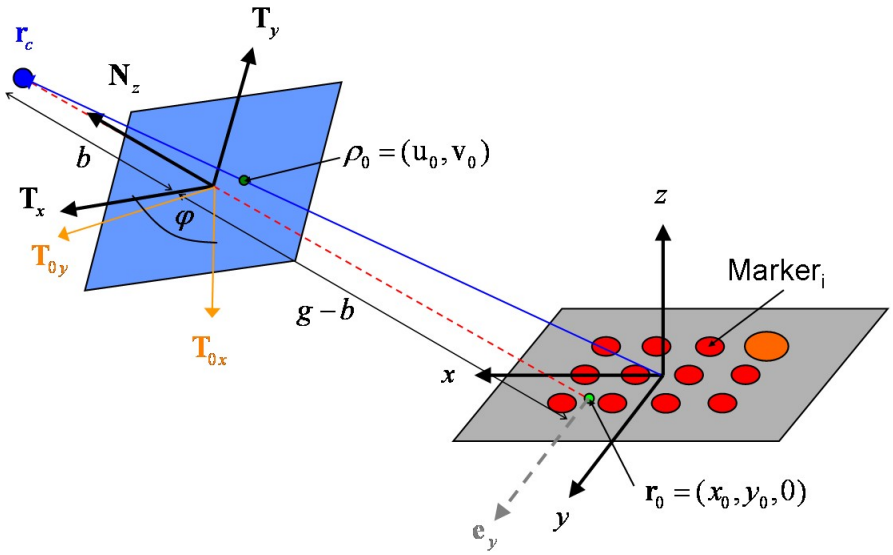

Figure 2.1.: Coordinate system

Parameter	Description
$\mathbf{r}_c = \begin{pmatrix} x_c \\ y_c \\ z_c \end{pmatrix}$	camera center (pinhole position)
$\mathbf{r}_0 = \begin{pmatrix} x_0 \\ y_0 \\ 0 \end{pmatrix}$	point where the optical axis cuts the pattern
$\mathbf{T}_x$	tangential vector of the camera sensor in x-direction
$\mathbf{T}_y$	tangential vector of the camera sensor in y-direction
$\mathbf{N}_z$	normal vector of the camera sensor
b	image distance
g	object distance

Table 2.1.: Camera parameters

2.4. Linear Approximation

2.4.1. Derivation

The camera center is described as:

$$\mathbf{r}_c = \mathbf{r}_0 + g\mathbf{N}_z \tag{2.1}$$

The image of the j^{th} marker in the sensor plane represented by coordinates in the sensor plane (u_j, v_j):

$$\rho_j = \mathbf{r}_0 + (g - b)\mathbf{N}_z + u_j\mathbf{T}_x + v_j\mathbf{T}_y \tag{2.2}$$

The image can also be represented by the coordinates of the marker in the global coordinate system $\mathbf{r}_j$:

$$\rho_j = \mathbf{r}_j + \lambda\left(\mathbf{r}_c - \mathbf{r}_j\right) \tag{2.3}$$

Now the right sides of Equation 2.2 and Equation 2.3 are equalized and $\mathbf{r}_c$ is substituted by Equation 2.1:

$$\begin{aligned} \mathbf{r}_0 + (g-b)\mathbf{N}_z + u_j\mathbf{T}_x + v_j\mathbf{T}_y &= \mathbf{r}_j + \lambda\left(\mathbf{r}_c - \mathbf{r}_j\right) \\ \mathbf{r}_0 + (g-b)\mathbf{N}_z + u_j\mathbf{T}_x + v_j\mathbf{T}_y &= \mathbf{r}_j + \lambda\left(\mathbf{r}_0 + g\mathbf{N}_z - \mathbf{r}_j\right) \end{aligned} \tag{2.4}$$

Rewriting Equation 2.4 and reintroducing $\mathbf{r}_c$ produces:

$$\begin{aligned} u_j\mathbf{T}_x + v_j\mathbf{T}_y &= (1-\lambda)\left(\mathbf{r}_j - \mathbf{r}_0 - g\mathbf{N}_z\right) + b\mathbf{N}_z \\ u_j\mathbf{T}_x + v_j\mathbf{T}_y &= (1-\lambda)\left(\mathbf{r}_j - \mathbf{r}_c\right) + b\mathbf{N}_z \end{aligned} \tag{2.5}$$

To obtain an expression for u_j Equation 2.5 is multiplied with $\mathbf{T}_x$:

$$u_j = (1-\lambda)\left(\mathbf{r}_j - \mathbf{r}_c\right)\mathbf{T}_x \tag{2.6}$$

To obtain an expression for v_j Equation 2.5 is multiplied with $\mathbf{T}_y$:

$$v_j = (1-\lambda)\left(\mathbf{r}_j - \mathbf{r}_c\right)\mathbf{T}_y \tag{2.7}$$

Multiplying Equation 2.5 with $\mathbf{N}_z$ and rewriting the equation gives an expression for λ:

$$\begin{aligned} 0 &= (1-\lambda)\left(\mathbf{r}_j - \mathbf{r}_c\right)\mathbf{N}_z + b \\ (1-\lambda) &= -\frac{b}{\left(\mathbf{r}_j - \mathbf{r}_c\right)\mathbf{N}_z} \end{aligned} \tag{2.8}$$

Substituting $(1-\lambda)$ from Equation 2.8 in Equation 2.6 and Equation 2.7 produces:

$$\begin{aligned} u_j &= -\frac{b}{\left(\mathbf{r}_j - \mathbf{r}_c\right)\mathbf{N}_z}\left(\mathbf{r}_j - \mathbf{r}_c\right)\mathbf{T}_x \\ v_j &= -\frac{b}{\left(\mathbf{r}_j - \mathbf{r}_c\right)\mathbf{N}_z}\left(\mathbf{r}_j - \mathbf{r}_c\right)\mathbf{T}_y \end{aligned}$$

Rewriting and inserting Equation 2.1 produces:

$$\begin{aligned} u_j &= -\frac{b}{\left(\mathbf{r}_j - \mathbf{r}_c\right)\mathbf{N}_z}\mathbf{r}_j\mathbf{T}_x + \frac{b}{\left(\mathbf{r}_j - \mathbf{r}_c\right)\mathbf{N}_z}\mathbf{r}_c\mathbf{T}_x \\ v_j &= -\frac{b}{\left(\mathbf{r}_j - \mathbf{r}_c\right)\mathbf{N}_z}\mathbf{r}_j\mathbf{T}_y + \frac{b}{\left(\mathbf{r}_j - \mathbf{r}_c\right)\mathbf{N}_z}\mathbf{r}_c\mathbf{T}_y \end{aligned}$$

$$\begin{aligned} u_j &= -\frac{b}{\left(\mathbf{r}_j - (\mathbf{r}_0 + g\mathbf{N}_z)\right)\mathbf{N}_z}\mathbf{r}_j\mathbf{T}_x + \frac{b}{\left(\mathbf{r}_j - (\mathbf{r}_0 + g\mathbf{N}_z)\right)\mathbf{N}_z}\mathbf{r}_c\mathbf{T}_x \\ v_j &= -\frac{b}{\left(\mathbf{r}_j - (\mathbf{r}_0 + g\mathbf{N}_z)\right)\mathbf{N}_z}\mathbf{r}_j\mathbf{T}_y + \frac{b}{\left(\mathbf{r}_j - (\mathbf{r}_0 + g\mathbf{N}_z)\right)\mathbf{N}_z}\mathbf{r}_c\mathbf{T}_y \end{aligned}$$

$$u_j = -\frac{b}{(\mathbf{r}_j - \mathbf{r}_0)\,\mathbf{N}_z - g}\mathbf{r}_j\mathbf{T}_x + \frac{b}{(\mathbf{r}_j - \mathbf{r}_0)\,\mathbf{N}_z - g}\mathbf{r}_c\mathbf{T}_x \tag{2.9}$$

$$v_j = -\frac{b}{(\mathbf{r}_j - \mathbf{r}_0)\,\mathbf{N}_z - g}\mathbf{r}_j\mathbf{T}_y + \frac{b}{(\mathbf{r}_j - \mathbf{r}_0)\,\mathbf{N}_z - g}\mathbf{r}_c\mathbf{T}_y \tag{2.10}$$

If it is assumed that $g \gg (\mathbf{r}_j - \mathbf{r}_0)\,\mathbf{N}_z$, which means there is a large distance between camera and calibration pattern, the equations 2.9 and 2.10 can be written as:

$$\begin{aligned} u_j &= \frac{b}{g}\mathbf{r}_j\mathbf{T}_x - \frac{b}{g}\mathbf{r}_c\mathbf{T}_x \\ &= \frac{b}{g}\mathbf{r}_j\mathbf{T}_x + u_0 \end{aligned} \tag{2.11}$$

$$\begin{aligned} v_j &= \frac{b}{g}\mathbf{r}_j\mathbf{T}_y - \frac{b}{g}\mathbf{r}_c\mathbf{T}_y \\ &= \frac{b}{g}\mathbf{r}_j\mathbf{T}_y + v_0 \end{aligned} \tag{2.12}$$

with

$$u_0 = -\frac{b}{g}\mathbf{r}_c\mathbf{T}_x \tag{2.13}$$

$$v_0 = -\frac{b}{g}\mathbf{r}_c\mathbf{T}_y \tag{2.14}$$

As $\frac{b}{g} \equiv m$ is the magnification, equations 2.11 and 2.12 can be written as:

$$u_j = m\mathbf{r}_j\mathbf{T}_x + u_0 \tag{2.15}$$

$$v_j = m\mathbf{r}_j\mathbf{T}_y + v_0 \tag{2.16}$$

Equations 2.15 and 2.16 written as a vector:

$$\begin{pmatrix} u_j \\ v_j \end{pmatrix} = \begin{pmatrix} mx_j\alpha_x + my_j\beta_x + u_0 \\ mx_j\alpha_y + my_j\beta_y + v_0 \end{pmatrix} \tag{2.17}$$

with

$$\mathbf{T}_{x,y} = \begin{pmatrix} \alpha_{x,y} \\ \beta_{x,y} \\ \gamma_{x,y} \end{pmatrix} \tag{2.18}$$

Equation 2.17 gives a direct relation between the coordinates in the sensor plane (u_j, v_j) and the global coordinates in the calibration pattern plane (x_j, y_j) of the j^{th} marker. These are the coordinate pairs, which are obtained through the measurement. Equation 2.17 has the form:

$$\begin{pmatrix} u_j \\ v_j \end{pmatrix} = \begin{pmatrix} Ax_j + By_j + C \\ Dx_j + Ey_j + F \end{pmatrix} \tag{2.19}$$

with A, B, C, D, E and F as the unknowns, which have to be determined. To find these a least-square optimization is used:

$$\Phi_1(A, B, C) = \sum_j (u_j - Ax_j - By_j - C)^2 \rightarrow minimum$$

$$\Phi_2(D, E, F) = \sum_j (v_j - Dx_j - Ey_j - F)^2 \rightarrow minimum$$

Instead of using an optimization algorithm, the optimization problem is solved analytically. Therefore the derivatives of the cost functions $\Phi_{1,2}$ according to the unknowns are needed:

$$\begin{aligned}
\frac{\partial \Phi_1}{\partial A} &= 2\sum_j \left(u_j - Ax_j - By_j - C\right)\left(-x_j\right) \\
&= 2\sum_j \left(-x_j u_j + Ax_j^2 + Bx_j y_j + Cx_j\right) \\
\frac{\partial \Phi_1}{\partial B} &= 2\sum_j \left(u_j - Ax_j - By_j - C\right)\left(-y_j\right) \\
&= 2\sum_j \left(-y_j u_j + Ax_j y_j + By_j^2 + Cx_j y_j\right) \\
\frac{\partial \Phi_1}{\partial C} &= 2\sum_j \left(u_j - Ax_j - By_j - C\right)\left(-1\right) \\
&= 2\sum_j \left(-u_j + Ax_j + By_j + C\right)
\end{aligned}$$

As the derivatives have to be zero to minimize the cost function, it follows:

$$\sum_j \left(Ax_j^2 + Bx_j y_j + Cx_j\right) = \sum_j u_j x_j \tag{2.20}$$

$$\sum_j \left(Ax_j y_j + By_j^2 + Cx_j y_j\right) = \sum_j u_j y_j \tag{2.21}$$

$$\sum_j \left(Ax_j + By_j + C\right) = \sum_j u_j \tag{2.22}$$

Equations 2.20, 2.21 and 2.22 are then combined in a matrix form:

$$\begin{aligned}
\begin{pmatrix} \sum_j x_j^2 & \sum_j x_j y_j & \sum_j x_j \\ \sum_j x_j y_j & \sum_j y_j^2 & \sum_j y_j \\ \sum_j x_j & \sum_j y_j & \sum_j 1 \end{pmatrix} \begin{pmatrix} A \\ B \\ C \end{pmatrix} &= \begin{pmatrix} \sum_j u_j x_j \\ \sum_j u_j y_j \\ \sum_j u_j \end{pmatrix} \\
\mathbf{M} \begin{pmatrix} A \\ B \\ C \end{pmatrix} &= \mathbf{V}_1
\end{aligned}$$

Analogously for D, E and F:

$$\begin{aligned}
\begin{pmatrix} \sum_j x_j^2 & \sum_j x_j y_j & \sum_j x_j \\ \sum_j x_j y_j & \sum_j y_j^2 & \sum_j y_j \\ \sum_j x_j & \sum_j y_j & \sum_j 1 \end{pmatrix} \begin{pmatrix} D \\ E \\ F \end{pmatrix} &= \begin{pmatrix} \sum_j v_j x_j \\ \sum_j v_j y_j \\ \sum_j v_j \end{pmatrix} \\
\mathbf{M} \begin{pmatrix} D \\ E \\ F \end{pmatrix} &= \mathbf{V}_2
\end{aligned}$$

Thus the unknowns are calculated by inverting the matrix $\mathbf{M}$ and multiplying it with the vectors $\mathbf{V}_{1,2}$:

$$\begin{aligned}\begin{pmatrix}A\\B\\C\end{pmatrix} &= \mathbf{M}^{-1}\mathbf{V}_1\\ \begin{pmatrix}D\\E\\F\end{pmatrix} &= \mathbf{M}^{-1}\mathbf{V}_2\end{aligned}$$

The matrix $\mathbf{M}$ is stable once $N \gg 9$. Now A, B, C, D, E and F are known.

2.4.2. Calculating the Camera Parameters

Principal Point of the Camera Position Vector with the Sensor Plane

Equations 2.17 and 2.19 show that $C = u_0$ and $F = v_0$. Therefore the principal point of the camera position vector with the sensor plane is:

$$\rho_0 = \begin{pmatrix}u_0\\v_0\end{pmatrix} = \begin{pmatrix}C\\F\end{pmatrix}$$

Magnification

As $\mathbf{T}_x$ and $\mathbf{T}_y$ are unit vectors, it applies according to the definitions of A, B, D and E:

$$\begin{aligned}\alpha_x^2 + \beta_x^2 + \gamma_x^2 &= 1\\ m^2\alpha_x^2 + m^2\beta_x^2 + m^2\gamma_x^2 &= m^2\\ A^2 + B^2 + m^2\gamma_x^2 &= m^2\end{aligned} \tag{2.23}$$

$$\begin{aligned}\alpha_y^2 + \beta_y^2 + \gamma_y^2 &= 1\\ m^2\alpha_y^2 + m^2\beta_y^2 + m^2\gamma_y^2 &= m^2\\ D^2 + E^2 + m^2\gamma_y^2 &= m^2\end{aligned} \tag{2.24}$$

Subtracting equation 2.24 from equation 2.23 results in:

$$\begin{aligned}A^2 - D^2 + B^2 - E^2 + m^2\left(\gamma_x^2 - \gamma_y^2\right) &= 0\\ m^2\left(\gamma_x^2 - \gamma_y^2\right) &= D^2 - A^2 + E^2 - B^2\end{aligned} \tag{2.25}$$

$\mathbf{T}_x$ and $\mathbf{T}_y$ are orthogonal, so it applies:

$$\begin{aligned}\gamma_x\gamma_y &= -\left(\alpha_x\alpha_y + \beta_x\beta_y\right)\\ m^2\gamma_x\gamma_y &= -\left(AD + BE\right)\end{aligned} \tag{2.26}$$

Looking at

$$m^2\left(\gamma_x - i\gamma_y\right)^2 = m^2\left(\gamma_x^2 - \gamma_y^2\right) - 2im^2\left(\gamma_x\gamma_y\right) \tag{2.27}$$

equations 2.25 and 2.26 are found on the right side. Therefore equation 2.27 can be written as:

$$\begin{aligned} m^2\left(\gamma_x - i\gamma_y\right)^2 &= \left(D^2 - A^2 + E^2 - B^2\right) + 2i\left(AD + BE\right) \\ m\left(\gamma_x - i\gamma_y\right) &= \pm\sqrt{\left(D^2 - A^2 + E^2 - B^2\right) + 2i\left(AD + BE\right)} \end{aligned}$$

$$m\gamma_x = \pm\Re\sqrt{\left(D^2 - A^2 + E^2 - B^2\right) + 2i\left(AD + BE\right)} \equiv P \tag{2.28}$$

$$m\gamma_y = \mp\Im\sqrt{\left(D^2 - A^2 + E^2 - B^2\right) + 2i\left(AD + BE\right)} \equiv Q \tag{2.29}$$

Inserting equations 2.28 and 2.29 into equations 2.23 and 2.24 gives a compact form for calculating the magnification m:

$$\begin{aligned} D^2 + E^2 + P^2 &= m^2 \\ A^2 + B^2 + Q^2 &= m^2 \end{aligned}$$

Due to the fact that there are two equations for calculating the magnification m, there is the possibility for verification and averaging respectively.

Principal Point of the Camera Axis with the Calibration Pattern Plane

Inserting equation 2.1 into equations 2.13 and 2.14 results in:

$$\begin{aligned} u_0 &= -\frac{b}{g}\left(\mathbf{r}_0 + g\mathbf{N}_z\right)\mathbf{T}_x \\ &= -m\left(\mathbf{r}_0\mathbf{T}_x + g\mathbf{N}_z\mathbf{T}_x\right) \\ &= -m\left(\mathbf{r}_0\mathbf{T}_x\right) \end{aligned}$$

$$\begin{aligned} v_0 &= -\frac{b}{g}\left(\mathbf{r}_0 + g\mathbf{N}_z\right)\mathbf{T}_y \\ &= -m\left(\mathbf{r}_0\mathbf{T}_y + g\mathbf{N}_z\mathbf{T}_y\right) \\ &= -m\left(\mathbf{r}_0\mathbf{T}_y\right) \end{aligned}$$

or as a vector:

$$\begin{pmatrix} u_0 \\ v_0 \end{pmatrix} = -m\begin{pmatrix} \alpha_x & \beta_x \\ \alpha_y & \beta_y \end{pmatrix}\begin{pmatrix} x_0 \\ y_0 \end{pmatrix} \tag{2.30}$$

Rewriting equation 2.30 produces the principal point of the camera axis with the calibration pattern plane:

$$\mathbf{r}_0 = \begin{pmatrix} x_0 \\ y_0 \end{pmatrix} = -\frac{1}{m}\begin{pmatrix} \alpha_x & \beta_x \\ \alpha_y & \beta_y \end{pmatrix}^{-1}\begin{pmatrix} u_0 \\ v_0 \end{pmatrix}$$

Tangential and Normal Camera Vectors

With equations 2.18, 2.28 and 2.29 the equations for calculating the tangential camera vectors are:

$$\mathbf{T}_x = \frac{1}{m}\begin{pmatrix} m\alpha_x \\ m\beta_x \\ m\gamma_x \end{pmatrix} = \frac{1}{m}\begin{pmatrix} A \\ B \\ sP \end{pmatrix}$$

$$\mathbf{T}_y = \frac{1}{m}\begin{pmatrix} m\alpha_y \\ m\beta_y \\ m\gamma_y \end{pmatrix} = \frac{1}{m}\begin{pmatrix} D \\ E \\ sQ \end{pmatrix}$$

As the camera sensor coordinate system is an orthogonal right-handed one, the normal vector $\mathbf{N}_z$ is calculated as the vector product of $\mathbf{T}_x$ and $\mathbf{T}_y$:

$$\mathbf{N}_z = \mathbf{T}_x \times \mathbf{T}_y = \frac{1}{m^2}\begin{pmatrix} s\,(BQ - EP) \\ s\,(DP - AQ) \\ AE - BD \end{pmatrix}$$

with $s = \pm 1$ depending on the estimated $\mathbf{N}_z$. The vector is calculated with both signs and then the scalar product of $\mathbf{N}_z$ and $\mathbf{N}_{z,est}$ which is the smallest, gives the right sign.

Image and Object Distances

As the focal length f must be given, the image distance b is calculated from the thin lens equation ([Brenner 2007]) as follows:

$$\begin{aligned} \frac{1}{f} &= \frac{1}{b} + \frac{1}{g} \\ \Rightarrow f &= \frac{bg}{b+g} \\ &= \frac{b}{\frac{b}{g}+1} \\ &= \frac{b}{m+1} \\ \Rightarrow b &= f\,(m+1) \end{aligned}$$

With the definition of the magnification $m \equiv \frac{b}{g}$ the object distance is:

$$g = \frac{b}{m}$$

Camera Center

The camera center follows directly from equation 2.1:

$$\mathbf{r}_c = \mathbf{r}_0 + g\mathbf{N}_z$$

Tilt Angle

The tangential vectors orthogonal to the plane $(\mathbf{e}_y, \mathbf{N}_z)$ are:

$$\begin{aligned} \mathbf{T}_{0x} &= \mathbf{e}_y \times \mathbf{N}_z \\ \mathbf{T}_{0y} &= \mathbf{N}_z \times \mathbf{T}_{0x} \end{aligned}$$

And the tilt angle φ of the camera sensor (Figure 2.2) in respect to $\mathbf{T}_{0x}$ and $\mathbf{T}_{0y}$ is calculated as follows:

$$\begin{aligned} \mathbf{T}_x \cdot \mathbf{T}_{0x} &= \cos(\alpha) \\ \mathbf{T}_y \cdot \mathbf{T}_{0x} &= \cos\left(\alpha + \frac{\pi}{2}\right) = -\sin(\alpha) \\ \rightarrow \alpha &= \arctan 2\left(-\mathbf{T}_y \cdot \mathbf{T}_{0x}, \mathbf{T}_x \cdot \mathbf{T}_{0x}\right) \end{aligned}$$

$$\begin{aligned} \mathbf{T}_y \cdot \mathbf{T}_{0y} &= \cos(\beta) \\ \mathbf{T}_y \cdot \mathbf{T}_{0y} &= \cos\left(\frac{\pi}{2} - \beta\right) = \sin(\beta) \\ \rightarrow \beta &= \arctan 2\left(\mathbf{T}_x \cdot \mathbf{T}_{0y}, \mathbf{T}_y \cdot \mathbf{T}_{0y}\right) \end{aligned}$$

$$\Rightarrow \varphi = \frac{\alpha + \beta}{2}$$

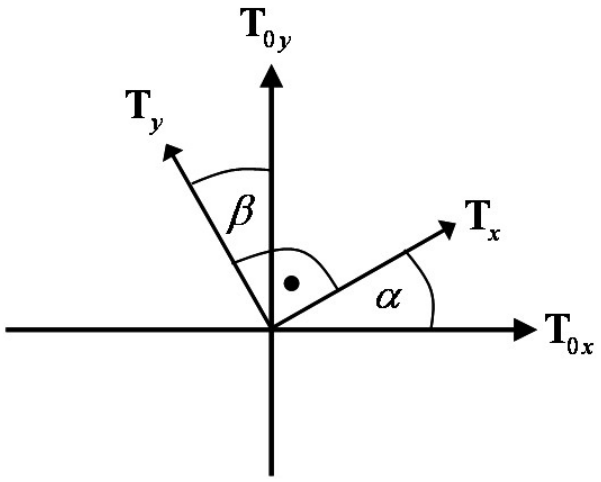

Figure 2.2.: Tilt angle of camera sensor

2.5. Non-linear Optimization

It is necessary to perform a non-linear optimization of the camera parameters to exclude the errors resulting from the linear approximation ($g \gg (\mathbf{r}_j - \mathbf{r}_0)\,\mathbf{N}_z$). The parameters obtained from the linear reconstruction are utilized as the starting point of the optimization process.

2.5.1. Optimization Parameters

As optimization parameters the camera center $\mathbf{r}_c$, the principal point of the camera axis with the calibration pattern plane $\mathbf{r}_0$ and the tilt angle of the sensor φ are used. So the optimization parameter vector $\mathbf{p}$ is:

$$\mathbf{p} = \begin{pmatrix} x_c \\ y_c \\ z_c \\ x_0 \\ y_0 \\ \varphi \end{pmatrix}$$

If the camera sensor is not on the optical axis and geometrical distortions occur in the imaging system, the optimization vector is supplemented with the interception point of the optical axis with the sensor plane $\mathbf{r}_{cs} = \begin{pmatrix} x_{cs} \\ y_{cs} \end{pmatrix}$ and the distortion coefficients c_0 and c_2:

$$\mathbf{p} = \begin{pmatrix} x_c \\ y_c \\ z_c \\ x_0 \\ y_0 \\ \varphi \\ x_{cs} \\ y_{cs} \\ c_0 \\ c_2 \end{pmatrix}$$

Given the distance d of one pixel to the sensor center and the original coordinate of one pixel $\mathbf{r}$ the distortion is described as follows:

$$\mathbf{r}_{dist} = (c_0 + c_2 \cdot d)\,\mathbf{r}$$

c_0 is a linear distortion (magnification factor) and c_2 is a second order factor to describe barrel or pincushion distortion.

2.5.2. Camera Parameters

It has to be ensured that the remaining camera parameters can be calculated from the optimization parameters. From the following equations it can be seen that the parameter

vector $\mathbf{p}$ is sufficient to derive the remaining camera parameters.

$$\begin{aligned}
\mathbf{N}_z &= \frac{\mathbf{r}_c - \mathbf{r}_0}{|\mathbf{r}_c - \mathbf{r}_0|} \\
\mathbf{T}_{0x} &= \mathbf{e}_y \times \mathbf{N}_z \\
\mathbf{T}_{0y} &= \mathbf{N}_z \times \mathbf{T}_{0x} \\
\mathbf{T}_x &= \cos(\varphi)\,\mathbf{T}_{0x} + \sin(\varphi)\,\mathbf{T}_{0y} \\
\mathbf{T}_y &= \cos(\varphi)\,\mathbf{T}_{0y} - \sin(\varphi)\,\mathbf{T}_{0x} \\
g &= |\mathbf{r}_c - \mathbf{r}_0| \\
b &= \frac{gf}{g - f}
\end{aligned}$$

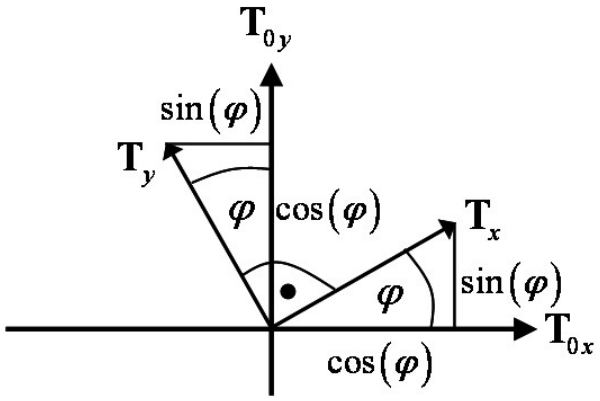

Figure 2.3.: Tilt angle of camera sensor

2.5.3. Goal Function

The goal function, which has to be minimized is:

$$\Phi_{goal}(\mathbf{p}) = \sum_{i=0}^{N-1} \left[\left(u_{found,i} - u_{calc,i}(\mathbf{p})\right)^2 + \left(v_{found,i} - v_{calc,i}(\mathbf{p})\right)^2 \right]$$

$u_{found,i}$ / $v_{found,i}$ are the coordinates of the image of the i^{th} marker in the sensor plane obtained by a measurement. $u_{calc,i}(\mathbf{p})$ / $v_{calc,i}(\mathbf{p})$ are the coordinates of the image of the i^{th} marker in the sensor plane calculated with the actual camera parameters $\mathbf{p}$ from the global position of the i^{th} marker $(x_s, y_s)_i$ in the calibration pattern plane (Figure 2.4).

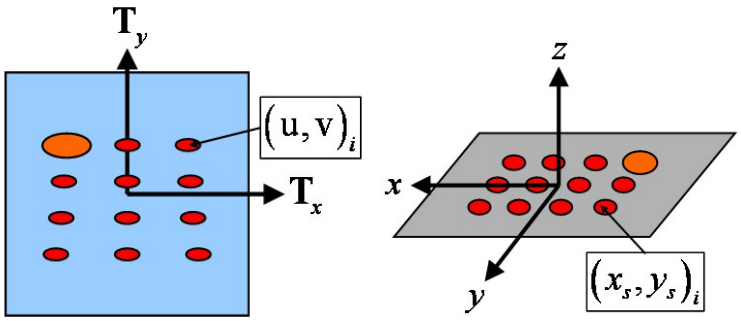

(a) Sensor plane (b) Calibration pattern plane

Figure 2.4.: Coordinates of one marker

$u_{calc,i}$ and $v_{calc,i}$ are calculated as follows:

$$\begin{aligned} \mathbf{D}_i &= \begin{pmatrix} x_{s,i} \\ y_{s,i} \\ 0 \end{pmatrix} - \mathbf{r}_c \\ g_i &= -\mathbf{D}_i + \mathbf{N}_z \\ m_i &= \frac{b}{g_i} \end{aligned}$$

$$\begin{aligned} u_{calc,i} &= m_i \left(\mathbf{D}_i \mathbf{T}_x \right) \\ v_{calc,i} &= m_i \left(\mathbf{D}_i \mathbf{T}_y \right) \end{aligned}$$

The goal function Φ_{goal} is minimized by Newton's method to find a root of a function.

2.5.4. Newton's Method

Newton's method is an iterative algorithm to find approximated solutions for:

$$f(x) = 0$$

The basic idea is that the function $f(x)$ is assumed to be linear at a starting point x_n of the iteration step n, so the root of the tangent at x_n is used as an approximation for the root of $f(x)$ [Bronstein et al. 1999]. Thus the step size dx_n at the n^{th} iteration is:

$$\begin{aligned} \frac{f(x)}{dx_n} &= -f'(x_n) \\ \Rightarrow dx_n &= -\frac{f(x_n)}{f'(x_n)} \end{aligned}$$

The new starting point x_{n+1} of the next iteration $n+1$ is:

$$\begin{aligned} x_{n+1} &= x_n + dx_n \\ x_{n+1} &= x_n - \frac{f(x_n)}{f'(x_n)} \end{aligned}$$

Therefore the equation that is iteratively solved is:

$$f(x+dx) = f(x) + f'(x) \cdot dx = 0 \tag{2.31}$$

with the step size $dx = -\frac{f(x)}{f'(x)}$.

For the non-linear optimization of the camera parameters x is the vector $\mathbf{p}$ and $f(x)$ is the gradient of the function $\Phi_{goal}(\mathbf{p})$. Then the equation which has to be solved is:

$$\nabla\Phi_{goal}(\mathbf{p}) = \mathbf{0}$$

Inserting this in Equation 2.31 gives:

$$\nabla\Phi_{goal}(\mathbf{p}+d\mathbf{p}) = \nabla\Phi_{goal}(\mathbf{p}) + \mathbf{H} \cdot d\mathbf{p} = \mathbf{0}$$

with the Hesse matrix $\mathbf{H} = \frac{\partial^2\Phi_{goal}}{\partial p_i \partial p_j}$. The step size $d\mathbf{p}_n$ at the n^{th} iteration then is:

$$d\mathbf{p}_n = -\mathbf{H}^{-1}(\mathbf{p}_n)\nabla\Phi_{goal}(\mathbf{p}_n)$$

And the starting point $\mathbf{p}_{n+1}$ of the iteration $n+1$ is:

$$\begin{aligned} \mathbf{p}_{n+1} &= \mathbf{p}_n + d\mathbf{p}_n \\ \mathbf{p}_{n+1} &= \mathbf{p}_n - \mathbf{H}^{-1}(\mathbf{p}_n)\nabla\Phi_{goal}(\mathbf{p}_n) \end{aligned}$$

2.6. Marker Identification

The centroid search and the filtering is performed in exactly the same way as in the case of the deflectometry (1.5.1 and 1.5.2).

2.6.1. Grid Identification

Both axes of the pattern are found by looking at the distance between the markers and the reference marker. From geometrical consideration follows that the closest marker must lie on one of the axes. So the vector

$$\mathbf{e}_{axis1} = \frac{\mathbf{r}_{i,c} - \mathbf{r}_{ref}}{|\mathbf{r}_{i,c} - \mathbf{r}_{ref}|}$$

is the unit vector of one axis. $\mathbf{r}_{i,c}$ is the coordinate of the closest marker and $\mathbf{r}_{ref}$ the coordinate of the reference marker. The marker which is the next closest to the reference marker and has an angle larger than 45° to the first found vector defines the second axis:

$$\mathbf{e}_{axis2} = \frac{\mathbf{r}_{i,nc} - \mathbf{r}_{ref}}{|\mathbf{r}_{i,nc} - \mathbf{r}_{ref}|}$$

At this point it is not known which axis is the x/y-axis. Since the coordinate system is right-handed, the assignment is done by calculating both possible vector products of the found vectors, which gives the possible unit vectors of the z-axis. As the camera always is at the positive side of the z-axis, the unit vector in z-direction must have a positive z-value.

These found axes are then used to get the periods p_x and p_y of the pattern and the indexing is done as it is described in 1.5.4.

2.7. Calibrating the Deflectometry Setup

The calibration of the deflectometric setup is performed in three steps. First the camera position relative to the substrate plane – defined by the holding frame – is obtained. Then the camera position relative to the pattern is evaluated. In the last step these two calibrations are combined so that the substrate plane, the pattern and the camera are in one global coordinate system. This is made possible as the camera is in the same position in both calibration measurements.

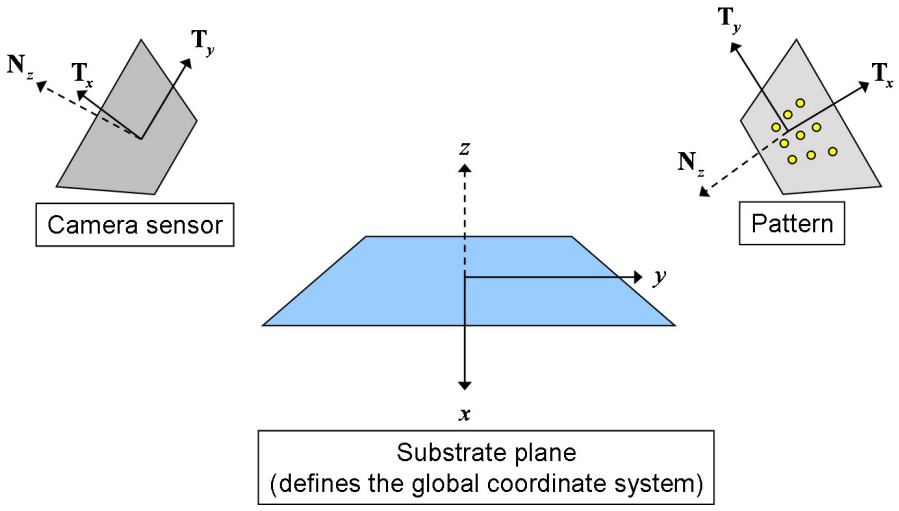

Figure 2.5.: Geometry

2.7.1. Substrate Plane

The camera calibration of the substrate plane is done with the help of a calibration pattern lying on the holding frame. This calibration pattern defines the global coordinate system. Therefore the values obtained from this measurement are the global camera parameters.

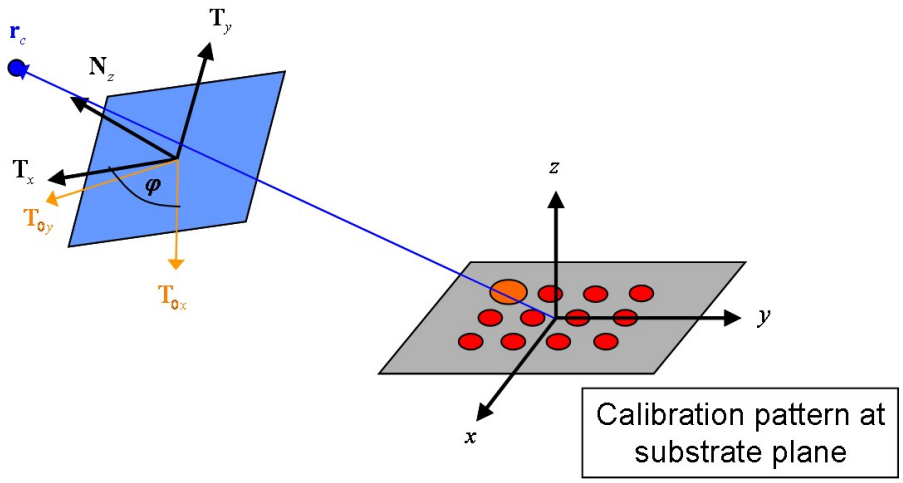

Figure 2.6.: Calibration of the substrate plane

2.7.2. Pattern

To get the position and tilt of the deflectometry pattern, an optical flat mirror is placed on the holding frame, so that the pattern can be observed with the camera in reflection. Due to the reflection the resulting calibration values provide the camera parameters related to a virtual mirrored pattern, lying on the unfold optical path (Figure 2.7). The

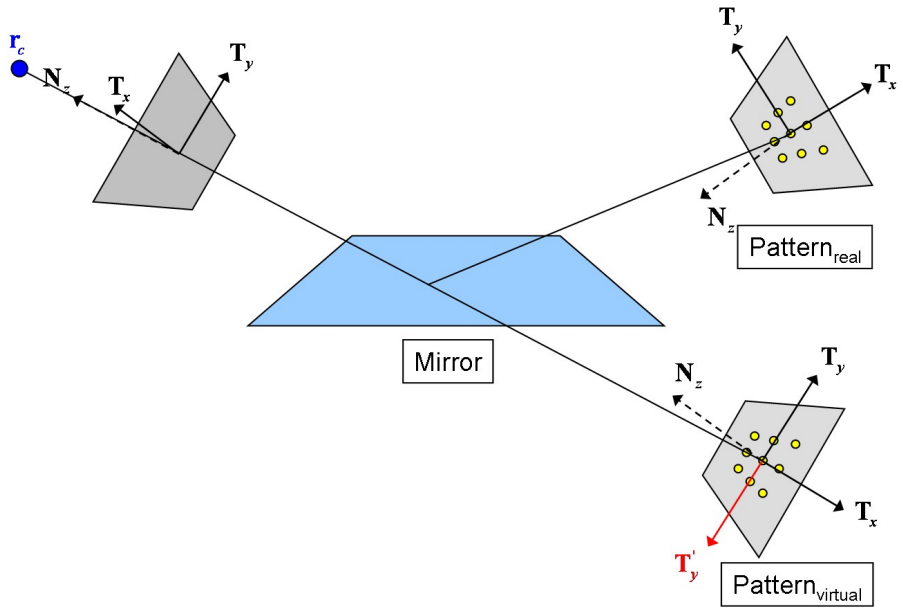

Figure 2.7.: Calibration of the pattern

camera parameters have to be transformed to take the mirror into account and to get the real position and tilt of the deflectometry pattern. This step is made after these camera parameters have been transferred to the global coordinate system.

Global Pattern Parameters

To obtain the virtual pattern parameters $\mathbf{r}$, $\mathbf{T}_x$, $\mathbf{T}_y$ and $\mathbf{N}_z$ in the global coordinate system the pattern parameters are first transferred to the camera's coordinate system as the global camera parameters are known from the substrate calibration.

$$(\mathbf{r}, \mathbf{T}_x, \mathbf{T}_y, \mathbf{N}_z)^{camera,pattern_v} \rightarrow (\mathbf{r}, \mathbf{T}_x, \mathbf{T}_y, \mathbf{N}_z)^{pattern_v,camera}$$

$$\begin{aligned}
r_x^{pattern_v,camera} &= -\mathbf{r}^{camera,pattern_v} \cdot \mathbf{T}_x^{camera,pattern_v} \\
r_y^{pattern_v,camera} &= -\mathbf{r}^{camera,pattern_v} \cdot \mathbf{T}_y^{camera,pattern_v} \\
r_z^{pattern_v,camera} &= -\mathbf{r}^{camera,pattern_v} \cdot \mathbf{N}_z^{camera,pattern_v}
\end{aligned}$$

$$\begin{aligned}
T_{x,x}^{pattern_v,camera} &= \mathbf{e}_x \cdot \mathbf{T}_x^{camera,pattern_v} \\
T_{x,y}^{pattern_v,camera} &= \mathbf{e}_x \cdot \mathbf{T}_y^{camera,pattern_v} \\
T_{x,z}^{pattern_v,camera} &= \mathbf{e}_x \cdot \mathbf{N}_z^{camera,pattern_v}
\end{aligned}$$

$$\begin{aligned}
T_{y,x}^{pattern_v,camera} &= \mathbf{e}_y \cdot \mathbf{T}_x^{camera,pattern_v} \\
T_{y,y}^{pattern_v,camera} &= \mathbf{e}_y \cdot \mathbf{T}_y^{camera,pattern_v} \\
T_{y,z}^{pattern_v,camera} &= \mathbf{e}_y \cdot \mathbf{N}_z^{camera,pattern_v}
\end{aligned}$$

$$\begin{aligned}
N_{z,x}^{pattern_v,camera} &= \mathbf{e}_z \cdot \mathbf{T}_x^{camera,pattern_v} \\
N_{z,y}^{pattern_v,camera} &= \mathbf{e}_z \cdot \mathbf{T}_y^{camera,pattern_v} \\
N_{z,z}^{pattern_v,camera} &= \mathbf{e}_z \cdot \mathbf{N}_z^{camera,pattern_v}
\end{aligned}$$

Now the virtual pattern parameters are known in the camera's coordinate system and can be transferred to the global coordinate system:

$$(\mathbf{r}, \mathbf{T}_x, \mathbf{T}_y, \mathbf{N}_z)^{pattern_v,camera} \rightarrow (\mathbf{r}, \mathbf{T}_x, \mathbf{T}_y, \mathbf{N}_z)^{pattern_v,global}$$

$$\begin{aligned}
\mathbf{r}^{pattern_v,global} = \; & \mathbf{r}^{camera,global} \\
& + r_x^{pattern_v,camera} \cdot \mathbf{T}_x^{camera,global} \\
& + r_y^{pattern_v,camera} \cdot \mathbf{T}_y^{camera,global} \\
& + r_z^{pattern_v,camera} \cdot \mathbf{N}_z^{camera,global}
\end{aligned}$$

$$\begin{aligned}
\mathbf{T}_x^{pattern_v,global} = \; & T_{x,x}^{pattern_v,camera} \cdot \mathbf{T}_x^{camera,global} \\
& + T_{x,y}^{pattern_v,camera} \cdot \mathbf{T}_y^{camera,global} \\
& + T_{x,z}^{pattern_v,camera} \cdot \mathbf{N}_z^{camera,global}
\end{aligned}$$

$$\begin{aligned}
\mathbf{T}_y^{pattern_v,global} = \; & T_{y,x}^{pattern_v,camera} \cdot \mathbf{T}_x^{camera,global} \\
& + T_{y,y}^{pattern_v,camera} \cdot \mathbf{T}_y^{camera,global} \\
& + T_{y,z}^{pattern_v,camera} \cdot \mathbf{N}_z^{camera,global}
\end{aligned}$$

$$\begin{aligned}\mathbf{N}_z^{pattern_v,global} &= N_{z,x}^{pattern_v,camera} \cdot \mathbf{T}_x^{camera,global} \\ &+N_{z,y}^{pattern_v,camera} \cdot \mathbf{T}_y^{camera,global} \\ &+N_{z,z}^{pattern_v,camera} \cdot \mathbf{N}_z^{camera,global}\end{aligned}$$

The global parameters of the virtual pattern are now known. The global parameters of the real pattern are obtained by taking the reflection into account. The mirror, by definition, lies exactly in the x/y-plane of the global coordinate system. So the transformation can be achieved by just inverting the z-components of the parameters with one exception: $\mathbf{T}_y$ has to be inverted completely after inverting the z-component as the coordinate system of the real pattern has to be right-handed (Figure 2.8).

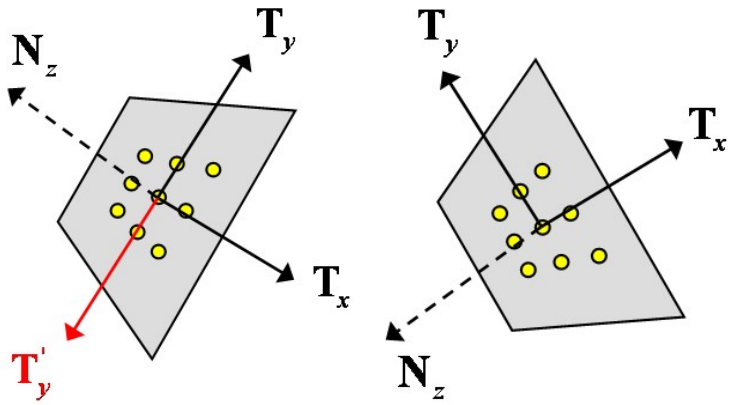

(a) Virtual pattern (b) Real pattern

Figure 2.8.: Taking the mirror into account

$$\mathbf{r}^{pattern_r,global} = \begin{pmatrix} r_x^{pattern_v,global} \\ r_y^{pattern_v,global} \\ -r_z^{pattern_v,global} \end{pmatrix}$$

$$\mathbf{T}_x^{pattern_r,global} = \begin{pmatrix} T_{x,x}^{pattern_v,global} \\ T_{x,y}^{pattern_v,global} \\ -T_{x,z}^{pattern_v,global} \end{pmatrix}$$

$$\mathbf{T}_y^{pattern_r,global} = -\begin{pmatrix} T_{y,x}^{pattern_v,global} \\ T_{y,y}^{pattern_v,global} \\ -T_{y,z}^{pattern_v,global} \end{pmatrix} = \begin{pmatrix} -T_{y,x}^{pattern_v,global} \\ -T_{y,y}^{pattern_v,global} \\ T_{y,z}^{pattern_v,global} \end{pmatrix}$$

$$\mathbf{N}_z^{pattern_r,global} = \begin{pmatrix} N_{z,x}^{pattern_v,global} \\ N_{z,y}^{pattern_v,global} \\ -N_{z,z}^{pattern_v,global} \end{pmatrix}$$

After this step the global parameters of the camera, of the pattern and – by definition – of the substrate plane are known and the calibration of the complete deflectometry setup is finished.

2.8. Simulations

2.8.1. Non-linear Optimization

To demonstrate the influence of the non-linear optimization, a calibration with only the linear-reconstruction of the camera parameters is compared to a calibration with the linear-reconstruction and a non-linear optimization which follows afterwards.

Perpendicular View

The center of the simulated camera is $\mathbf{r}_c = \begin{pmatrix} 0 \\ 0 \\ 233.24 \end{pmatrix} mm$, the vectors defining the local coordinate system of the sensor are $\mathbf{T}_x = \begin{pmatrix} 1 \\ 0 \\ 0 \end{pmatrix}$, $\mathbf{T}_y = \begin{pmatrix} 0 \\ 1 \\ 0 \end{pmatrix}$ and $\mathbf{N}_z = \begin{pmatrix} 0 \\ 0 \\ 1 \end{pmatrix}$. The image distance is $b = 28mm$ and the focal length $f = 25mm$.

The marker centers calculated in the optimization step were compared to the ones found in the image rendered with the original parameters to estimate the accuracy of the calibration. In Table 2.2 the deviations from the correct values and the root-mean-square and peak-to-valley values of the marker center comparison are listed. For the non-linear optimization, the linear parameters were used as start values.

Camera parameter	linear	non-linear
$\Delta\mathbf{r}_c$	$\begin{pmatrix} 1.432 \cdot 10^{-7} \\ 5.017 \cdot 10^{-6} \\ -2.842 \cdot 10^{-14} \end{pmatrix} mm$	$\begin{pmatrix} 1.79 \cdot 10^{-13} \\ -6.787 \cdot 10^{-14} \\ 0 \end{pmatrix} mm$
$\Delta\mathbf{T}_x$	$\begin{pmatrix} -1.11 \cdot 10^{-16} \\ 0 \\ -6.141 \cdot 10^{-10} \end{pmatrix}$	$\begin{pmatrix} -1.11 \cdot 10^{-16} \\ -2.009 \cdot 10^{-18} \\ -7.673 \cdot 10^{-16} \end{pmatrix}$
$\Delta\mathbf{T}_y$	$\begin{pmatrix} -1.321 \cdot 10^{-17} \\ -2.22 \cdot 10^{-16} \\ -2.151 \cdot 10^{-8} \end{pmatrix}$	$\begin{pmatrix} 2.009 \cdot 10^{-18} \\ 1.11 \cdot 10^{-16} \\ 2.912 \cdot 10^{-16} \end{pmatrix}$
$\Delta\mathbf{N}_z$	$\begin{pmatrix} 6.141 \cdot 10^{-10} \\ 2.151 \cdot 10^{-8} \\ -1.11 \cdot 10^{-16} \end{pmatrix}$	$\begin{pmatrix} 7.673 \cdot 10^{-16} \\ -2.912 \cdot 10^{-16} \\ 0 \end{pmatrix}$
Δb	$0mm$	$0mm$
root-mean-square value	$1.063 \cdot 10^{-9}mm$	$4.722 \cdot 10^{-16}mm$
peak-to-valley value	$1.953 \cdot 10^{-9}mm$	$1.110 \cdot 10^{-15}mm$

Table 2.2.: Comparison of reconstructed camera parameters for perpendicular view

Angular View

The center of the simulated camera lies at $\mathbf{r}_c = \begin{pmatrix} 0 \\ -200 \\ 120 \end{pmatrix} mm$, the vectors of the local coordinate system of the sensor are $\mathbf{T}_x = \begin{pmatrix} 1 \\ 0 \\ 0 \end{pmatrix}$, $\mathbf{T}_y = \begin{pmatrix} 0 \\ 0.5145 \\ 0.8575 \end{pmatrix}$ and $\mathbf{N}_z = \begin{pmatrix} 0 \\ -0.8575 \\ 0.5145 \end{pmatrix}$. The image distance is $b = 28mm$ and the focal length $f = 25mm$.

Table 2.3 shows the deviations from the correct values and the root-mean-square and peak-to-valley values of the marker center comparison.

Camera parameter	linear	non-linear
$\Delta\mathbf{r}_c$	$\begin{pmatrix} -1.557 \cdot 10^{-15} \\ 4.366 \cdot 10^{-1} \\ -1.485 \cdot 10^{-2} \end{pmatrix} mm$	$\begin{pmatrix} 6.071 \cdot 10^{-15} \\ 3.126 \cdot 10^{-13} \\ 3.979 \cdot 10^{-13} \end{pmatrix} mm$
$\Delta\mathbf{T}_x$	$\begin{pmatrix} 0 \\ 0 \\ 7.698 \cdot 10^{-18} \end{pmatrix}$	$\begin{pmatrix} 0 \\ 1.289 \cdot 10^{-17} \\ -3.053 \cdot 10^{-17} \end{pmatrix}$
$\Delta\mathbf{T}_x$	$\begin{pmatrix} -6.6 \cdot 10^{-18} \\ 3.342 \cdot 10^{-4} \\ -2.006 \cdot 10^{-4} \end{pmatrix}$	$\begin{pmatrix} 1.955 \cdot 10^{-17} \\ 1.665 \cdot 10^{-15} \\ -1.221 \cdot 10^{-15} \end{pmatrix}$
$\Delta\mathbf{N}_z$	$\begin{pmatrix} -3.963 \cdot 10^{-18} \\ 2.006 \cdot 10^{-4} \\ 3.342 \cdot 10^{-4} \end{pmatrix}$	$\begin{pmatrix} 2.676 \cdot 10^{-17} \\ 1.221 \cdot 10^{-15} \\ 1.665 \cdot 10^{-15} \end{pmatrix}$
Δb	$2.6 \cdot 10^{-3} mm$	$0mm$
root-mean-square value	$1.477 \cdot 10^{-2} mm$	$9.076 \cdot 10^{-15} mm$
peak-to-valley value	$4.934 \cdot 10^{-3} mm$	$1.719 \cdot 10^{-14} mm$

Table 2.3.: Comparison of reconstructed camera parameters for angular view

The results show, that the non-linear optimization has a strong influence on the accuracy of the calibration, which is clearly seen in the root-mean-square and peak-to-valley values of the marker center comparison. For the non-perpendicular look at the pattern the non-linear optimization is particularly essential.

2.8.2. Accuracy of the Centroid Search

The markers are spatially extended spots, hence there is a dependency of the accuracy of the centroid search on the viewing angle. To analyze this, a scan over the viewing angle is performed and the found centroid coordinates of the markers are compared to the exact position of the marker centers on the camera sensor.

The distance d of the camera center $\mathbf{r}_c$ from the center of the calibration pattern is kept constant, so that $d = |\mathbf{r}_c| = 233,24mm$ (Figure 2.9). The angle starts at $\alpha = 90°$

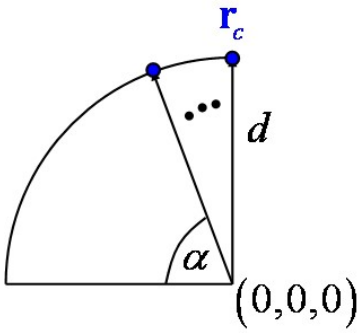

Figure 2.9.: Angle scan setup

(Figure 2.10(a)) and is diminished by $\Delta\alpha = 10°$ down to $\alpha = 10°$ (Figure 2.10(b)).

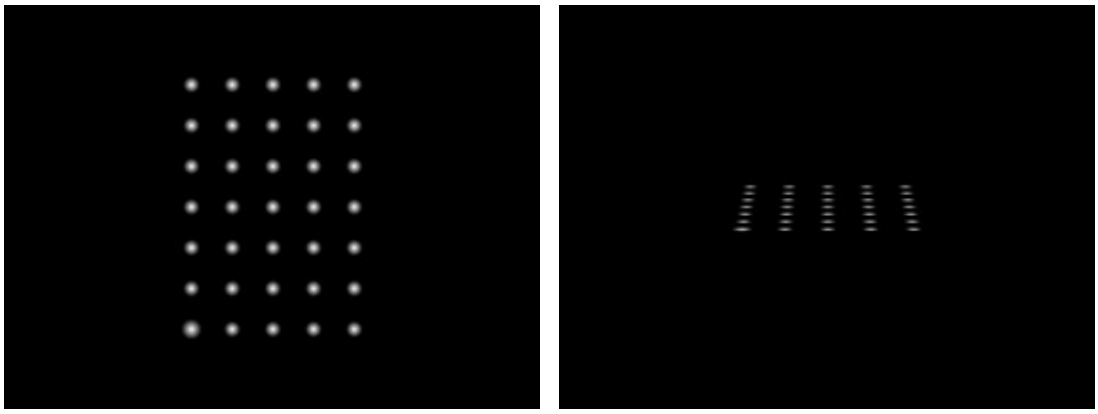

(a) $\alpha = 90°$ (b) $\alpha = 10°$

Figure 2.10.: Camera images

The camera pixels have a square shape with an edge length of $4.65\mu m$. Thus the diagrams in Figure 2.11(a) and Figure 2.11(a) show that the accuracy of the centroid search lies between $\frac{1}{40}$ and $\frac{1}{20}$ pixel.

The impact of the accuracy on the camera calibration is analyzed by adding a distortion to the exact marker coordinates in the sensor plane and performing a calibration with these disturbed positions. The standard deviation of the distortion is $0.233\mu m$, which represents the worst-case accuracy of $\frac{1}{20}$ pixel. The maximum distortion is $0.70\mu m$. The position of the camera center $\mathbf{r}_c$ is chosen so that the viewing angle is about 30°. Table 2.4 shows the deviation from the camera parameters with and without distortion.

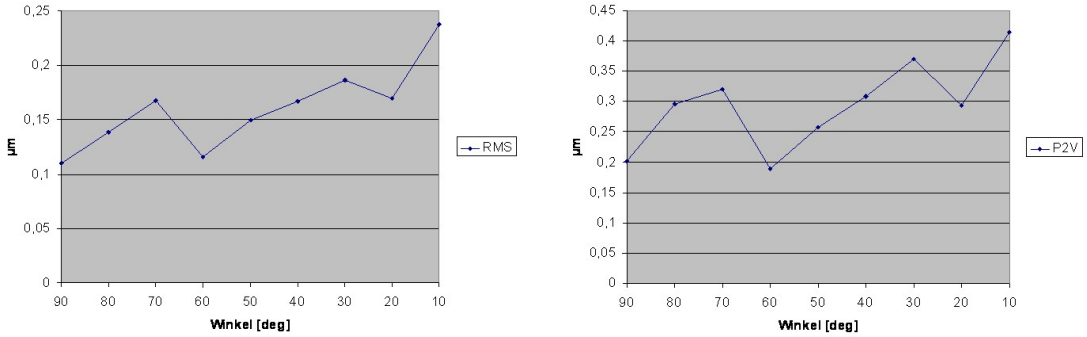

(a) Root-mean-square values of the deviation (b) Peak-to-valley values of the deviation

Figure 2.11.: Angle scan

Camera parameter	with distortion	without distortion
$\Delta\mathbf{r}_c$	$\begin{pmatrix} 1.09 \cdot 10^{-3} \\ 5.72 \cdot 10^{-3} \\ 6.91 \cdot 10^{-3} \end{pmatrix} mm$	$\begin{pmatrix} 1.59 \cdot 10^{-16} \\ 0 \\ 1.42 \cdot 10^{-14} \end{pmatrix} mm$
$\Delta\mathbf{T}_x$	$\begin{pmatrix} 4.32 \cdot 10^{-11} \\ 1.17 \cdot 10^{-6} \\ 9.22 \cdot 10^{-6} \end{pmatrix}$	$\begin{pmatrix} 0 \\ 5.42 \cdot 10^{-18} \\ 1.00 \cdot 10^{-17} \end{pmatrix}$
$\Delta\mathbf{T}_y$	$\begin{pmatrix} 7.31 \cdot 10^{-6} \\ 1.03 \cdot 10^{-5} \\ 6.21 \cdot 10^{-6} \end{pmatrix}$	$\begin{pmatrix} 1.14 \cdot 10^{-17} \\ 0 \\ 1.11 \cdot 10^{-16} \end{pmatrix}$
$\Delta\mathbf{N}_z$	$\begin{pmatrix} 5.74 \cdot 10^{-6} \\ 6.21 \cdot 10^{-6} \\ 1.03 \cdot 10^{-5} \end{pmatrix}$	$\begin{pmatrix} 5.25 \cdot 10^{-19} \\ 1.11 \cdot 10^{-16} \\ 0 \end{pmatrix}$

Table 2.4.: Comparison of reconstructed camera parameters with/without distortion

2.8.3. Accuracy of the Calibration

The complete calibration of the deflectometric setup was simulated to check the accuracy of the algorithm and evaluate the deviations.

The center of the camera is $\mathbf{r}_c = \begin{pmatrix} 0 \\ -200 \\ 120 \end{pmatrix} mm$, the vectors describing the local coordinate system of the sensor are $\mathbf{T}_x = \begin{pmatrix} 1 \\ 0 \\ 0 \end{pmatrix}$, $\mathbf{T}_y = \begin{pmatrix} 0 \\ 0.5145 \\ 0.8575 \end{pmatrix}$ and $\mathbf{N}_z = \begin{pmatrix} 0 \\ -0.8575 \\ 0.5145 \end{pmatrix}$. The image distance is $b = 28mm$ and the focal length $f = 25mm$. The number of pixels in the x-direction is 1360, in the y-direction 1024. The pixels are square shaped with a size of $4.65\mu m$.

The position of the pattern's center is $\mathbf{r}_c = \begin{pmatrix} 0 \\ 80 \\ 48 \end{pmatrix} mm$. The vectors defining the local coordinate system are $\mathbf{T}_x = \begin{pmatrix} 1 \\ 0 \\ 0 \end{pmatrix}$, $\mathbf{T}_y = \begin{pmatrix} 0 \\ -0.5145 \\ 0.8575 \end{pmatrix}$ and $\mathbf{N}_z = \begin{pmatrix} 0 \\ -0.8575 \\ -0.5145 \end{pmatrix}$.

The difference between the ideal parameters and the parameters kept by the calibration process are shown in Table 2.5 and Table 2.6.

Camera parameter	Deviation
$\Delta\mathbf{r}_c$	$\begin{pmatrix} 4.383 \cdot 10^{-3} \\ 3.979 \cdot 10^{-3} \\ -1.598 \cdot 10^{-2} \end{pmatrix} mm$
$\Delta\mathbf{T}_x$	$\begin{pmatrix} -1.704 \cdot 10^{-10} \\ 1.536 \cdot 10^{-5} \\ -1.024 \cdot 10^{-5} \end{pmatrix}$
$\Delta\mathbf{T}_y$	$\begin{pmatrix} 8.765 \cdot 10^{-7} \\ -4.664 \cdot 10^{-5} \\ 2.799 \cdot 10^{-5} \end{pmatrix}$
$\Delta\mathbf{N}_z$	$\begin{pmatrix} 1.844 \cdot 10^{-5} \\ -2.799 \cdot 10^{-5} \\ -4.665 \cdot 10^{-5} \end{pmatrix}$
Δb	$-9.653 \cdot 10^{-5} mm$

Table 2.5.: Deviation of the calibration data for the camera

Pattern parameter	Deviation
$\Delta\mathbf{r}_c$	$\begin{pmatrix} -1.639 \cdot 10^{-3} \\ 2.520 \cdot 10^{-2} \\ 7.904 \cdot 10^{-3} \end{pmatrix} mm$
$\Delta\mathbf{T}_x$	$\begin{pmatrix} -1.704 \cdot 10^{-10} \\ 1.536 \cdot 10^{-5} \\ 1.024 \cdot 10^{-5} \end{pmatrix}$
$\Delta\mathbf{T}_y$	$\begin{pmatrix} -8.688 \cdot 10^{-7} \\ -3.123 \cdot 10^{-4} \\ 1.875 \cdot 10^{-4} \end{pmatrix}$
$\Delta\mathbf{N}_z$	$\begin{pmatrix} 1.844 \cdot 10^{-5} \\ 1.875 \cdot 10^{-4} \\ -3.123 \cdot 10^{-4} \end{pmatrix}$

Table 2.6.: Deviation of the calibration data for the pattern

To reach an estimate of the accuracy of the calibration algorithm the marker center positions, which are calculated in the optimization's cost function, are compared to the

ones found in the images rendered with the original parameters.

When calibrating the substrate plane, the root-mean-square value of the deviation is $0.153\mu m$ and the peak-to-valley value $0.260\mu m$. As the simulated pixel size is $\Delta px = \Delta py = 4.65\mu m$ this corresponds to almost $\frac{1}{30}pixel$ for the root-mean-square value and almost $\frac{1}{18}pixel$ for the peak-to-valley value.

When calibrating the pattern, the root-mean-square value of the deviation is $0.364\mu m$ and the peak-to-valley value $3.307\mu m$. This corresponds to almost $\frac{1}{13}pixel$ for the root-mean-square value and almost $\frac{1}{2}pixel$ for the peak-to-valley value.

2.8.4. Influence on the Surface Reconstruction

A surface reconstruction with the results from the calibration of the deflectometric setup described in 2.8.3 is performed to evaluate the influence of the deviations of the calibration data compared to the ideal position and orientation values of all the elements in the setup. The parameters for the simulation are the same as in the simulation with the height distribution 2 in 1.10. But for the reconstruction the calibration data is used.

After 7 iterations of the start height loop, the height differences between the maxima in the frame regions is $0.08\mu m$. The maximum deviation from the original surface is $7.577\mu m$, the root-mean-square value of the difference is $4.578\mu m$. In the region of interest, which is the space between the frame regions, the maximum deviation is $0.697\mu m$ and the root-mean-square value of the difference is $0.097\mu m$.

Figure 2.12 depicts the absolute value of the difference between reconstructed and original surface for the reconstruction with ideal parameters and for the reconstruction with the parameters obtained by calibration. The comparison of the quality of both reconstructions is shown in Table 2.7.

	with ideal data	with calibration data
Maximum deviation (ROI)	$0.357\mu m$	$1.162\mu m$
root-mean-square value (ROI)	$0.091\mu m$	$0.414\mu m$

Table 2.7.: Comparison of the two reconstructions with respect to the maximum deviation and root-mean-square value

The reconstruction with setup parameters obtained through calibration provides a good agreement with the simulated surface as the root-mean-square value in the region of interest is still below $1\mu m$.

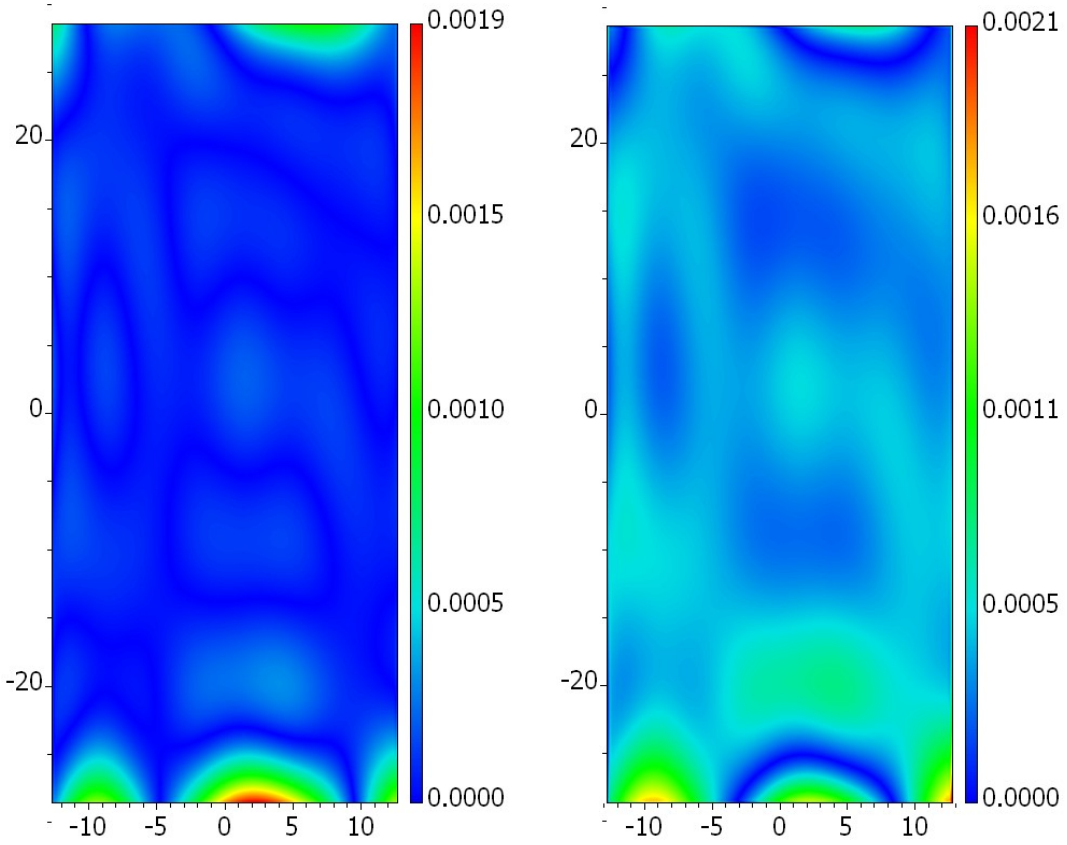

(a) Reconstruction with ideal data (b) Reconstruction with calibration data

Figure 2.12.: Absolute value of the difference between reconstructed and simulated surface (units are mm)

2.8.5. Distortion and Optical Axis

The camera center's position is $\mathbf{r}_c = \begin{pmatrix} 0 \\ -200 \\ 120 \end{pmatrix} mm$, the vectors of the sensor's coordinate system are $\mathbf{T}_x = \begin{pmatrix} 1 \\ 0 \\ 0 \end{pmatrix}$, $\mathbf{T}_y = \begin{pmatrix} 0 \\ 0.5145 \\ 0.8575 \end{pmatrix}$ and $\mathbf{N}_z = \begin{pmatrix} 0 \\ -0.8575 \\ 0.5145 \end{pmatrix}$. The coordinates of the interception point of the optical axis with the sensor plane is $\mathbf{r}_{cs} = \begin{pmatrix} 46.5 \\ 46.5 \end{pmatrix} \mu m$ (ten pixels in both directions) and the distortion coefficients are $c_0 = 1$ and $c_2 = 0.00123$.

The difference of the camera parameters obtained through calibration from the original parameters are listed in Table 2.8.

The marker centers calculated in the cost function of the optimization are compared to the correct marker centers. The root-mean-square value of the deviations is $3.844 \cdot 10^{-10} mm$ and the peak-to-valley value is $4.136 \cdot 10^{-10} mm$. When the optimization is

Camera parameter	Deviation
$\Delta\mathbf{r}_c$	$\begin{pmatrix} 2.62 \cdot 10^{-6} \\ 34.0 \\ 20.4 \end{pmatrix} \mu m$
$\Delta\mathbf{T}_x$	$\begin{pmatrix} 0 \\ 4.37 \cdot 10^{-10} \\ 2.53 \cdot 10^{-10} \end{pmatrix}$
$\Delta\mathbf{T}_y$	$\begin{pmatrix} 7.83 \cdot 10^{-12} \\ 2.43 \cdot 10^{-4} \\ 1.46 \cdot 10^{-4} \end{pmatrix}$
$\Delta\mathbf{N}_z$	$\begin{pmatrix} 5.05 \cdot 10^{-10} \\ 1.46 \cdot 10^{-4} \\ 2.43 \cdot 10^{-4} \end{pmatrix}$
$\Delta\mathbf{r}_{cs}$	$\begin{pmatrix} 0.02 \\ 7.94 \end{pmatrix} \mu m$
Δc_0	$2.47 \cdot 10^{-4}$
Δc_2	$9.11 \cdot 10^{-7}$

Table 2.8.: Deviations of the calibration data

carried out without taking the offset and the distortion into account, the root-mean-square value is $8.553 \cdot 10^{-4} mm$ and the peak-to-valley value is $1.542 \cdot 10^{-3} mm$.

The results show that the non-linear optimization provides applicable values for the camera parameters when there is a small offset between the sensor center and the optical axis and when slight geometrical distortions are present.

If the offset and distortion values are higher the optimized camera parameters become unrealistic. Particularly when calibrating the deflectometry setup the obtained values are not applicable. The optimized values for the offset strongly vary between the calibration of the substrate and the calibration of the pattern. The calibration of the experimental setup shows an offset of $\begin{pmatrix} -692.71 \\ 174.47 \end{pmatrix} \mu m$ for the substrate calibration and an offset of $\begin{pmatrix} -957.72 \\ 633.48 \end{pmatrix} \mu m$ for the pattern calibration. The distortion coefficients are $c_0 = 0.983$ and $c_2 = -0.00099$ for the substrate calibration and $c_0 = 0.998$ and $c_2 = 0.00050$ for the pattern calibration respectively. When the optimization is carried out by taking only the offset into account, completely different and unrealistic values for the offset are obtained. The offset for the substrate calibration then is $\begin{pmatrix} 980 \\ -1531 \end{pmatrix} \mu m$ and for the pattern calibration $\begin{pmatrix} -2492 \\ 10442 \end{pmatrix} \mu m$. When the camera parameters of both optimizations are used for surface reconstructions, the reconstructions fail. Thus the simulations and measurements are carried out without taking the offset and distortion into account.

2.9. Experimental Results

2.9.1. Accuracy of the Calibration

Dependency on the Camera Exposure

In order to analyze the dependency of the calibration on the camera exposure 15 images of the calibration pattern, which is shown in Figure 2.13(a), were taken. Each image is then used for a calibration. The number of markers is 6 in the x-direction and 4 in the y-direction respectively. The distance between the markers is $4mm$, the radius of the reference marker is $1.875mm$ and the radius of the other markers is $1.5mm$. Figure 2.13(b) shows the first camera image taken.

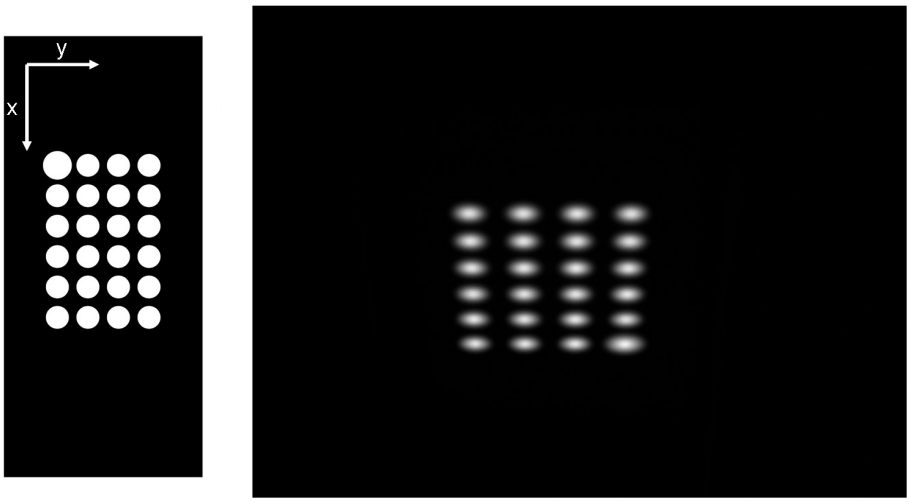

(a) Layout of the calibration pattern

(b) Camera image

Figure 2.13.: Dependency on the camera exposure

Figure 2.14 shows the deviation from the average value (Table 2.9) of the camera parameters $\mathbf{r}_c$, $\mathbf{r}_0$ and φ. The average values of the deviations of the camera parameters

Camera parameter	Average value
$\mathbf{r}_c$	$\begin{pmatrix} 194.567 \\ -0.140 \\ 112.961 \end{pmatrix} mm$
$\mathbf{r}_0$	$\begin{pmatrix} 4.498 \\ -2.225 \end{pmatrix} mm$
φ	$3.144rad$

Table 2.9.: Average value of the camera parameters $\mathbf{r}_c$, $\mathbf{r}_0$ and φ (15 images)

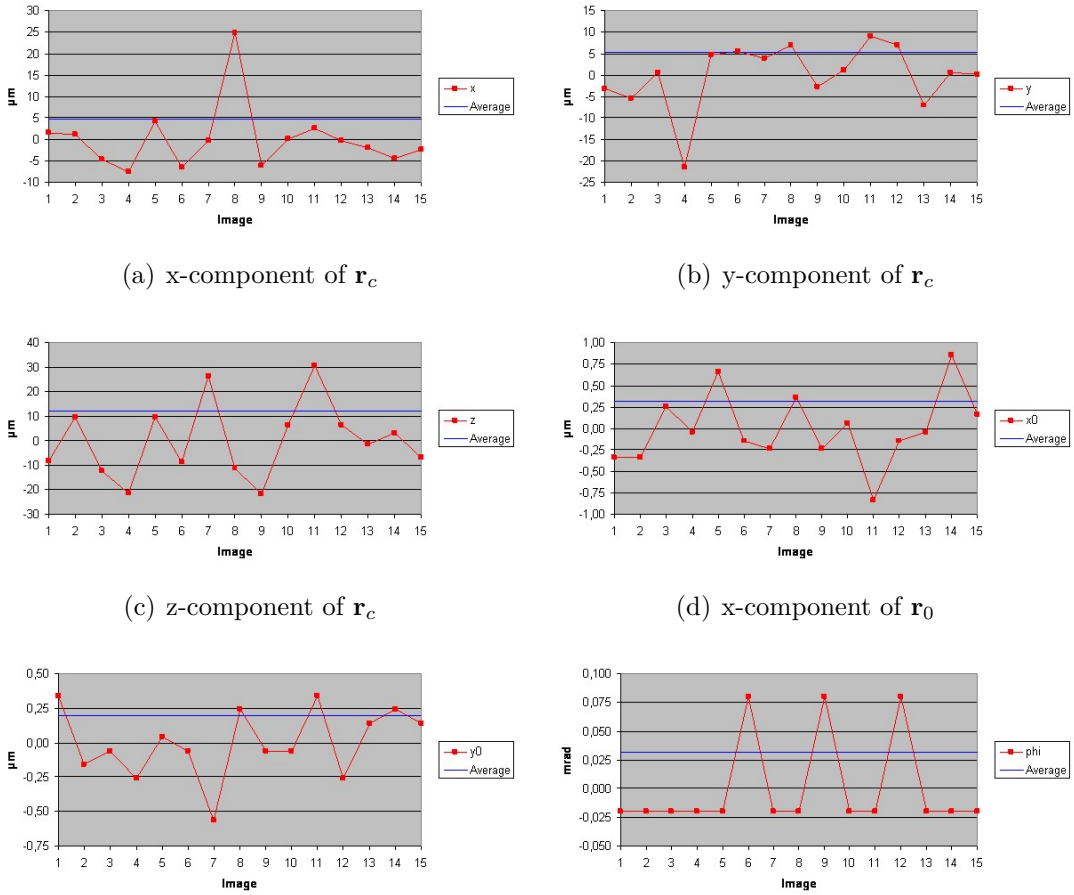

(a) x-component of $\mathbf{r}_c$

(b) y-component of $\mathbf{r}_c$

(c) z-component of $\mathbf{r}_c$

(d) x-component of $\mathbf{r}_0$

(e) y-component of $\mathbf{r}_0$

(f) φ

Figure 2.14.: Deviations from the average value of the camera parameters $\mathbf{r}_c$, $\mathbf{r}_0$ and φ

are listed in Table 2.10. The values for the camera center $\mathbf{r}_c$ are in the order of $10\mu m$, the values for $\mathbf{r}_0$ below $1\mu m$ and the average value of the deviation of the tilt angle φ is $0.032mrad$. Hence the repeatability of the camera calibration, when taking multiple camera images of the same scene, is precise enough.

Camera parameter	Average value of the deviation
$\mathbf{r}_c$	$\begin{pmatrix} 4.579 \\ 5.316 \\ 12.268 \end{pmatrix} \mu m$
$\mathbf{r}_0$	$\begin{pmatrix} 0.314 \\ 0.197 \end{pmatrix} \mu m$
φ	$3.2 \cdot 10^{-5} rad$

Table 2.10.: Average values of the deviations of camera parameters $\mathbf{r}_c$, $\mathbf{r}_0$ and φ (15 images)

Dependency on the Position of the Calibration Pattern

The accuracy of the camera parameters $\mathbf{r}_c$, $\mathbf{r}_0$ and φ was surveyed on the basis of two calibration patterns on one substrate with one common coordinate system. The lithographic process for the patterns has an accuracy below $1\mu m$, hence the offset of the two patterns is very accurate. Therefore this known offset can be used for a verification of the calibration.

The patterns have identical features. The number of markers is 4 in both directions. The distance between the markers is $3mm$, the radius of the reference marker is $750\mu m$ and the radius of the other markers is $500\mu m$. The offset in the x-direction is $14mm$ and in the y-direction $11mm$ (Figure 2.15).

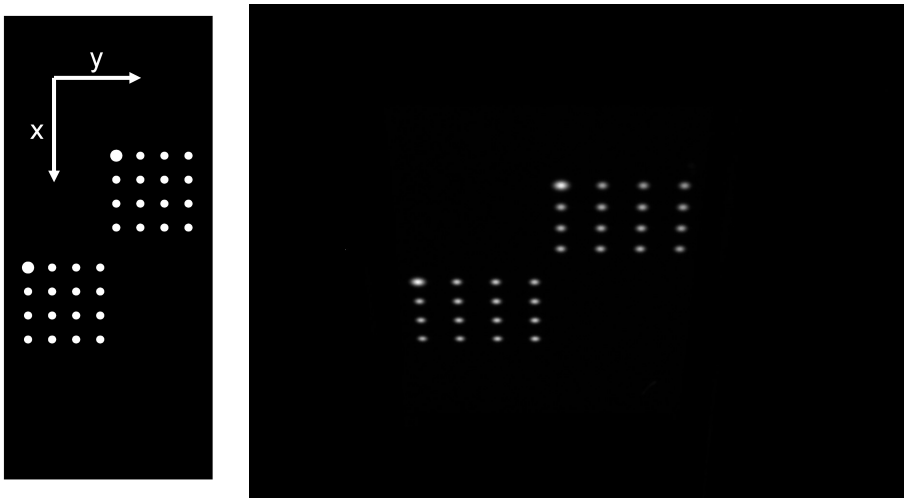

(a) Layout of the two calibration patterns

(b) Camera image

Figure 2.15.: Dependency on the position of the calibration pattern

The center of the common coordinate system is defined to be exactly between both calibration patterns. Thus the calibration results of both patterns should ideally be the same. Table 2.11 shows the camera parameters for both calibrations and their difference. The largest difference of the camera center $\mathbf{r}_c$ is in the order of $500\mu m$, the difference of the point $\mathbf{r}_0$ where the optical axis cuts the pattern plane is in the order of $10\mu m$ and the difference of the tilt angle φ is below $1mrad$ when an offset of 2π is taken into account. Considering that the distance of the camera is about $22cm$ in the setup these values are satisfying.

Detection of a Pattern Shift

To analyze the accuracy in detecting a pattern shift the same camera image as in the analysis of the dependency on the position of the calibration pattern was used instead

Camera parameter	Upper pattern	Lower pattern	Difference
$\mathbf{r}_c$	$\begin{pmatrix}-191.931\\0.315\\113.092\end{pmatrix} mm$	$\begin{pmatrix}-192.414\\0.459\\113.284\end{pmatrix} mm$	$\begin{pmatrix}482.4\\-144.0\\-191.6\end{pmatrix} \mu m$
$\mathbf{r}_0$	$\begin{pmatrix}-2.189\\2.189\end{pmatrix} mm$	$\begin{pmatrix}-2.197\\2.200\end{pmatrix} mm$	$\begin{pmatrix}8.3\\-10.8\end{pmatrix} \mu m$
φ	$-3.138 rad$	$3.145 rad$	$0.285 mrad$

Table 2.11.: Camera parameters for two calibration patterns in the same coordinate system

of moving a pattern and acquire two camera images. Now both calibration patterns define their own coordinate system. The respective point of origin is located at the center of each pattern. As the experimental setup for both calibrations is the same the point where the optical axis cuts the pattern plane $\mathbf{r}_0$ is used to detect the lateral shift. For the offset in the x-direction dx and the offset in the y-direction dy follows from geometrical considerations:

$$\begin{aligned} dx &= x_{0,upper} - x_{0,lower} \\ dy &= y_{0,lower} - y_{0,upper} \end{aligned}$$

with $\begin{pmatrix}x_{0,upper}\\y_{0,upper}\end{pmatrix} = \mathbf{r}_{0,upper}$ being the penetration point in coordinates of the upper pattern and $\begin{pmatrix}x_{0,lower}\\y_{0,lower}\end{pmatrix} = \mathbf{r}_{0,lower}$ being the penetration point in coordinates of the lower pattern.

The camera parameters obtained from both patterns are listed in Table 2.12. The

Camera parameter	Upper pattern	Lower pattern
$\mathbf{r}_c$	$\begin{pmatrix}-184.931\\-5.185\\113.092\end{pmatrix} mm$	$\begin{pmatrix}-199.414\\5.959\\113.284\end{pmatrix} mm$
$\mathbf{r}_0$	$\begin{pmatrix}4.8109\\-3.3106\end{pmatrix} mm$	$\begin{pmatrix}-9.1947\\7.7002\end{pmatrix} mm$
φ	$-3.138 rad$	$3.145 rad$

Table 2.12.: Camera parameters for both calibration patterns

detected offsets in the x-direction and in the y-direction respectively are:

$$\begin{aligned} dx &= 4.8109\mu m - (-9.1947\mu m) = 14.0056\mu m \\ dy &= 7.7002\mu m - (-3.3106\mu m) = 11.0108\mu m \end{aligned}$$

With the known offsets $dx_{pattern} = 14mm$ and $dy_{pattern} = 11mm$ of the lithographically fabricated patterns the deviation of the offset in the x-direction is $5.6\mu m$ and $10.8\mu m$ in the y-direction. This corresponds to an error of 0.04% for the x-offset and 0.10% for the y-offset.

2.9.2. Calibration of the Deflectometry Setup

The calibration results which are presented here are the ones used for the deflectometric measurement in 1.12. Figure 2.16 shows the camera image for the calibration of the substrate plane and Table 2.13 the corresponding camera parameters. The camera image for the pattern calibration is found in Figure 2.17 and the corresponding pattern parameters are listed in Table 2.14 for the virtual pattern and in Table 2.15 for the real pattern.

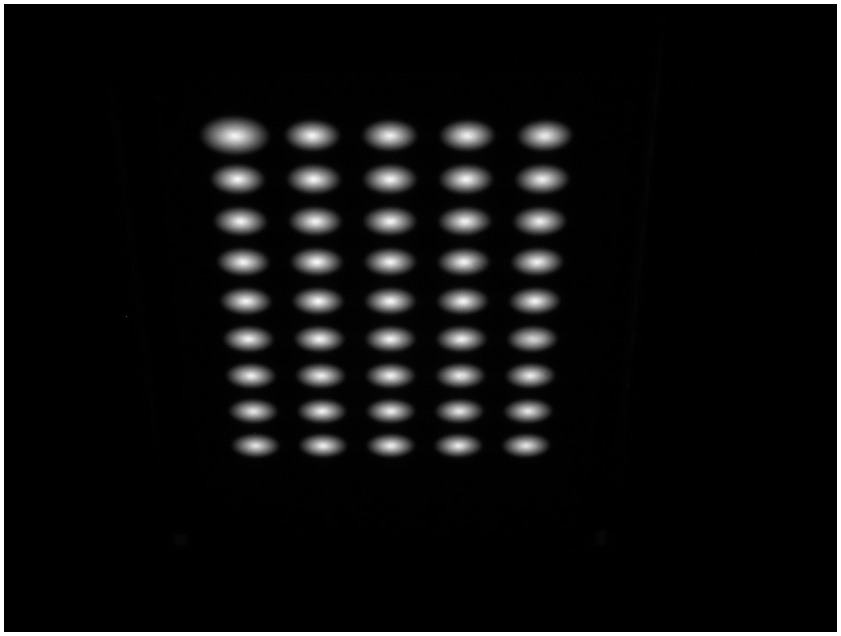

Figure 2.16.: Camera image of the substrate calibration (experiment)

Camera parameter	Calibration result
$\mathbf{r}_c$	$\begin{pmatrix} -0.359 \\ -175.235 \\ 110.394 \end{pmatrix} mm$
$\mathbf{T}_x$	$\begin{pmatrix} -0.999 \\ -5.172 \cdot 10^{-3} \\ 3.613 \cdot 10^{-3} \end{pmatrix}$
$\mathbf{T}_y$	$\begin{pmatrix} 3.291 \cdot 10^{-4} \\ -0.529 \\ -0.849 \end{pmatrix}$
$\mathbf{N}_z$	$\begin{pmatrix} 6.300 \cdot 10^{-3} \\ -0.848 \\ 0.529 \end{pmatrix}$
b	$28.404mm$

Table 2.13.: Results of the substrate calibration

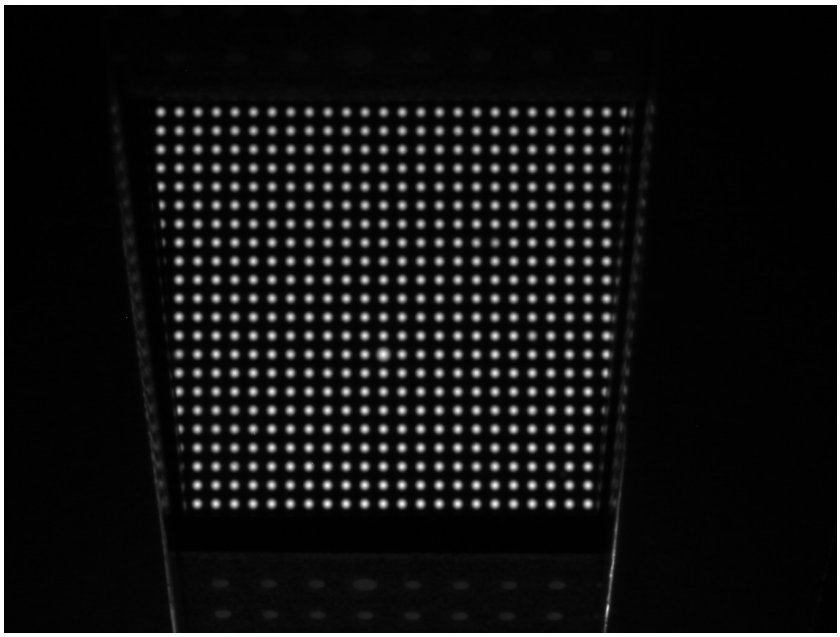

Figure 2.17.: Camera image of the pattern calibration (experiment)

Camera parameter	Calibration result
$\mathbf{r}_c$	$\begin{pmatrix} 2.294 \\ 7.799 \\ 290.638 \end{pmatrix} mm$
$\mathbf{T}_x$	$\begin{pmatrix} 0.999 \\ -2.596 \cdot 10^{-5} \\ 2.230 \cdot 10^{-3} \end{pmatrix}$
$\mathbf{T}_y$	$\begin{pmatrix} 6.359 \cdot 10^{-5} \\ 0.999 \\ -1.687 \cdot 10^{-2} \end{pmatrix}$
$\mathbf{N}_z$	$\begin{pmatrix} -2.229 \cdot 10^{-3} \\ 1.687 \cdot 10^{-2} \\ 0.999 \end{pmatrix}$
b	$27.352mm$

Table 2.14.: Calibration results for the virtual pattern (camera's relative position)

Pattern parameter	Calibration result
$\mathbf{r}_c$	$\begin{pmatrix} 0.752 \\ 72.986 \\ 41.004 \end{pmatrix} mm$
$\mathbf{T}_x$	$\begin{pmatrix} -0.999 \\ -3.314 \cdot 10^{-3} \\ 2.380 \cdot 10^{-3} \end{pmatrix}$
$\mathbf{T}_y$	$\begin{pmatrix} 1.968 \cdot 10^{-4} \\ 0.543 \\ -0.839 \end{pmatrix}$
$\mathbf{N}_z$	$\begin{pmatrix} 4.075 \cdot 10^{-3} \\ -0.839 \\ -0.543 \end{pmatrix}$

Table 2.15.: Calibration results for the real pattern in the global coordinate system

2.10. Summary

The camera calibration, which is introduced here, only needs one image of a known pattern to calculate the camera parameters. It is based on the geometric properties of the camera and is performed in two steps. First the camera parameters are calculated with a linear approximation. Then the values are refined using a non-linear optimization.

The calibration of the deflectometry setup is accomplished in three steps. First the camera parameters relative to the substrate plane are obtained. In the second step the parameters of the deflectometry pattern are measured by using a mirror at the substrate plane. In the last step the values from the preceding steps are combined in the global coordinate system.

The simulations of the accuracy show that the markers are found with a precision of at least $\frac{1}{20}$ pixel. This precision leads to an error in the camera position of less than $10\mu m$. The analysis of the influence of the deviations on the surface reconstruction in the deflectometry setup shows that the surface is still reconstructed with an root-mean-square value of the height deviation below $1\mu m$ in the region of interest.

When taking multiple camera images of the same scene in the experimental setup the repeatability is precise enough as the average values of the deviations are approximately $10\mu m$ for $\mathbf{r}_c$, less than $1\mu m$ for $\mathbf{r}_0$ and significantly smaller than $1mrad$ for the tilt angle φ.

The analysis of the accuracy in the experiment shows an error in the detection of a pattern shift of 0.04% in the x-direction and 0.10% in the y-direction respectively. This corresponds to an absolute error in the order of $10\mu m$ for both directions. The comarison of the camera parameters obtained through calibrations with two patterns in a common coordinate system shows a difference in the order of $500\mu m$ for the camera center $\mathbf{r}_c$, a difference in the order of $10\mu m$ for the point where the optical axis cuts the pattern plane $\mathbf{r}_0$ and a difference below $1mrad$ for the tilt angle φ. Considering that the distance of the camera is about $22cm$ in the setup these values are satisfying. One possible reason for these errors is that the sensor offset and the image distortion could not be covered satisfactorily by the optimization.

Part II.

Compact Multi-Channel Fluorescence Microscope

3. Concept

3.1. Introduction

The acceleration of the image acquisition in fluorescence microscopy can be achieved by parallelizing the observation of the single experiments of a genome-wide screen. Here the concept and the implementation of a compact multi-spectral microscope unit is presented which is able to acquire images of four fluorophores in parallel in one field of view without moving any components. As optic designers have put a lot of effort in optimizing objective lenses for fluorescence microscopy in the past decades, the design is based on commercially available objectives in order to obtain high spatial resolution. The concept was developed and first implementations were made by Lars Lehmann and Prof. Dr. Peter Fischer from the Chair of Circuit Design at the University of Heidelberg. The work presented here is the continuation of their last implementation.

3.2. Fluorescence of Organic Molecules

The information in this section originates from [Wolf 2007]. Single atoms have discrete energy levels, so called states. In contrast, an organic molecule has broadened energy levels, resulting from the various vibrational states the molecule can exist in.

If an organic molecule in the ground state is excited by the absorption of light, it can occupy, for example, the first singlet excited state. It then decays to the lowest level of this excited state without emitting radiation. After a short time it relaxes to one of the vibrational levels of the ground state and emits radiation. Finally, it non radiatively returns to the lowest vibrational level of the ground state.

The vibrational levels result in a broadened excitation and emission spectrum. The energy of the emission is lower compared to the excitation. Thus, the emission light has a longer wavelength than the excitation light. This phenomenon is known as the Stoke's shift.

3.3. Used Fluorophores

3.3.1. Blue Channel

DAPI

The fluorophore DAPI binds to the nucleus of a cell. It attaches strongly to adenine-thymine rich sequences of the DNA and thereby forms a fluorescent complex [Kapuscinski 1995]. When bound to the double-stranded DNA the excitation peak is at $358nm$, its emission maximum is $461nm$ [Invitrogen 2006] and the quantum yield is 0.92 [Kapuscinski 1995]. The excitation and emission spectra are shown in Figure 3.1.

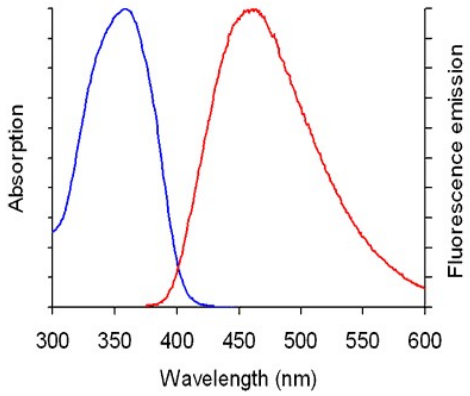

Figure 3.1.: Excitation and emission spectra of DAPI (image source: Life Technologies Corporation)

Hoechst 33258

Hoechst 33258 also binds to the nucleus of a cell. It is often used as a substitute for DAPI. The excitation maximum is $350nm$, the emission peak is at near $460nm$ and the quantum yield is 0.6 [Latt et al. 1975]. Figure 3.2 depicts the excitation and emission spectra.

3.3.2. Green Channel

GFP

The green fluorescent protein is one of the most popular fluorophores. The GFP gene can combine with other proteins, thus tagging them fluorescently. It can be expressed

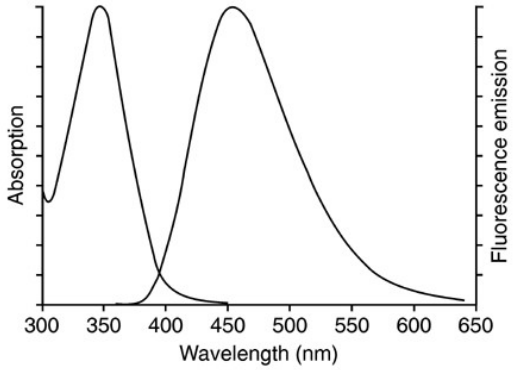

Figure 3.2.: Excitation and emission spectra of Hoechst 33258 (image source: Life Technologies Corporation)

in every species, in which genetic engineering is possible [Yuste 2005]. The excitation maximum of EGFP, which is an optimized derivate of GFP, is $488nm$, the emission peak is at $507nm$ and features a quantum yield of 0.6 [Day et al. 2009]. The spectra are found in Figure 3.3.

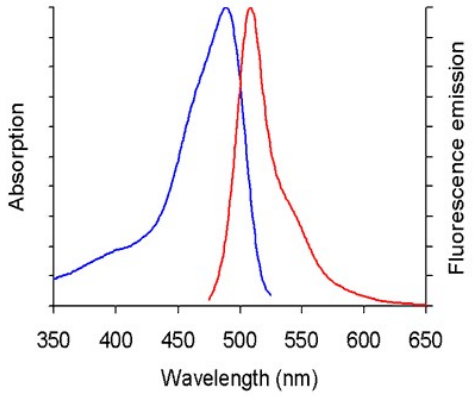

Figure 3.3.: Excitation and emission spectra of EGFP (image source: Life Technologies Corporation)

3.3.3. Red Channel

mRFP and mCherry

The red fluorescence protein mRFP provides an alternative to GFP concerning the fluorescent labeling of fusion proteins [Campbell et al. 2002]. The excitation peak is at

584nm, its emission maximum is 607nm and the quantum yield is 0.25 [Campbell et al. 2002]. The excitation and emission spectra are depicted in Figure 3.4.

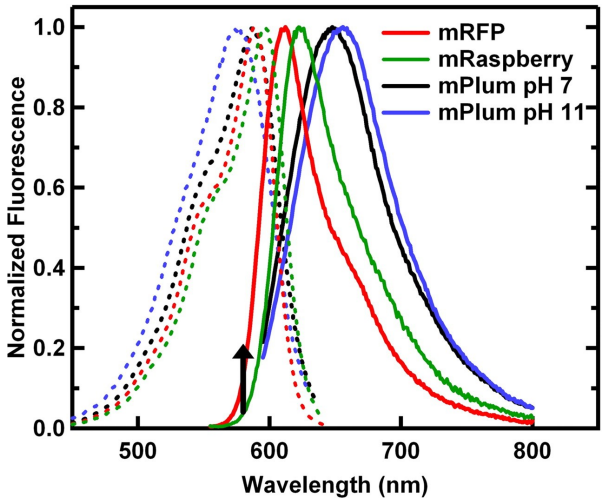

Figure 3.4.: Excitation and emission spectra of mRFP (image source: [Abbyad et al. 2007])

Fluorophore mCherry is an optimized version of mRFP. The excitation maximum is 587nm and the emission peak is at 610nm. It features a quantum yield of 0.22 [Shaner et al. 2004].

3.3.4. NIR Channel

DRAQ5

Fluorophore DRAQ5 rapidly stains fixed or living cells and has a high affinity to DNA [Smith et al. 1999]. The excitation peak is at 646nm and the emission maximum is 681nm respectively 697nm when intercalated with double-stranded DNA [Biostatus Limited 2012]. The quantum yield is 0.003 to 0.004 [Njoh et al. 2006]. Figure 3.5 shows the excitation and emission spectra for this fluorophore.

3.4. Parallelization

3.4.1. Spectral Domain

In many biological experiments it is essential to mark different structures of one cell with different fluorophores. In off-the-shelf automated wide-field microscopes white light

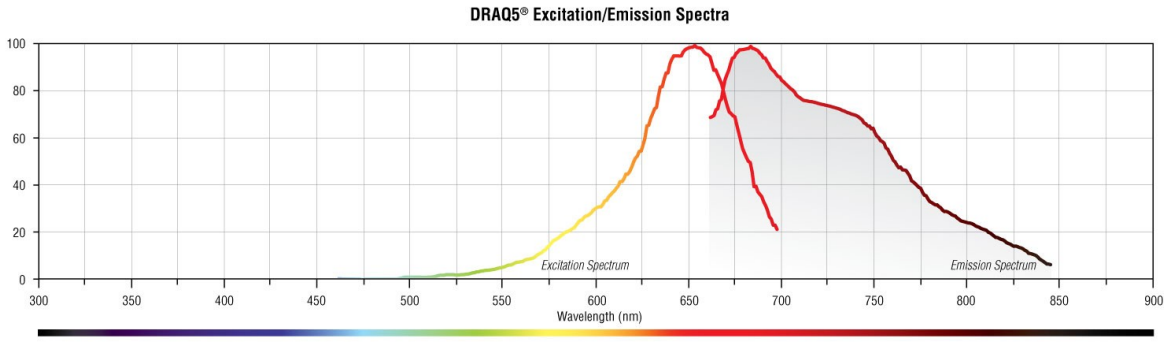

Figure 3.5.: Excitation and emission spectra of DRAQ5 (image source: Cell Signaling Technology Inc.)

sources in conjunction with filter wheels are used to change the spectral band for the illumination and the image acquisition to select one specific fluorophore. As the filter change is a mechanical movement it is time-consuming. In the concept presented here, however, narrow band light sources and beam splitters / filters are used to combine the excitation light and to separate the emitted light coming from the observed object.

Channel	Excitation	Emission	Fluorophore
Blue	$360 \pm 20nm$	$455 \pm 25nm$	DAPI/Hoechst 33258
Green	$485 \pm 8nm$	$525 \pm 25nm$	EGFP
Red	$570 \pm 10nm$	$620 \pm 30nm$	mRFP/mCherry
NIR	$680 \pm 20nm$	$785 \pm 15nm$	DRAQ5

Table 3.1.: Excitation and emission bands of the four channels

One compact microscope unit (CMU) is designed to feature four excitation channels and four emission channels (Table 3.1) which all pass through one objective lens. The wavelength ranges for the excitation and emission bands arise from the available beam splitters and bandpass filters. In order to ensure that the beam splitters function properly, the passing light has to be collimated. Hence an infinity-corrected objective lens is used together with a corresponding tubus lens in each emission channel.

Apart from the aspect of time saving by avoiding mechanical movements, the images of the four channels are taken at the exact same point in time, which is relevant when observing living cells.

3.4.2. Spatial Domain

Multiple multi-channel microscope units can be combined in one microscope system to observe different lateral positions on the substrate. Therefore the thickness of one unit is

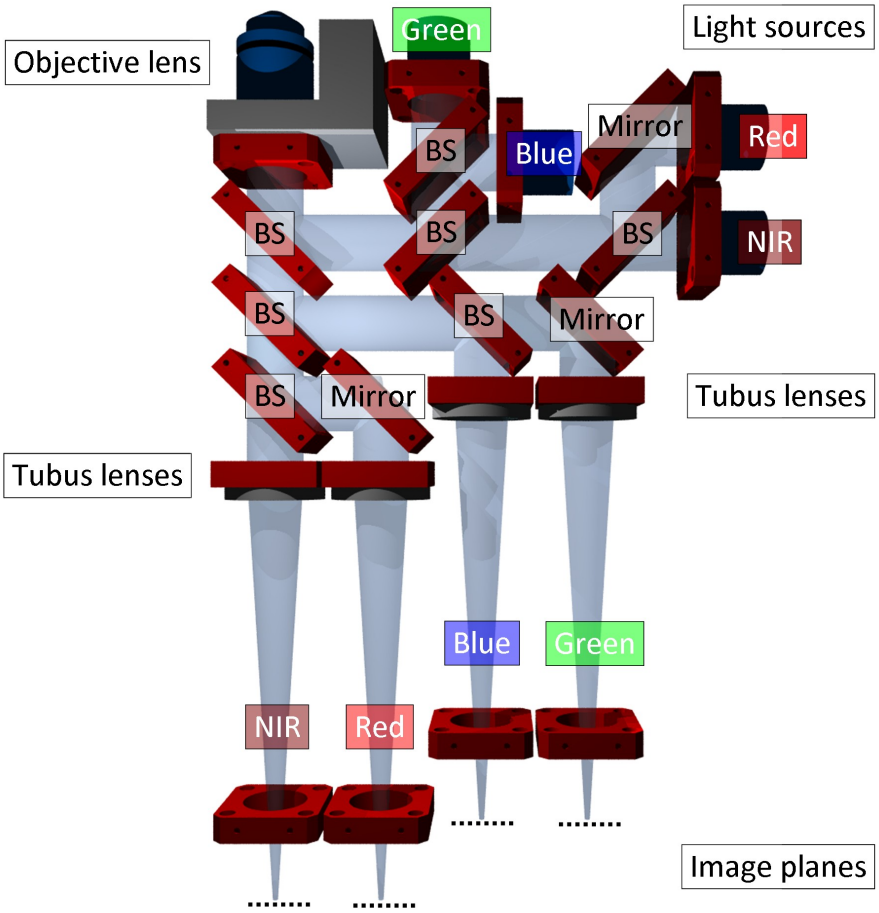

Figure 3.6.: Conceptual design of one CMU

designed to be as small as possible taking into account the size of the used components.

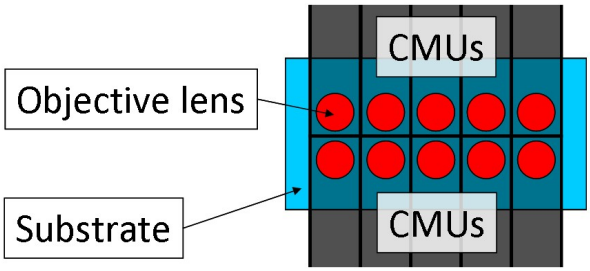

Figure 3.7.: Multiple compact microscope units (CMUs)

4. Implementation

The complete experimental setup of the microscope is depicted in Figure 4.1(a). Figure 4.1(b) shows the implementation of the compact microscope unit.

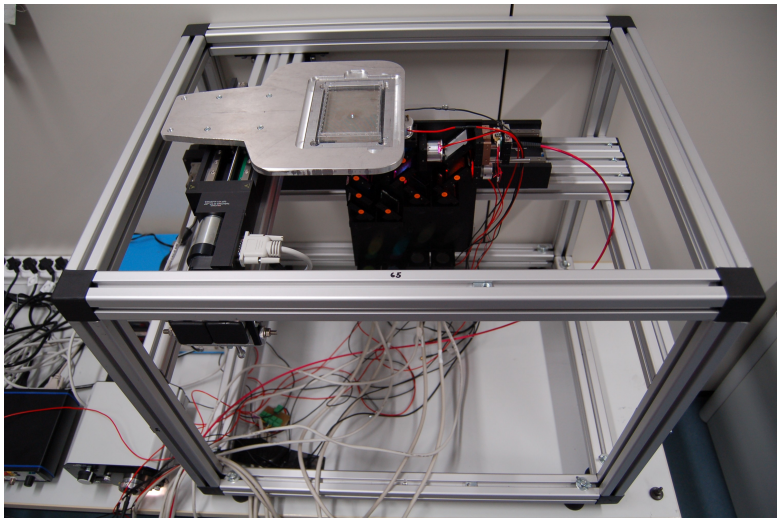

(a) Microscope setup

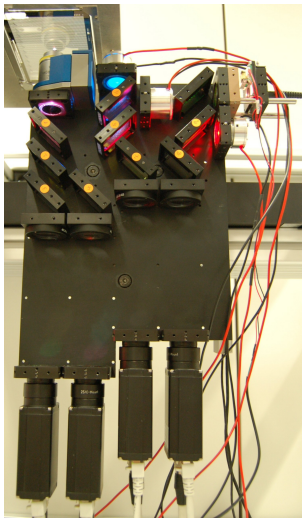

(b) Compact microscope unit

Figure 4.1.: Implementation of the microscope

4.1. Microscope Unit

4.1.1. Light Sources

Blue Channel For this channel a high power UV-LED from Nichia (NCSU033B) was chosen. It features a peak wavelength between $360nm$ and $370nm$ and a spectrum half width of $9nm$, so that no additional bandpass filter is needed as the spectrum lies completely within the usable band of $340nm$ to $380nm$(Table 3.1) except for some minor parts beyond $380nm$. In Figure 4.2 the measured spectrum is shown. The usable wavelength range is located between the vertical red lines.

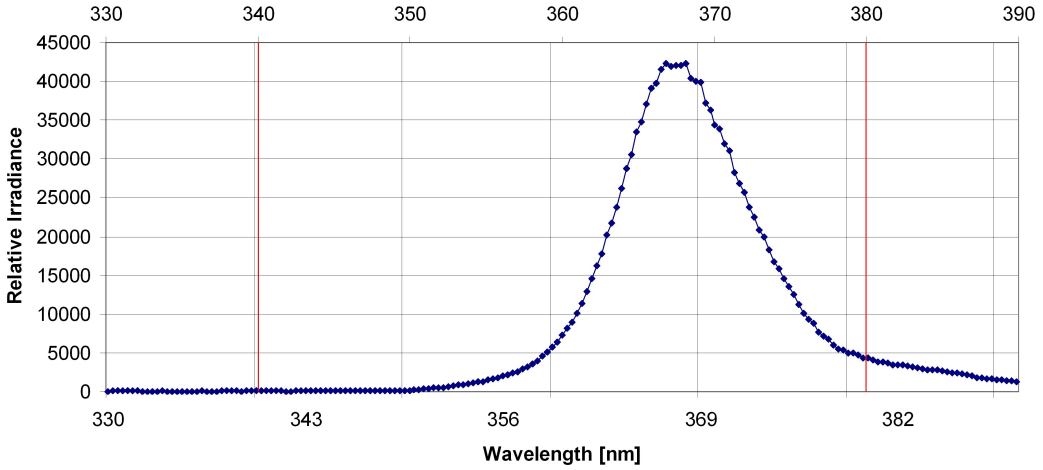

Figure 4.2.: Measured spectrum of the UV-LED

Green Channel The best fitting high power LED for the excitation in the green channel is the Rebel Blue from the company Luxeon. It has a peak wavelength between $475nm$ and $480nm$ and a spectrum half width of $20nm$. As the usable band for this channel is $477nm$ to $493nm$ a bandpass filter is needed to crop the unwanted frequency components. The bandpass used features a range of $476.5nm$ up to $492.5nm$. The measured spectrum of the light source is found in Figure 4.3.

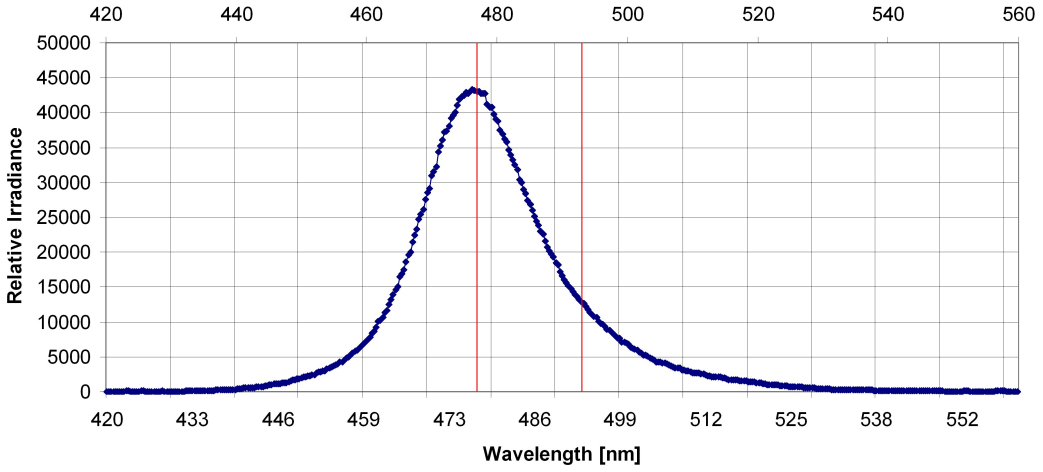

Figure 4.3.: Measured spectrum of the Rebel Blue LED

Red Channel There is no high power LED available for the usable spectrum of $560nm$ up to $580nm$ and the suitable lasers are very expensive. For this reason a $150W$ halogen bulb coupled into a fiber, which features a numerical aperture of 0.39 and a core diameter of $1mm$, in combination with a bandpass filter with a range of $560nm$ up to $580nm$ is

used. The halogen bulb needs time to have full optical output power after switching it on and afterglows when switched off. Therefore a mechanical shutter is used to trigger the light source. In Figure 4.4 the measured spectrum is depicted.

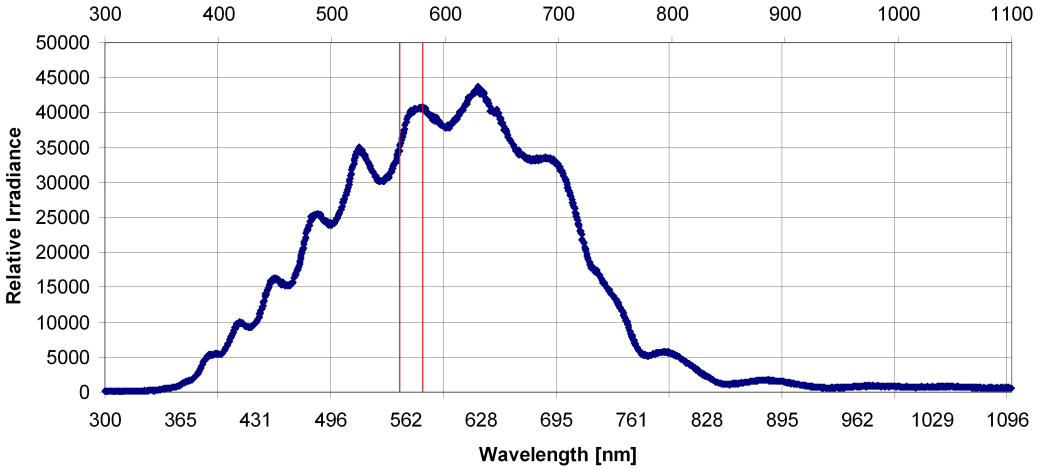

Figure 4.4.: Measured spectrum of the halogen source coupled into the fiber

NIR Channel For the excitation of the near-infrared channel a high power LED Rebel Deep Red from Luxeon is used. The peak wavelength is 662.5nm and the spectrum half width is 20nm. With a bandpass filter with a range of 660nm to 700nm the usable spectrum is reached. In Figure 4.5 the measured spectrum is shown.

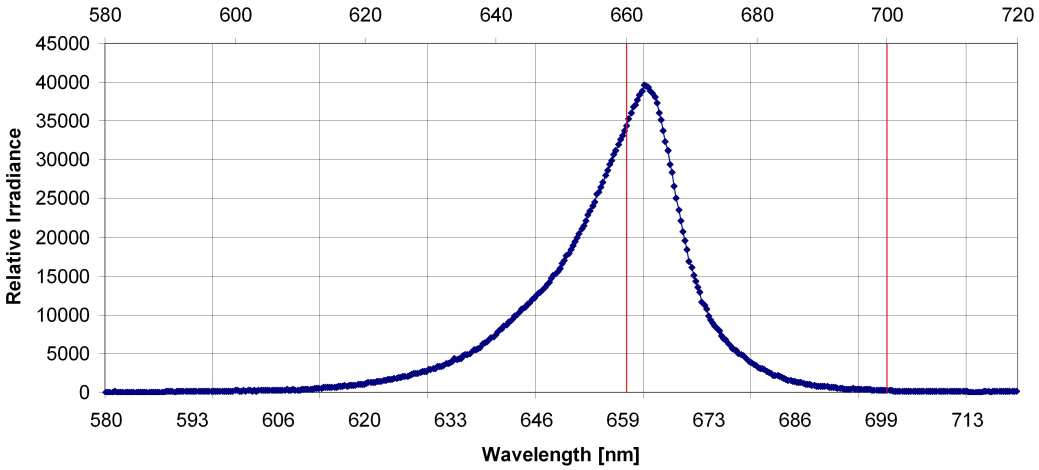

Figure 4.5.: Measured spectrum of the Rebel Deep Red LED

Collimation

To ensure that the beam splitters and filters work properly, the light sources must be collimated. But the collimation must not be perfect as the illuminated area at the object space has to be at least as big as the observed area. Due to the fact that the LEDs are extended sources and the fiber used at the green channel has a core diameter of $1mm$, which hence can not be seen as a point light source either, the collimation will not be perfect. This results in an illuminated area on the object plane, which is bigger than the observed area.

LEDs The LEDs are collimated by using aspheric lenses from the company OptoSigma. The lenses have a convex surface on the source side and an aspheric surface on the other side. They feature a focal length of $12mm$ and a diameter of $18mm$. Figure 4.6 shows the LED housing with integrated collimation lens and bandpass filter.

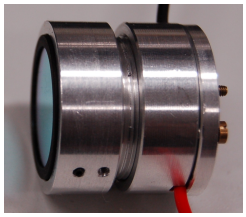

Figure 4.6.: LED housing with collimation lens and bandpass filter

Fiber Coupled Halogen Bulb The collimation of the light from the halogen bulb is achieved with an aspherical Linos Microbench lens with a focal length of $25mm$ and a diameter of $30mm$. The fiber-mount with the shutter, collimation lens and bandpass filter is shown in Figure 4.7.

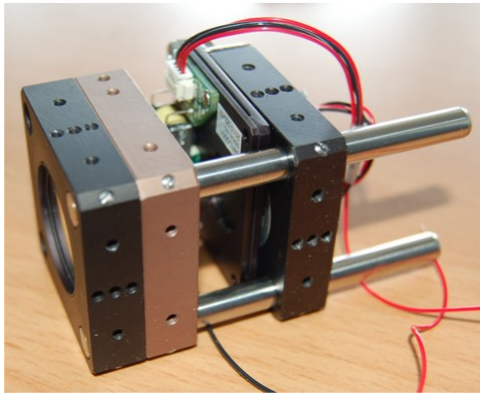

Figure 4.7.: Fiber-mount for halogen light source with shutter, collimation lens and bandpass filter

Optical Power and Illuminated Area at the Object Plane

The optical power of the excitation is measured after all spectral portions of each light source that are not wanted for the excitation are filtered out. A power meter was positioned above the objective lens in the object plane. The light sources were driven at the maximum ratings for the current. The optical power and the illuminated area for each channel are listed in Table 4.1. The lowest optical power of $0.85mW$ is found at the red channel, which uses a $150W$ halogen bulb coupled into a fiber. There is a high loss of power, because the coupling is not very efficient. The illuminated areas fulfill the requirements as the area observed by the cameras is $897.4\mu m$ in the horizontal direction and $670.8\mu m$ in the vertical direction if a magnification of 10 is assumed.

Channel	Optical power	Illuminated area
$Blue$	$9.13mW$	$0.9mm$
$Green$	$1.42mW$	$0.9mm$
Red	$0.85mW$	$1.1mm$
NIR	$7.78mW$	$0.9mm$

Table 4.1.: Optical power and illuminated area of the excitation light at the object plane

Spectra at the Object Plane

To ensure that only the wavelength range which is needed for the excitation of each channel is guided to the object plane the spectrum for each channel is measured after the light has passed the objective lens.

Blue The spectrum of the UV-LED at the object plane lies completely within the needed wavelength range (Figure 4.8).

Green The spectrum of the Rebel Blue LED does not show the desired wavelength range (Figure 4.9). The analysis of the bandpass filter leads to the conclusion that it does not fit its specification. The coating on the filter is not homogeneous. A radial gradient is observed, when inspecting it with the eyes. A second filter of the same type shows the same defects. Nevertheless the main peak is still in the desired wavelength range. And the portions outside do not lead to crosstalk to the other channels, neither at the excitation nor the emission.

Red As the light source for this channel is a halogen bulb, a lot of unwanted wavelengths have to be filtered out. As can be seen in Figure 4.10, the spectrum fits well into the desired range.

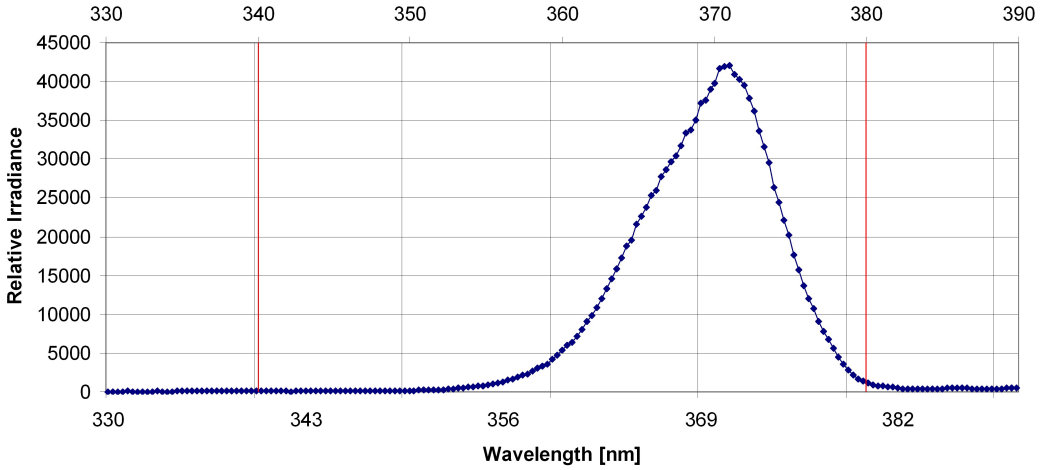

Figure 4.8.: Measured spectrum of the UV-LED at the object plane

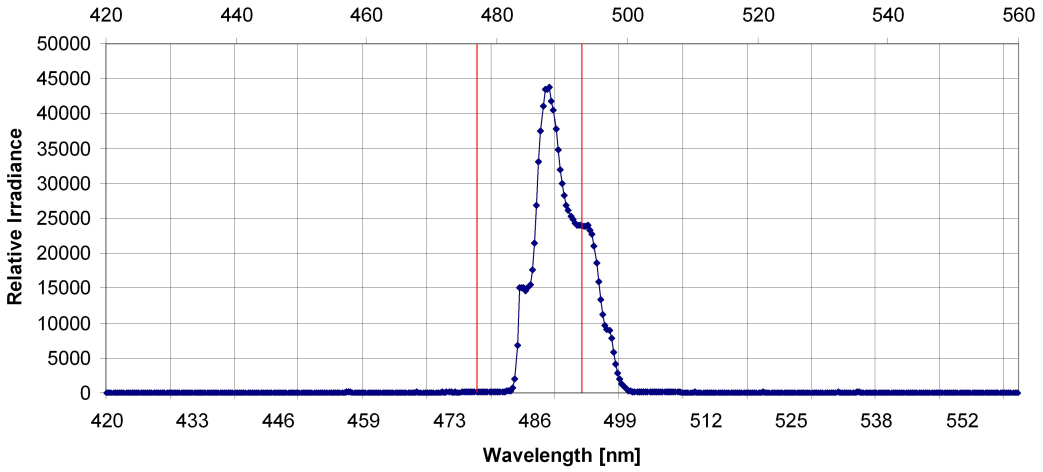

Figure 4.9.: Measured spectrum of the Rebel Blue LED at the object plane

NIR The main part of the spectrum of the Rebel Deep Red LED lies between the lower and upper limit for this channel. The spectrum is shown in Figure 4.11.

4.1.2. Imaging Components

The imaging system consists of an infinity-corrected objective lens and four corresponding tubus lenses – one for each emission channel – from the company Zeiss. The objective lens functions with a magnification of 10, a numerical aperture of 0.45 and a working distance of $2mm$. It is optimized to work with a cover glass thickness of $170\mu m$. The focal length of the tubus lens is $164.5mm$.

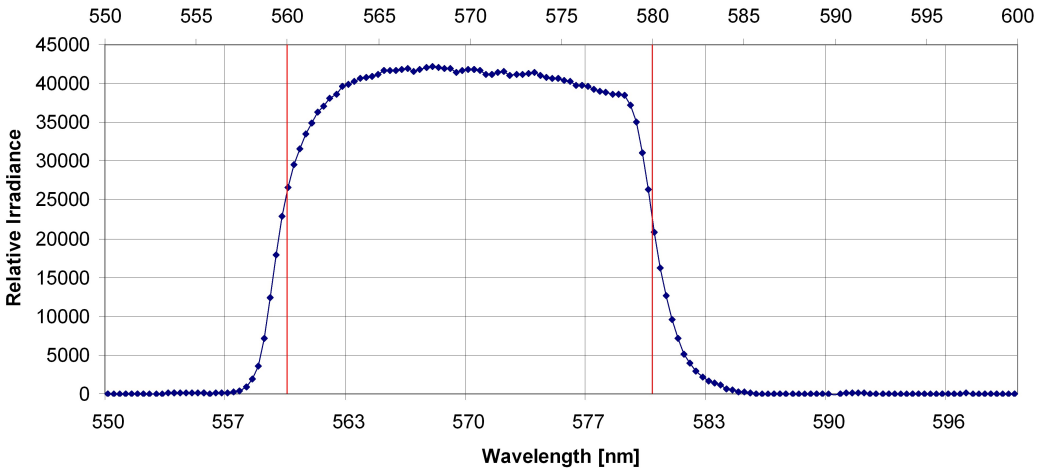

Figure 4.10.: Measured spectrum of the halogen source at the object plane

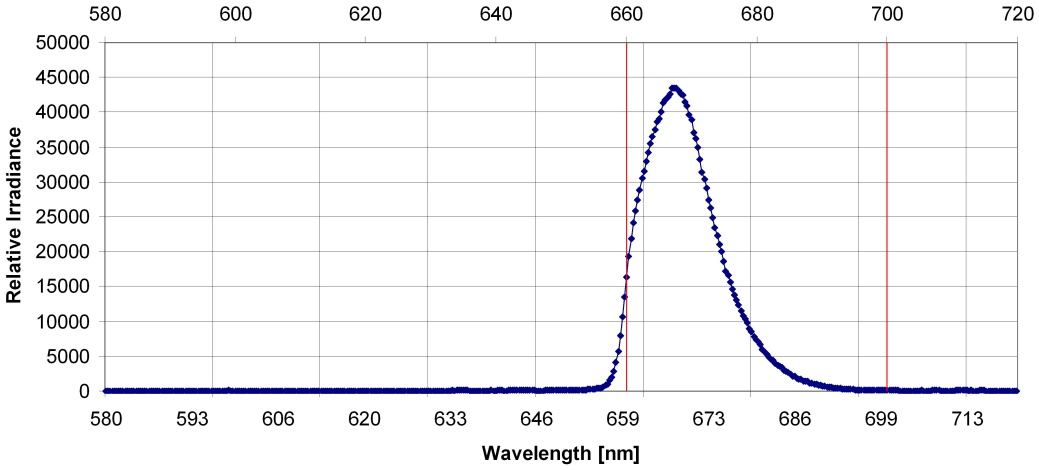

Figure 4.11.: Measured spectrum of the Rebel Deep Red LED at the object plane

4.1.3. Components for Spectral Selection

The beam splitters and bandpass filters are manufactured by the company Chroma Technology. The beam splitters feature a width of $25.5mm$, a height of $36mm$ and a thickness of $1mm$. The free aperture diameter of the bandpass filters is $22mm$.

The <number>DCXR beam splitters are dichroic high-pass filters with respect to the wavelength when they are used in transmission. When used in reflection they act as low-pass filters. The beam splitter denominated with 61002BS, which is located directly behind the objective lens, is a multi-bandpass filter. The filter curve, when it is used in transmission, is depicted in Figure 4.12. When used in reflection the shown filter curve is inverted. It is the component which merges the illumination path with the imaging path. This beam splitter defines the usable excitation and emission bands.

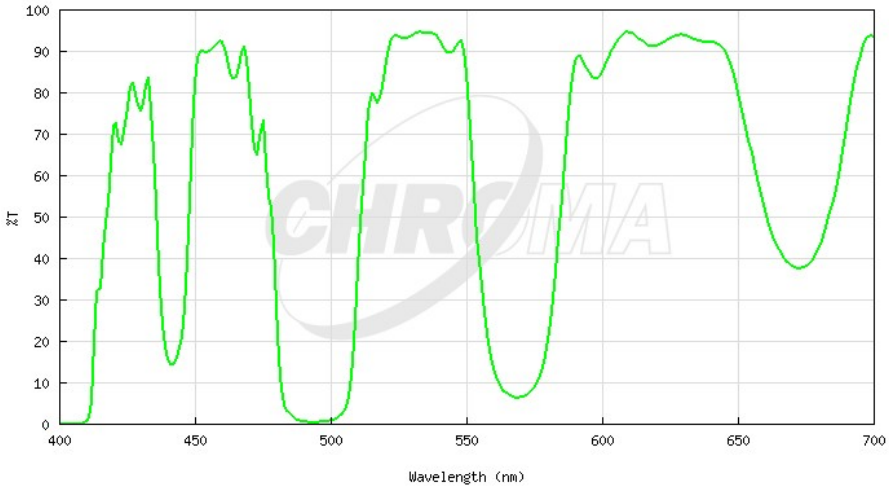

Figure 4.12.: Spectrum of the 61002BS beam splitter when used in transmission (image source: Chroma Technology Corporation)

Filters and Beam Splitter in the Excitation Paths

The filters and beam splitters are listed in the order related to their position in the optical path starting from the source.

Blue Channel

- Bandpass filter HQ360/40M
- Beam splitter 425DCXR (reflection)
- Beam splitter 515DCXR (reflection)
- Beam splitter 61002BS (reflection)

Green Channel

- Bandpass filter HQ485/15X
- Beam splitter 425DCXR (transmission)
- Beam splitter 515DCXR (reflection)
- Beam splitter 61002BS (reflection)

Red Channel

- Bandpass filter HQ570/20X
- Beam splitter 585DCXR (reflection)
- Beam splitter 515DCXR (transmission)
- Beam splitter 61002BS (reflection)

NIR Channel

- Bandpass filter D680/40X
- Beam splitter 585DCXR (transmission)
- Beam splitter 515DCXR (transmission)
- Beam splitter 61002BS (reflection)

Filters and Beam Splitter in the Emission Paths

The beam splitters and filters are listed in the order related to their position in the optical path starting from the objective lens.

Blue Channel

- Beam splitter 61002BS (transmission)
- Beam splitter 565DCXR (reflection)
- Beam splitter 500DCXR (reflection)
- Bandpass filter ET455/50M

Green Channel

- Beam splitter 61002BS (transmission)
- Beam splitter 565DCXR (reflection)
- Beam splitter 500DCXR (transmission)
- Mirror
- Bandpass filter ET525/50M

Red Channel

- Beam splitter 61002BS (transmission)
- Beam splitter 565DCXR (transmission)
- Beam splitter 770DCXR (reflection)
- Mirror
- Bandpass filter ET620/60M

NIR Channel

- Beam splitter 61002BS (transmission)
- Beam splitter 565DCXR (transmission)
- Beam splitter 770DCXR (transmission)
- Bandpass filter HQ775/50X

4.1.4. Cameras

The cameras used in this project are the monochrome Ethernet cameras scA1400-30gm from the company Basler. The sensor (Sony ICX285AL) provides a resolution of 1392 pixels in the horizontal direction and 1040 pixels in the vertical direction. The pixels are square-shaped with an edge length of $6.45\mu m$. The bit depth of the analog-to-digital converter is 12 bits [*User's manual for GigE vision cameras* 2011].

4.2. Mechanics

4.2.1. Body Housing

The body housing is made of $4cm$ wide aluminum profiles in robust version so that it is stable enough for the movements of the stages.

It is essential to fine-adjust the two lateral axes to each other. The axis with the CMU is hold at all four corners of the housing. At each corner there is a screw with a thread pitch of $0.7\frac{mm}{rotation}$. This allows to adjust the tilt of the optical axis, the longitudinal tilt of the stage and the distance towards the other axis (Figure 4.13(a)). The axis with the stage holding the substrate offers an adjustability for its longitudinal tilt with a

screw also featuring a thread pitch of $0.7\frac{mm}{rotation}$ (Figure 4.13(b)). To adjust the lateral angle between the axes, they can be moved on each side, where they are mounted to the holding frame.

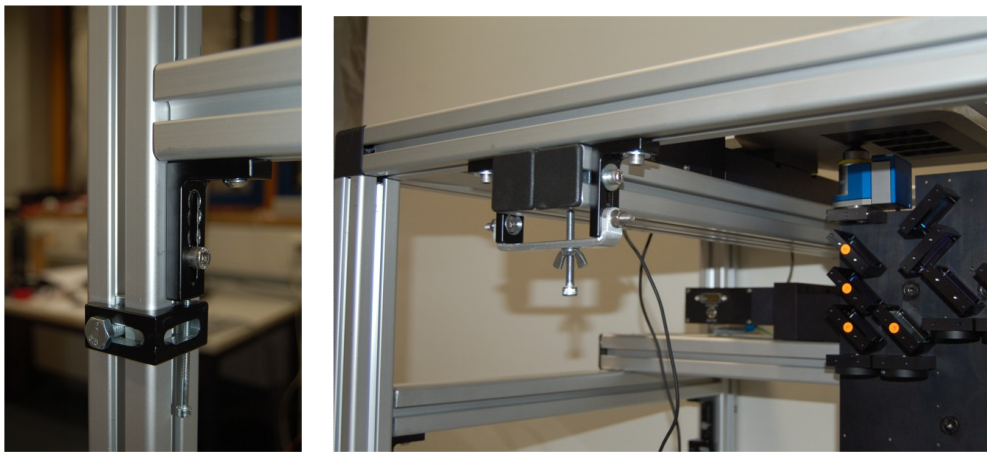

(a) Lower axis (b) Upper axis

Figure 4.13.: Fine adjustment

4.2.2. Lateral Movement

The lateral movement is accomplished with two stages from the company Physik Instrumente. The substrate holder is moved by stage M-404.6PD and the CMU itself by stage M-414.3PD.

Stage M-404.6PD features a travel range of $150mm$, a typical resolution of $0.25\mu m$, a typical unidirectional repeatability of $0.5\mu m$ and a maximum velocity of $50\frac{mm}{s}$ [*MP79E User Manual* 2007].

Stage M-414.3PD has a travel range of $300mm$, a typical resolution of $0.5\mu m$, a typical unidirectional repeatability of $0.5\mu m$ and a maximum velocity of $100\frac{mm}{s}$ [*MP81E User Manual* 2007].

4.2.3. Focusing

The focusing is done with the piezoelectric objective lens positioning system MIPOS500 from the company Piezosysteme Jena. It features a range from $0\mu m$ to $400\mu m$ with a resolution and typical repeatability of $12nm$ in closed loop operation [*microscopel objective/lens positioning system MIPOS500* 2011].

4.3. Controlling the Microscope

4.3.1. Controller Board

Light Sources and Camera Triggers

To control the light sources and the camera triggers a FPGA-board, developed at the Chair of Circuit Design at the University of Heidelberg, is used. The FPGA-board features four jack plug outputs with current control for the light sources, four 15-pin D-Sub connectors for the cameras, four TTL-level SMA connectors, of which two are used to control the mechanical shutter for the red channel, and three RS-232 connectors, which are not used in this project. The board is connected to the computer via USB.

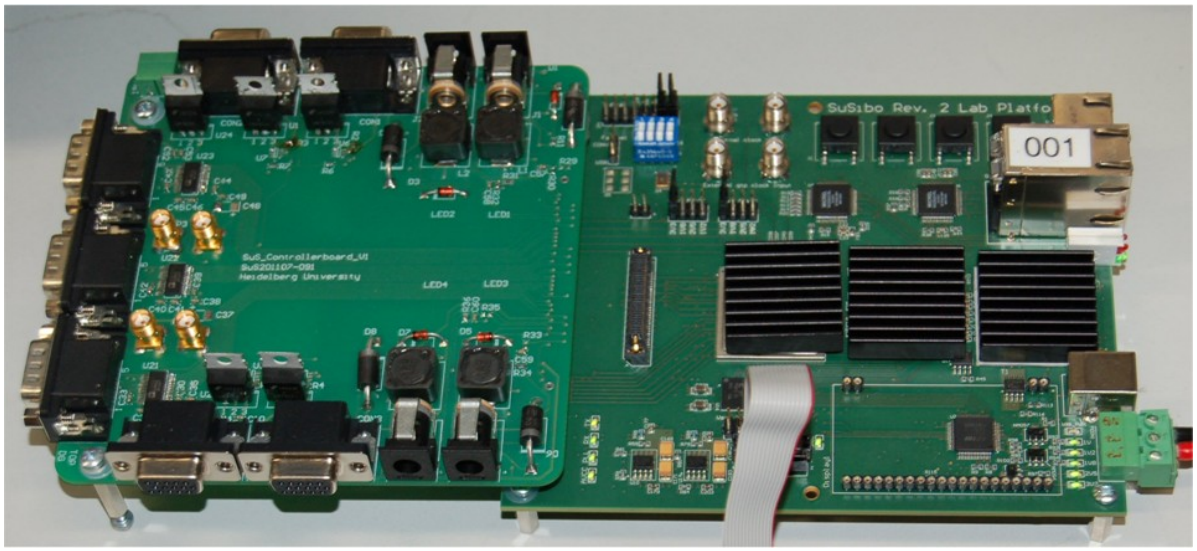

Figure 4.14.: FPGA controller board

Moving Axes

Both lateral moving stages are connected via USB with the computer. The focusing unit uses an RS-232 interface.

4.3.2. Controller Application

All components of the microscope are controlled through one Dynamic Link Library (DLL) written in C++. The functions, its parameters and return values are fully compatible with C, hence the use of the DLL is possible with almost every programming language that supports DLLs.

The DLL offers full control over each component in the microscope setup. An overview about the functionality of the DLL in respect to each component is listed hereafter.

Cameras

Information:

- Serial number
- Sensor size

Parameters:

- Image size
- Binning
- Bit depth
- Exposure time
- Gain
- Black level
- Frames per seconds
- Listen to global trigger
- Global trigger delay

Operation:

- Single frame grabbing
- Streaming

Stages

Information:

- Position

Parameters:

- Velocity

Operations:

- Move absolute

- Move relative

Focusing Unit

Information:

- Position

Operations:

- Move absolute

Light sources

Parameters:

- Duration when switched on
- Use duration
- Current
- Listen to global trigger
- Global trigger delay

Operations:

- Trigger
- Switch off

Global Trigger

It is important to trigger the camera acquisition and the light sources at the same time. Therefore a global trigger was implemented on the controller board. The parameter 'global trigger delay' for the cameras and the light sources offers the possibility of fine-adjusting the synchrony.

Communication with the Controller Board

The DLL communicates with the controller board via USB. As an example the instruction for configuring the light sources is shown in Table 4.2.

Byte	Content
0	0x01 (write)
1	Address of light source
2	12 (number of following bytes)
3	Current index MSB
4	Current index LSB
5	Use duration
6	Duration MSB
7	Duration Byte 2
8	Duration Byte 1
9	Duration LSB
10	Listen to global trigger
11	Global trigger delay MSB
12	Global trigger delay Byte 2
13	Global trigger delay Byte 1
14	Global trigger delay LSB

Table 4.2.: Machine instruction for the configuration of a light source

5. Analysis of the Image Quality

5.1. Deformation of the Beam Splitters

5.1.1. Measurement

The surfaces of three beam splitters and one mirror were measured (Figure 5.1). The obtained height distribution of the first beam splitter has a range of $3.6\mu m$, the second beam splitter features a range of $9.4\mu m$ and the range of the third beam splitter is $10.2\mu m$. The height distribution of the mirror is optical-flat with deviations significant below $1\mu m$. At the edges it shows deviations in the magnitude order of $1\mu m$, which have no influence on the image quality as they are nearly completely located outside of the light beam diameter of $20mm$.

The beam splitters have a slight, primarily spherical surface. This is not a problem, as long as the incident angle of the light is orthogonal to the beam splitter surface. In this case the spherical part of the deformation can be compensated completely by adjusting the distance between tubus lens and image plane (Figure 5.2). The remaining blur derives from the non-spherical part of the deformation. But in the setup of the microscope, the beam splitters reside in the light path with an angle of 45°, hence the aberrations are no longer spherical and cannot be compensated by refocusing.

In the excitation path the deformations do not play a significant role. In the imaging path there are two different scenarios: When used in transmission, they mainly produce a phase shift, which does not affect the image quality. When used in reflection, the deformations produce a position-dependent defocus. Due to this local dependency the image is blurred.

5.1.2. Simulations

The height distributions are used in a Zemax simulation to get an estimate of the impact on the sharpness of the images. The objective lens and the tubus lens are modeled as perfect lenses as there are no simulation models available for these components from the vendor Zeiss. Another reason for using perfect lenses is that the simulation results are then only affected by the reflection at the beam splitters. The focal length of the objective lens is set to $16.45mm$, the focal length of the tubus lens to $164.5mm$. This

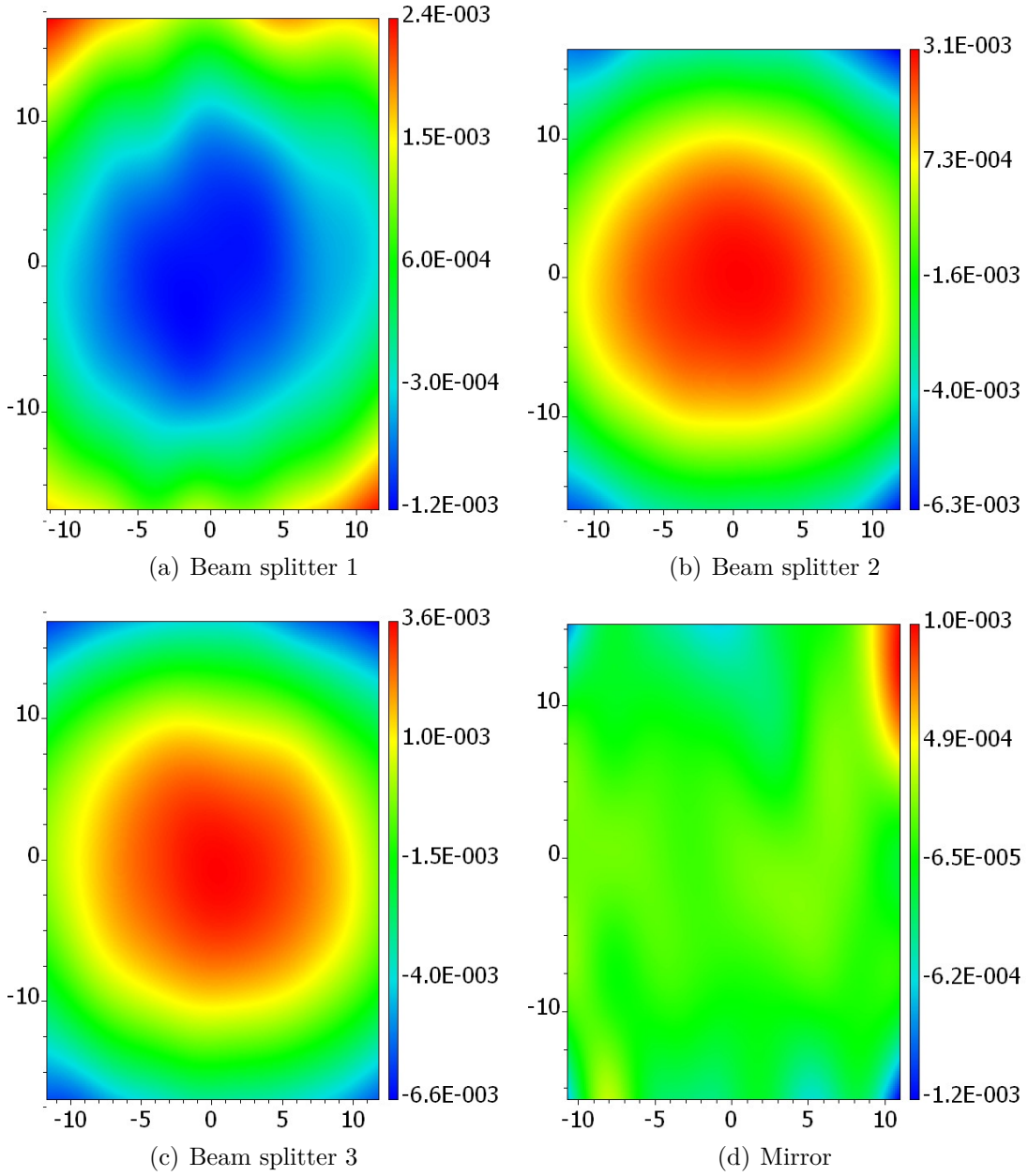

(a) Beam splitter 1

(b) Beam splitter 2

(c) Beam splitter 3

(d) Mirror

Figure 5.1.: Measured height distributions of the beam splitters and the mirror (units are mm)

leads to the desired magnification of 10.

The source image resolution is chosen in such a way that it perfectly matches the real camera sensor parameters when the imaging is carried out with a magnification factor of 10. Thus it has 1392 pixel in the horizontal and 1040 pixel in the vertical direction, which leads to a height of 670.8μm and a width of 897.84μm with a pixel size in both directions of 0.645μm. 500 dummy structures representing cells with a length of 50μm and a width of 25μm are placed on the image.

Figure 5.2(a) depicts the resulting image when a perfect mirror is placed orthogonally to the light path. The image shows no blurring at all and the resulting magnification is 10. With the height distribution of beam splitter 3 the propagated image (Figure 5.2(b)) is only slightly blurred after adjusting the image distance. The resulting magnification is 9.90, which is caused by the refocusing in order to compensate the spherical part of the aberrations.

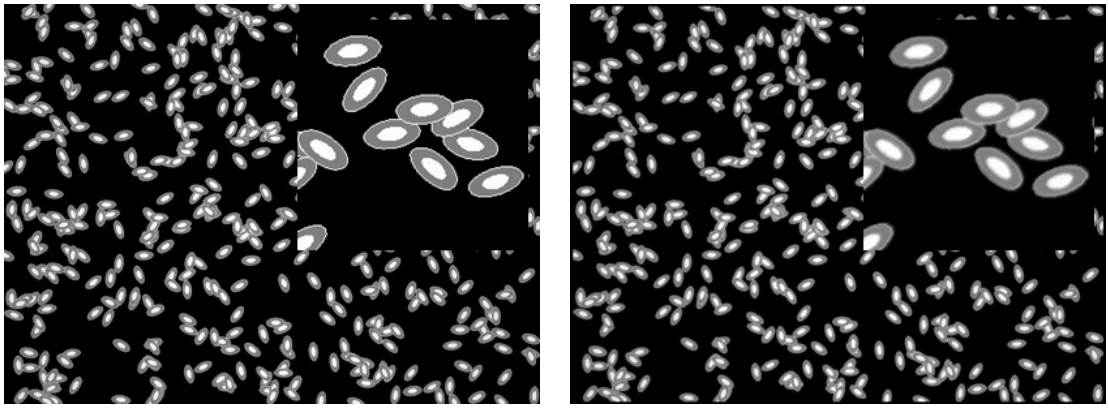

(a) Planar mirror (b) Beam splitter 3

Figure 5.2.: Simulated images with perpendicular reflection and refocusing

When the reflecting surfaces are located in an angle of 45°, the images are strongly blurred even after refocusing (Figure 5.3). This results from the spherical deviations of the beam splitters, which lead to an astigmatism when they are located in the optical path with an angle of 45°. The astigmatism can clearly be seen in Figure 5.4. When using beam splitter 3 the root-mean-square value of the spot radius at the outer bound is $43.499\mu m$.

The only way to achieve sharper images under the reflection of 45° is to insert an aperture in front of the tubus lens, thus the depth of focus is enlarged. Then an image similar to the one when the reflecting element is placed orthogonally to the light path is reached (Figure 5.5). The drawback of inserting an aperture is a strong loss of intensity, especially when an aperture of $4mm$ diameter (light beam diameter is $20mm$) is used as it was necessary in the simulation. Then the root-mean-square value of the spot radius is $8.826\mu m$ (beam splitter 3).

According to the manufacturer Chroma Technology the beam splitters are fabricated with a flatness of $10\frac{\lambda}{inch}$. This value corresponds to the measured deformations. A flatness down to $\frac{1}{10}\frac{\lambda}{inch}$ is principally possible on the basis of specially manufactured beam splitters. With such optical flat beam splitters a sharp imaging in every channel can be achieved.

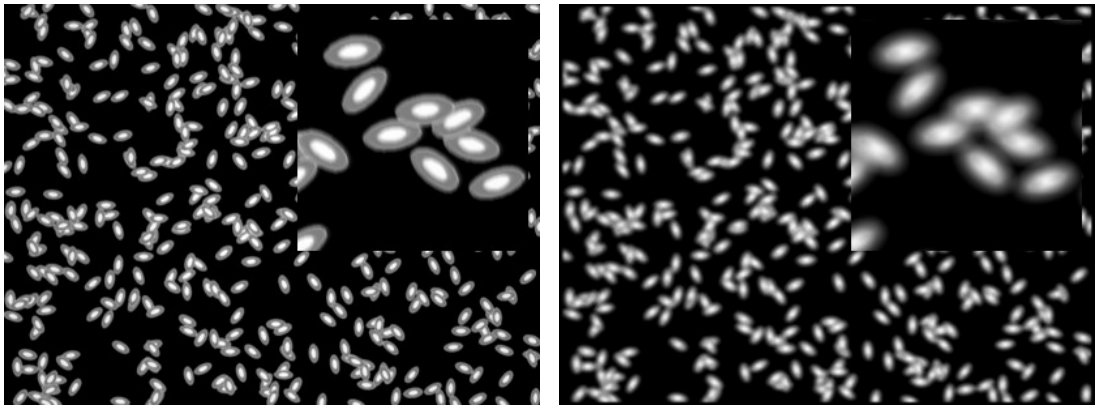

(a) Beam splitter 1

(b) Beam splitter 2

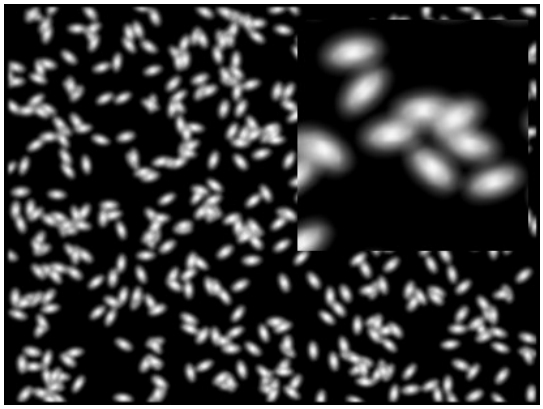

(c) Beam splitter 3

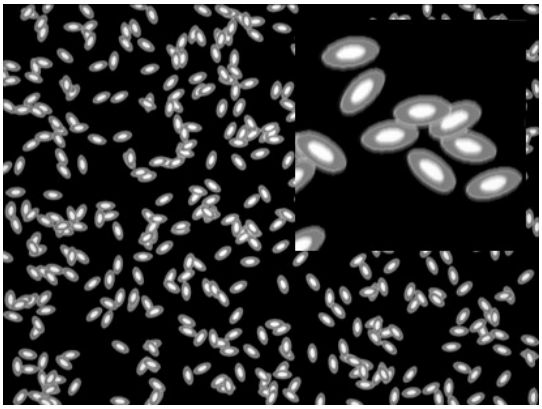

(d) Mirror

Figure 5.3.: Simulated images with 45° reflection and refocusing

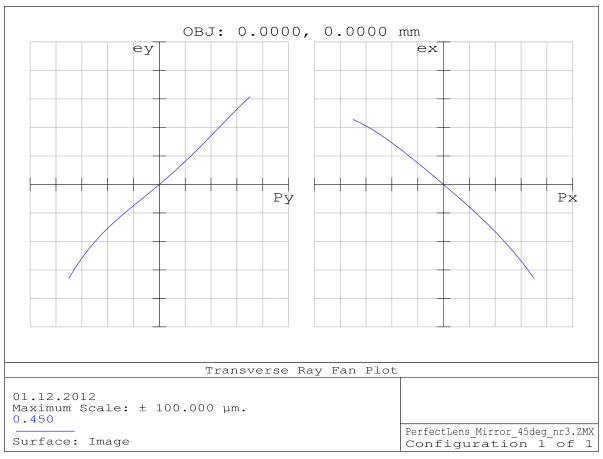

Figure 5.4.: Ray aberrations as functions of pupil coordinates (beam splitter 3)

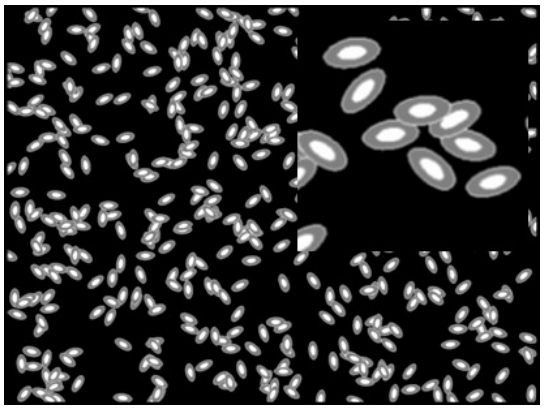

Figure 5.5.: Simulated image with an aperture in front of the tubus lens (beam splitter 3)

5.2. Experimental Results

5.2.1. Image Distance

It is important to align the camera and the tubus lens to the correct image distance. Otherwise the image quality and the magnification will not be optimal. This is done by using a collimated laser beam that goes through the tubus lens and then adjusting the distance of the camera thus that the focus on the camera sensor has the smallest possible radius. The setup is shown in Figure 5.6.

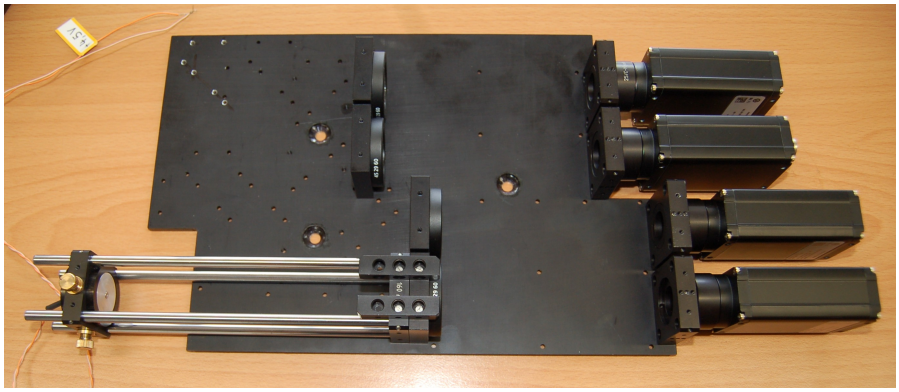

Figure 5.6.: Image distance setup

The adjustment is only performed for the NIR channel, which is then the reference for the other channels. This is due to the fact that the channels have different optical paths and therefore a different count of reflections on beam splitters, which produce aberrations caused by their non-planar surface. In the NIR channel the beam splitters are only used in transmission, which has almost no effect on the imaging quality. The aberrations can be corrected to a certain amount by refocusing. Hence the ideal image distance, which can be found by the adjustment explained here, would lead to unsharp images in the channels.

The ideal image distance of the other channels is determined by adjusting the object distance so that a sharp image at the reference channel can be observed. This ensures, that the correct object distance is set. Now the image distances of the channels are adjusted until the images appear in the best sharpness and resolution possible.

5.2.2. Images of a Siemens Star

Resolution

The resolution of each channel is analyzed by imaging a Siemens star with 30 spokes and a radius of $400\mu m$. In order to be able to measure the magnification, the offset and the tilt, it is surrounded by a square-shaped frame with a length of the edges of $500\mu m$. The Siemens star was manufactured lithographically on a chrome coated glass substrate and illuminated from the back with a white light source. The camera images are depicted in Figures 5.10, 5.9, 5.7 and 5.8.

From the images the magnification is calculated. The magnification should ideally be $m = 10$ as the objective lens together with the used tubus lens is designed to feature this factor. The resulting values for each channel are listed in Table 5.1. The NIR channel matches the ideal magnification, which confirms that the adjustment of the image distance was correct, whereas the other channels show slight deviations and produce smaller images of the object. This is caused by the process of refocusing in order to compensate the aberrations produced by the reflections at the beam splitters.

Channel	Magnification
$Blue$	9.82
$Green$	9.92
Red	9.95
NIR	10

Table 5.1.: Magnification

The maximum resolution δx, which can be resolved by the system, is calculated with the count of spokes N_{spokes} and the minimum radius r_{min} at which the spokes are still separated in the image:

$$\delta x = \frac{\pi r_{min}}{N_{spokes}}$$

In Table 5.2 the maximum resolutions for the channels are found. While the NIR channel can clearly resolve features below $1\mu m$, the other channels are only able to resolve features between $2\mu m$ to $3\mu m$.

Channel	δx
$Blue$	$2.20\mu m$
$Green$	$2.53\mu m$
Red	$2.70\mu m$
NIR	$< 1\mu m$

Table 5.2.: Maximum resolution in absolute dimensions at the object plane

The resolution of the NIR channel is better than that of the lithographic process, which is able to resolve structures down to $0.8\mu m$. In the case of the chrome mask, the finest structures are $\sim 1\mu m$. This resolution limit, which is represented by the big white area in the middle of the Siemens star, can clearly be seen in Figure 5.10. The spokes are well resolved even at the border of this area.

The red, blue and green channels show a resolution which is below the resolution of the chrome mask. The detailed views of the camera images show that the blurring is not radially symmetric, which is a sign for the astigmatism in the optical system predicted by the simulations.

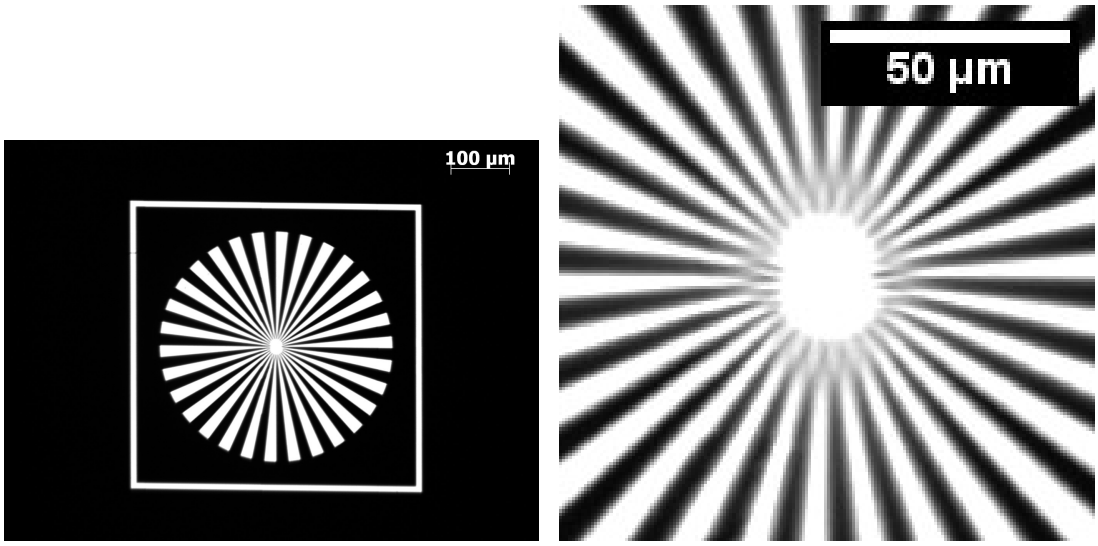

(a) Complete camera image (b) Detail

Figure 5.7.: Siemens star in the blue channel

Offset and Tilt

The offset relative to the NIR channel, which serves as a reference, was calculated from images taken from the same lateral position of the object. As can be seen in Figure 5.11 the offset strongly varies between the different channels. Table 5.3 lists the offsets in both lateral directions in pixel and in absolute dimensions at the object plane.

Especially the red channel features a large offset in the vertical direction. This is caused by the fixation of the beam splitters and mirrors. They are fixed with countersink screws, but the play of the fixation is large. The mirror in the red channel for instance can be tilted and then fixed with the screws in a way that offsets of more than the sensor size are reached. As the metal plate, on which the components are fixed, is itself fixed to the stage with its back, the alignment of most of the components cannot be accomplished in the setup. Hence no live image can be used for the adjustment.

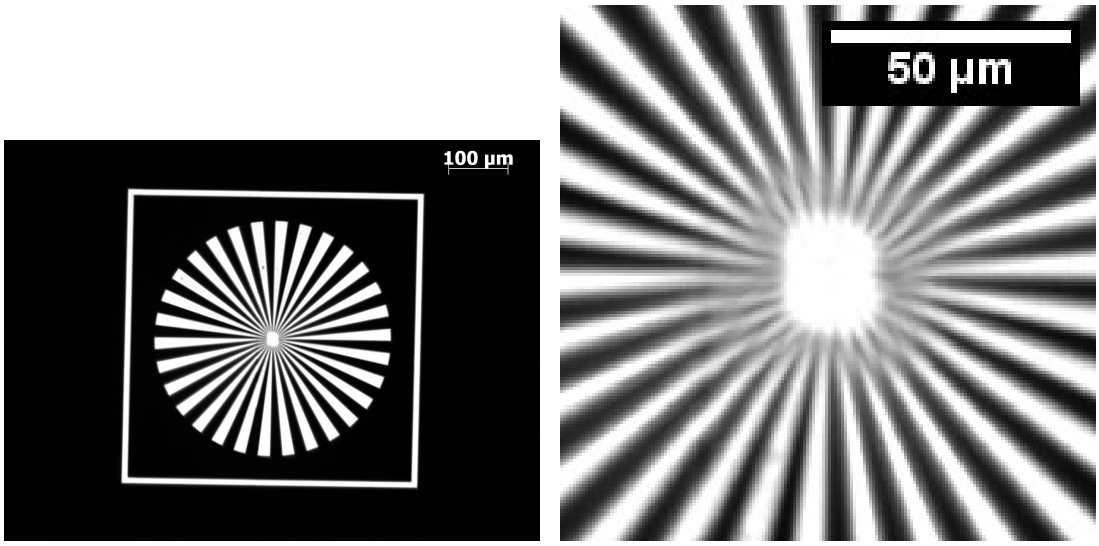

(a) Complete camera image (b) Detail

Figure 5.8.: Siemens star in the green channel

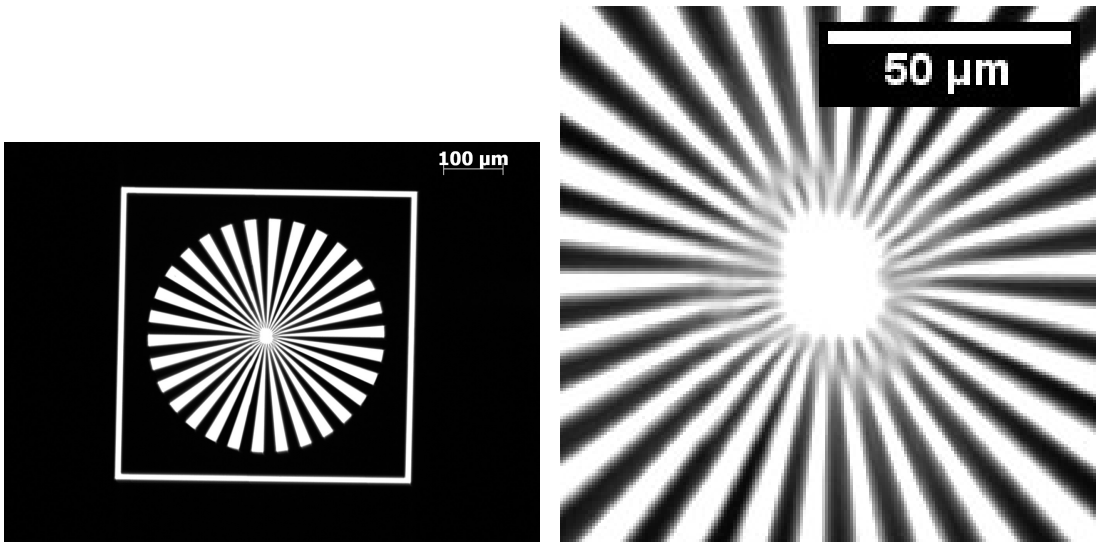

(a) Complete camera image (b) Detail

Figure 5.9.: Siemens star in the red channel

The tilts of the channels relative to the reference channel (NIR) are small (Table 5.4). The green channel features almost no relative tilt, whereas the maximum tilt of 0.13° is found in the blue channel.

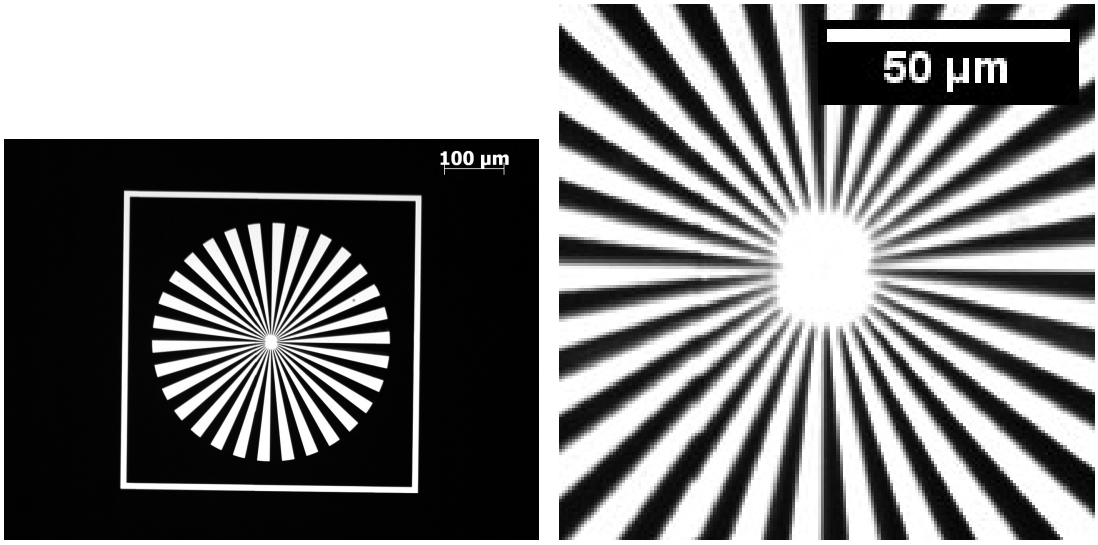

(a) Complete camera image (b) Detail

Figure 5.10.: Siemens star in the NIR channel

Channel	Offset
Blue	$\begin{pmatrix} -18 \\ -225 \end{pmatrix} px = \begin{pmatrix} -116.1 \\ -1451.25 \end{pmatrix} \mu m$
Green	$\begin{pmatrix} 35 \\ -95 \end{pmatrix} px = \begin{pmatrix} 225.75 \\ -612.75 \end{pmatrix} \mu m$
Red	$\begin{pmatrix} -138 \\ -610 \end{pmatrix} px = \begin{pmatrix} -890.1 \\ -3934.5 \end{pmatrix} \mu m$

Table 5.3.: Offset in pixel and absolute dimensions at the image plane

Channel	$\Delta\phi$
Blue	$0.13°$
Green	$-0.01°$
Red	$0.07°$

Table 5.4.: Tilt relative to the reference channel

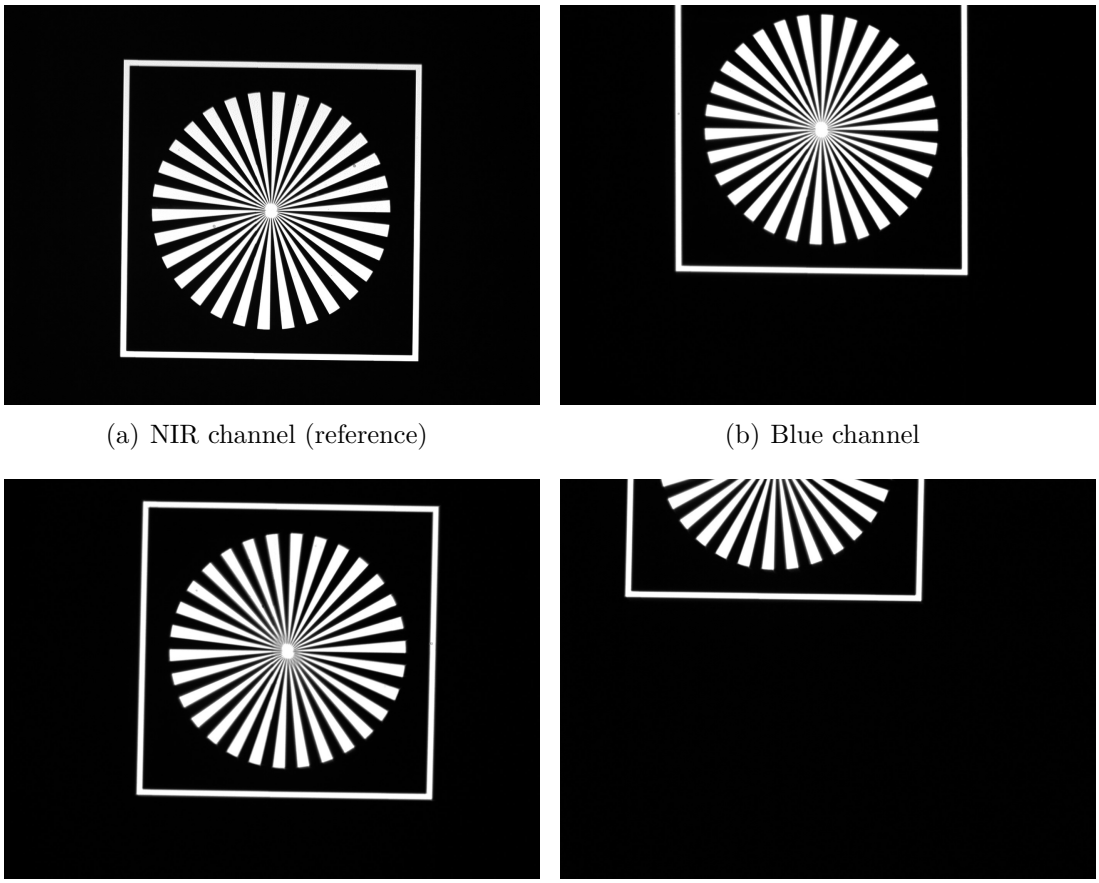

(a) NIR channel (reference)

(b) Blue channel

(c) Green channel

(d) Red channel

Figure 5.11.: Offset and tilt comparison

5.2.3. Images of Stained Cells

The cell probes were kindly prepared by the group of Nathan Brady, PhD, at the DKFZ in Heidelberg. The fixed human cells were stained with the fluorophores Hoechst 33258, GFP, mCherry and DRAQ5.

In addition to the fluorescence image a white light image is taken for every channel to get an impression which structures are in the field of view.

Figure 5.12 shows the camera images of the blue channel (Hoechst 33258). The exposure time for the fluorescence image is $80ms$. As there are deformed beam splitters used in reflection in the optical path of this channel the image is blurred.

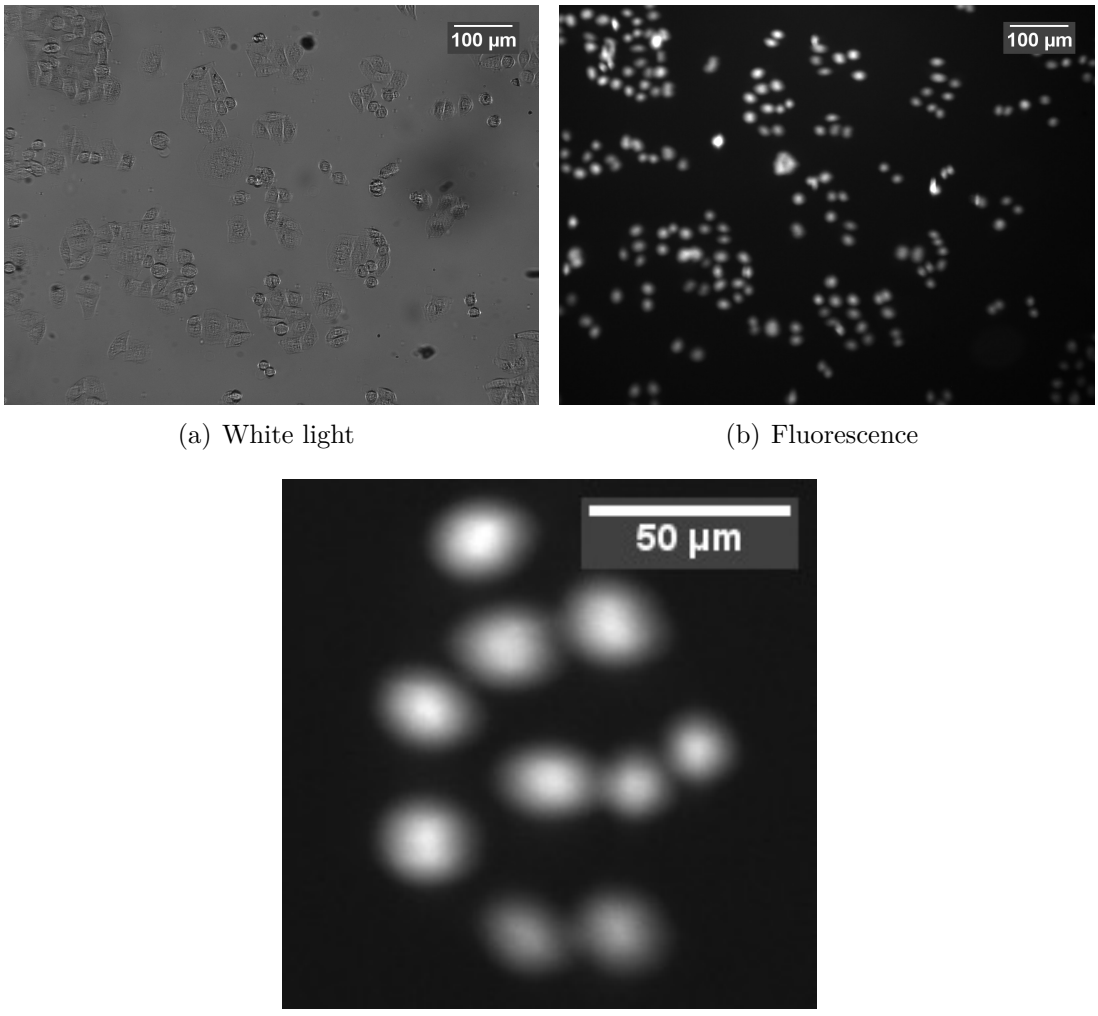

(a) White light (b) Fluorescence

(c) Detail

Figure 5.12.: Camera images of the blue channel

The camera images of the green channel (GFP) are found in Figure 5.13. The exposure time for the fluorescence image is $4000ms$. The image also shows the predicted blur.

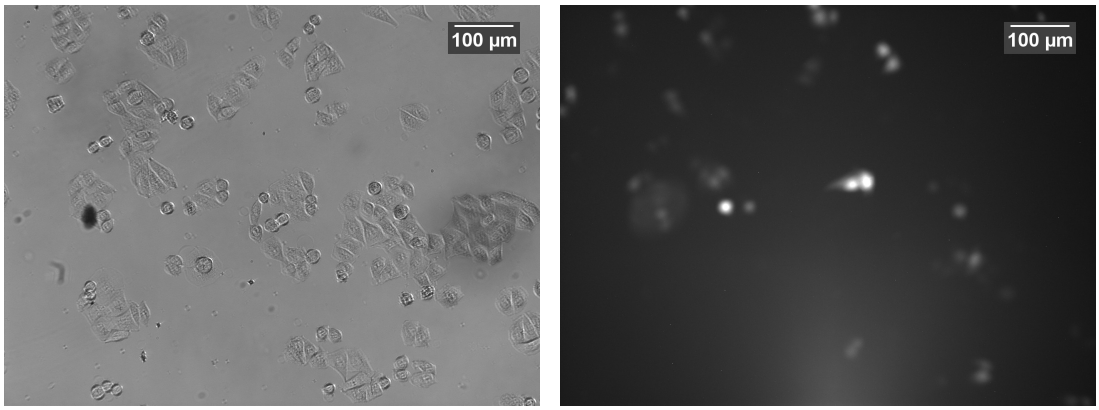

(a) White light (b) Fluorescence

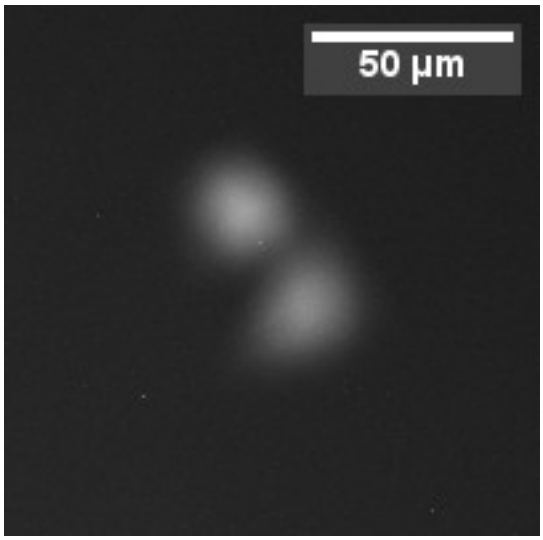

(c) Detail

Figure 5.13.: Camera images of the green channel

The fluorescence image of the red channel (mCherry), depicted in Figure 5.14, also shows a blur as it was predicted by the simulations with the measured beam splitters. The exposure time for the fluorescence image is $9800ms$.

Figure 5.15 shows the camera images of the NIR channel (DRAQ5). The exposure time for the fluorescence image was $6000ms$. The beam splitters in the optical path are only passed in transmission, hence the image is sharp and features fine details of the observed structures.

Exposure Time and Optical Power

It is striking that the exposure times of all channels except the blue channel are very high. The range is between $4s$ and $9.8s$. Only in the blue channel an exposure time of

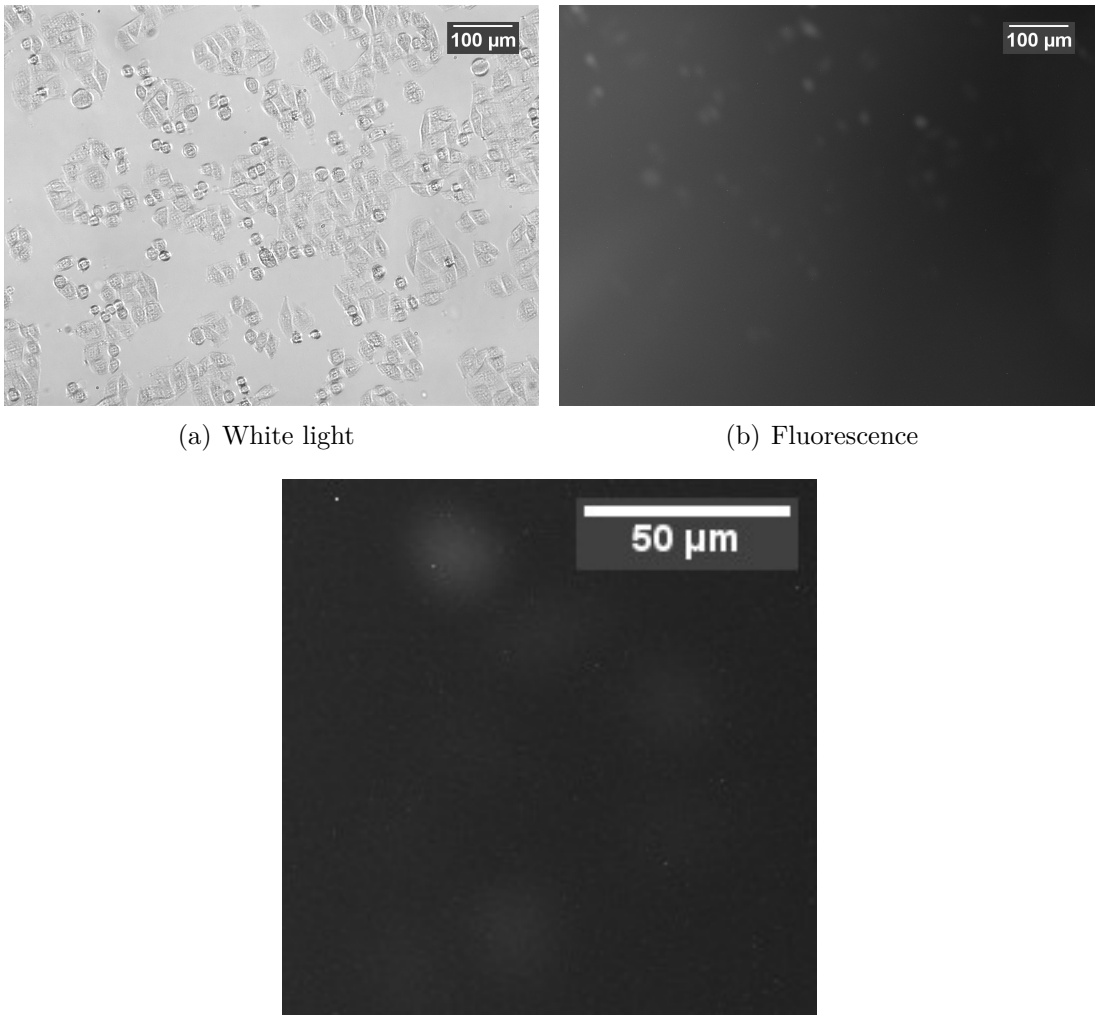

(a) White light

(b) Fluorescence

(c) Detail

Figure 5.14.: Camera images of the red channel

$80ms$ is realized, which makes fast scanning of the probe possible. The reason for these high exposure times is the low optical power of the used light sources and the different quantum yields and concentrations of the fluorophores. The blue channel features the light source with the highest optical power of $9.13mW$, whereas the source in the red channel, where only an underexposed image at the maximum exposure time of the camera was obtained, has just an optical power at the object plane of $0.85mW$.

Exposure times which are small enough to make fast scanning possible can be achieved by using light sources which offer higher optical power. As the optical power of available LEDs is not sufficient it is suggested to use lasers instead.

For the blue channel, where an excitation wavelength between $350nm$ and $358nm$ (depending on the fluorophore) would be optimal, a laser with $355nm$ could be used, which is available up to an optical power of $250mW$ (Coherent Genesis CX STM-Series). But as the UV-LED delivers enough power, it need not be substituted.

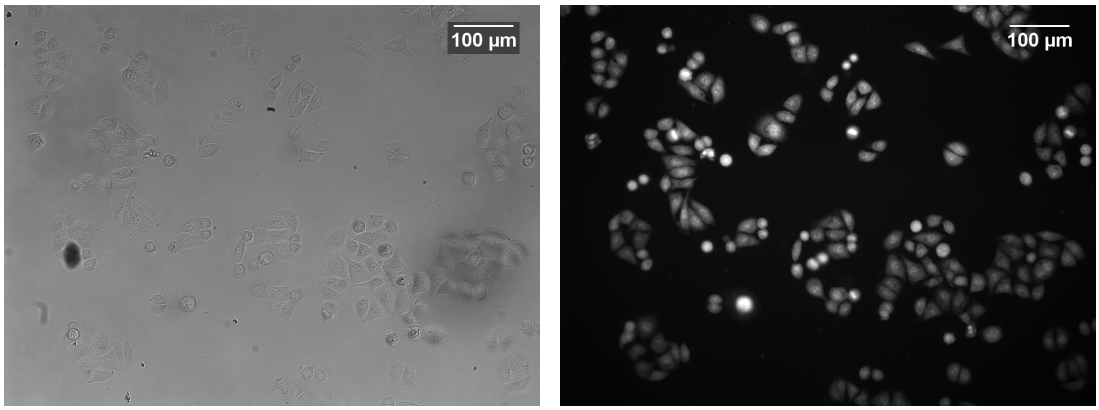

(a) White light (b) Fluorescence

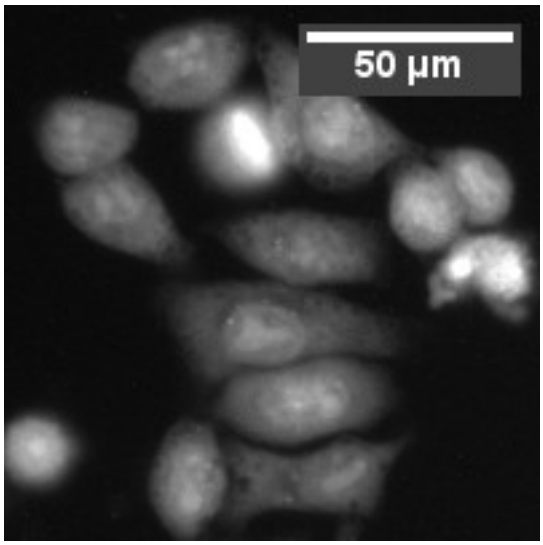

(c) Detail

Figure 5.15.: Camera images of the NIR channel

For the green channel, where the optimum excitation wavelength would be $488nm$, a laser with exact this wavelength is available featuring an optical power up to $4W$ (Coherent Genesis CX STM-Series).

The optimum excitation wavelength for the red channel would be between $584nm$ and $587nm$, but this is limited by the required beam splitters. So a good choice would be a laser with $568nm$, available with an output power up to $200mW$ (Coherent Sapphire 568 LP).

For the NIR channel the optimum excitation wavelength is $646nm$ but as the beam splitter 61002BS would block this in reflection, a laser with $660nm$ is recommended. A laser with this wavelength and an optical power of $100mW$ is available (Coherent CUBE 660-100C).

6. Summary

With the concept presented here, it is possible to observe different cell structures, which are marked with four different fluorophores, at the exact same point in time. Compared to state-of-the-art automated fluorescence microscopes, there are no filter wheel movements needed to select the desired excitation and emission bands. The only moving parts are the two lateral axes and the piezoelectric focusing unit when another position on the substrate is meant to be observed. Therefore the rate of analysis can be increased and only depends on the exposure time and the time needed to move to different positions.

The implementation validates the principal feasibility of the concept. The blur in the images of the blue, green and red emission channels arises from the reflections at the beam splitters, which possess a slight, mainly spherical surface deformation. Exchanging these elements through optical flat beam splitters will eliminate the astigmatic aberrations and will lead to images which are as sharp as the ones obtained in the NIR channel.

The type of fixing the single components to the base plate has to be revised, as every component can be tilted and then fixed within a huge angle range without the possibility of a fine adjustment.

The main drawback of the implemented system is the lack of optical power of the light sources. Only the blue channel, which is equipped with a light source featuring the highest optical power of $9.13mW$ in this system at the object plane, offers enough intensity at the image plane to permit a fast scanning of the probes. The concept was laid out to use high power LEDs as light sources, but the available LEDs still feature too less optical power. Only in the UV are the LEDs suitable for this application. Especially in the red channel, where an excitation band of $570nm \pm 10nm$ is needed, no high power LEDs are available now.

As long as the available LEDs do not fulfill the power requirements, it is suggested to switch to laser.

Part III.

Miniaturized Parallel Fluorescence Microscope

7. Concept

7.1. Introduction

In this chapter the concept for a miniaturized parallel fluorescence microscope is presented, which uses GRIN rod lenses for the illumination and imaging paths. In contrast to available systems from the company DMetrix, who use arrays of microlenses [Olszak et al. 2011], the approach described here integrates the illumination path into the imaging path, thus enabling efficient fluorescence microscopy. Included is a discussion about the influence of the parallelization on the total scan time as well as the advantages of a scaled down optical system.

7.2. Classic Image Acquisition with One Objective Lens

Off-the-shelf automated microscopes work with only one objective lens, which has a field of view larger than the spot size (diameter of the single experiment). Therefore the spots on the substrate have to be observed one after one. This procedure consist of alternating sequences of movements and image acquisitions. With the given width W and height H of the substrate, the distances of the spots in both directions d_w and d_h respectively and the exposure time τ_e, the time T_I needed for the image acquisitions is:

$$T_I = \frac{W}{d_w}\tau_e\frac{H}{d_h}$$

The time T_M needed for all movements between the spots is:

$$T_M = \frac{1}{v}\left(\frac{W}{d_w}H + W\right)$$

with v being the velocity of the movement. The total time needed to have an image of all spots on the substrate is:

$$\begin{aligned} T &= T_I + T_M \\ &= \frac{W}{d_w}\tau_e\frac{H}{d_h} + \frac{W}{d_w}H + W \\ &= WH\left(\frac{\tau_e}{d_w d_h} + \frac{1}{v d_w}\right) + \frac{W}{v} \end{aligned}$$

7.3. Scanning the Substrate

In contrast to the classic image acquisition an image of the whole substrate is obtained when the images are taken during movement. As for scanning the sensor is a line sensor, the relevant dimension of the field of view is its width w_{FOV} (Figure 7.1).

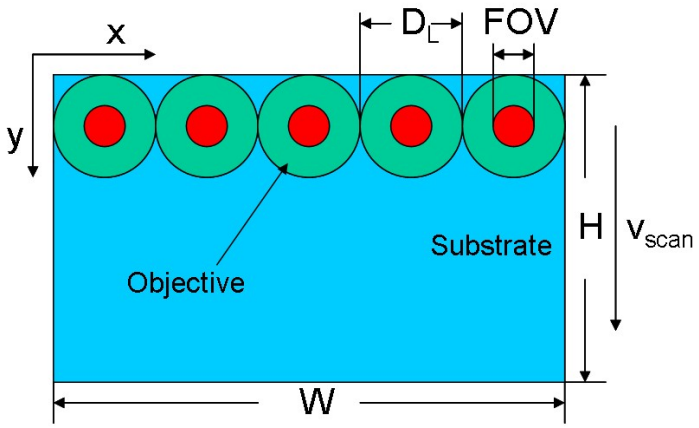

Figure 7.1.: Multiple objectives scanning a substrate

The time to scan the whole substrate with one objective lens is:

$$\begin{aligned} T_1 &= \frac{H}{v_{scan}} \frac{W}{w_{FOV}} + \frac{W}{v_{scan}} \\ &= WH \frac{1}{v_{scan} w_{FOV}} + \frac{W}{v_{scan}} \end{aligned}$$

When using more than one objective lens in x direction the time needed for a whole scan scales directly with the number of the objective lenses N:

$$\begin{aligned} T_N &= \frac{T_1}{N} \\ &= \frac{1}{N} \frac{H}{v_{scan}} \frac{W}{w_{FOV}} + \frac{1}{N} \frac{W}{v_{scan}} \end{aligned}$$

Since in most cases the width of the field of view w_{FOV} is smaller than the outer diameter of the lens D_L, D_L is a limiting factor for the degree of parallelization perpendicular to the scan direction. Therefore the maximum count of lenses in x-direction N_x is:

$$N_x = \frac{W}{D_L}$$

Disregarding the movement in x-direction and using the degree of parallelization in

x-direction to full capacity, it follows then:

$$\begin{aligned} T_{N_x} &= \frac{1}{N_x}\frac{H}{v_{scan}}\frac{W}{w_{FOV}} \\ &= \frac{D_L}{W}\frac{H}{v_{scan}}\frac{W}{w_{FOV}} \\ &= \frac{D_L}{w_{FOV}}\frac{H}{v_{scan}} \end{aligned} \tag{7.1}$$

As it can be concluded from Equation 7.1, the number of scans N_{scans} needed to scan the whole substrate is:

$$N_{scans} = \frac{D_L}{w_{FOV}}$$

The ideal ratio $\frac{D_L}{w_{FOV}}$ is 1, then the substrate can be scanned in only one movement and no further objective lenses in the scanning direction are needed. A parallelization of the objective lenses in both dimensions is needed to scan the whole substrate in one movement. The parallelization in scan direction is done by adding further rows of objective lenses each shifted by the width of the field of view w_{FOV}. With the number of rows N_y the scan time is:

$$T = \frac{1}{N_y}\frac{D_L}{w_{FOV}}\frac{H}{v_{scan}} \tag{7.2}$$

Four parameters to shorten the scanning time are found in Equation 7.2: The degree of parallelization in y-direction N_y can be increased, which is limited by the size of the objective lenses and the packing density of the sensors, light sources and their electronics. The ratio $\frac{D_L}{w_{FOV}}$ can be decreased by designing objective lenses with a larger field of view which increases w_{FOV}. But this will lead to more complex optic designs for the objective. The other possibility to decrease $\frac{D_L}{w_{FOV}}$ is to scale down the objective lens and therefore D_L. The advantages of this alternative are discussed in 7.4. The fourth parameter to shorten the scanning time is the scanning velocity v_{scan}, which mainly depends on the needed exposure time of the sensors.

7.4. Scaling an Optical System

Scaling down an optical system leads to a compact system design, which has the advantage that the parallelism can be deployed more efficiently, since the packing density is much higher. Another big advantage of a scaled down optical system is, that - in terms of ray optics - all parameters especially the aberrations are also scaled down [Lohmann 1989] (Figure 7.2).

One of the most important parameters in an imaging system is the spot size. It is assumed that the radius of the spot r_s follows a parabolic curve as a function of the lens radius r_l:

$$r_s = A + Br_l^2 \tag{7.3}$$

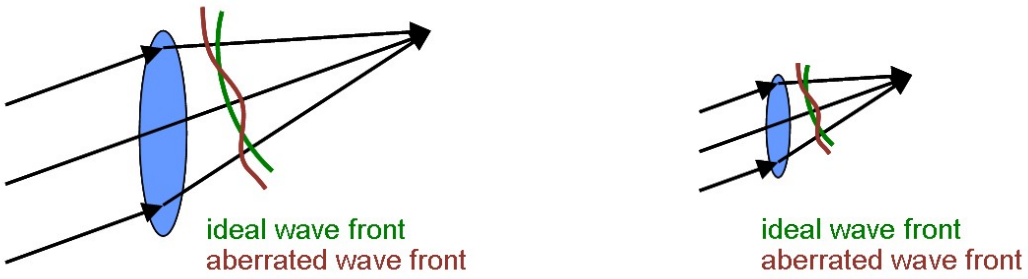

(a) Original lens size (b) Scaled lens size

Figure 7.2.: Scaled aberrations

with A and B being the parameters of the parabola. The diffraction limited spot radius is:

$$r_d = \frac{\lambda}{NA}$$

The imaging system should be diffraction limited even at the maximum lens radius $r_{l,max}$:

$$\begin{aligned} r_s\left(r_{l,max}\right) &= r_d \\ A + Br_l^2 &= \frac{\lambda}{NA} \end{aligned} \tag{7.4}$$

By scaling the system by the factor s, Equation 7.3 becomes:

$$r_s\left(s\right) = s\left(A + B\left(\frac{r_l}{s}\right)^2\right)$$

Considering the diffraction limit constraint (Equation 7.4), an expression for the maximum radius is obtained:

$$r_{max,s} = s\sqrt{\frac{1}{B}\left(\frac{\lambda}{sNA} - A\right)}$$

With the given magnification m of the imaging system, the expression for the width w_{FOV} of the field of view is:

$$\begin{aligned} w_{FOV,s} &= \frac{2r_{max,s}}{m} \\ &= \frac{2s}{m}\sqrt{\frac{1}{B}\left(\frac{\lambda}{sNA} - A\right)} \end{aligned}$$

Applying this to Equation 7.2 leads to:

$$\begin{aligned} T_s &= \frac{1}{N_y}\frac{sD_L}{w_{FOV,s}}\frac{H}{v_{scan}} \\ &= \frac{1}{N_y}\frac{sD_L}{\frac{2s}{m}\sqrt{\frac{1}{B}\left(\frac{\lambda}{sNA} - A\right)}}\frac{H}{v_{scan}} \\ &\sim \sqrt{s} \end{aligned} \tag{7.5}$$

The degree of parallelization in scan direction also increases when the system is scaled down, because the packing density of the objectives then is higher:

$$N_y \sim \frac{1}{s}$$

With this Equation 7.5 becomes:

$$T \sim s\sqrt{s} \tag{7.6}$$

Equation 7.6 shows that scaling down a system to a quarter of the original size results in one-eighth of the time which the unscaled system would need to complete a whole scan.

7.5. Design of the Parallel Microscope

For the miniaturized parallel microscope, systems with micro lens arrays and GRIN rod lenses as imaging components were analyzed in [Wohlfeld et al. 2009]. Micro lens arrays have to be custom-designed and the integration is complex due to the non-flat surfaces, whereas GRIN rod lenses are products off-the-shelf, have flat end faces and hence are easier to integrate into the system. Therefore, optical systems using GRIN rod lenses are preferred here.

The optical system of the miniaturized parallel microscopy consists of three layers: To guide the excitation light to the object, a beam splitter layer resides between two GRIN lens arrays (Figure 7.3), which are fixed on glass substrates (Figure 7.4).

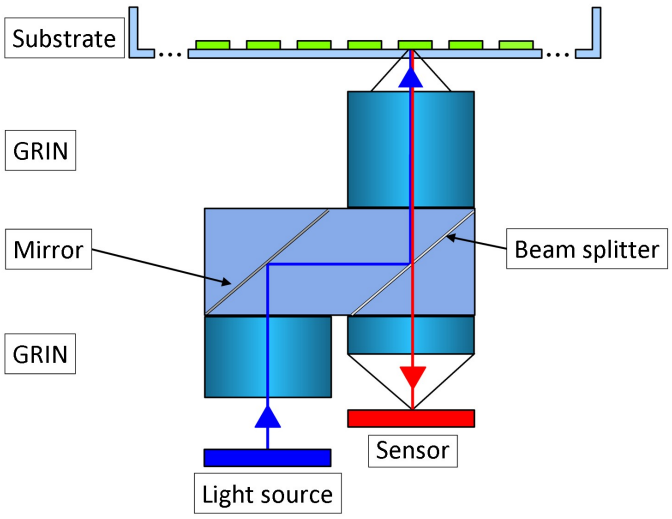

Figure 7.3.: Path of rays

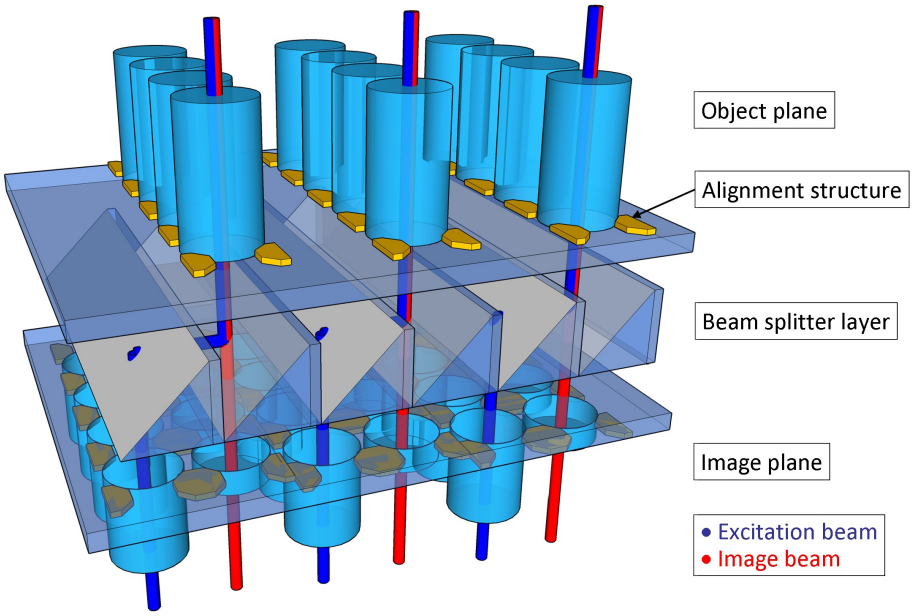

Figure 7.4.: Integration scheme of the miniaturized parallel fluorescence microscope

7.5.1. GRIN Rod Lens Model

GRIN rod lenses are glass cylinders with a gradient of their refractive index, which is typically radial-symmetric along the optical axis. The largest value of the refractive index is found at the center and decreases towards the outer bound. They are produced by diffusing material into the glass. The refraction index profile and the absorption characteristics depend on the material used for the diffusion and the process itself.

The GRIN rod lenses used here are manufactured by the company GrinTech. They are produced by silver ion exchange and the refractive index profile of the GRIN rod lenses, which ideally is a *sech*-profile, is approximated with a Taylor series:

$$n\left(r\right) = n_0 + nr_2 \cdot r^2 + nr_4 \cdot r^4$$

While the parameters n_0 and nr_2 are determined by the manufacturer, the parameter nr_4 can be used for optimization in the optic design. The standard values from GrinTech are:

$$\begin{aligned} n_0 &= 1.62893 \\ nr_2 &= -0.077 \\ nr_4 &= 0.00315 \end{aligned}$$

7.5.2. Simulation of the Imaging Path

As basis for the simulation of the imaging path a layout shown in [Wohlfeld 2009] is used. The layout is designed for the fluorophore DAPI, which has its emission peak at $461nm$ and its excitation peak at $358nm$.

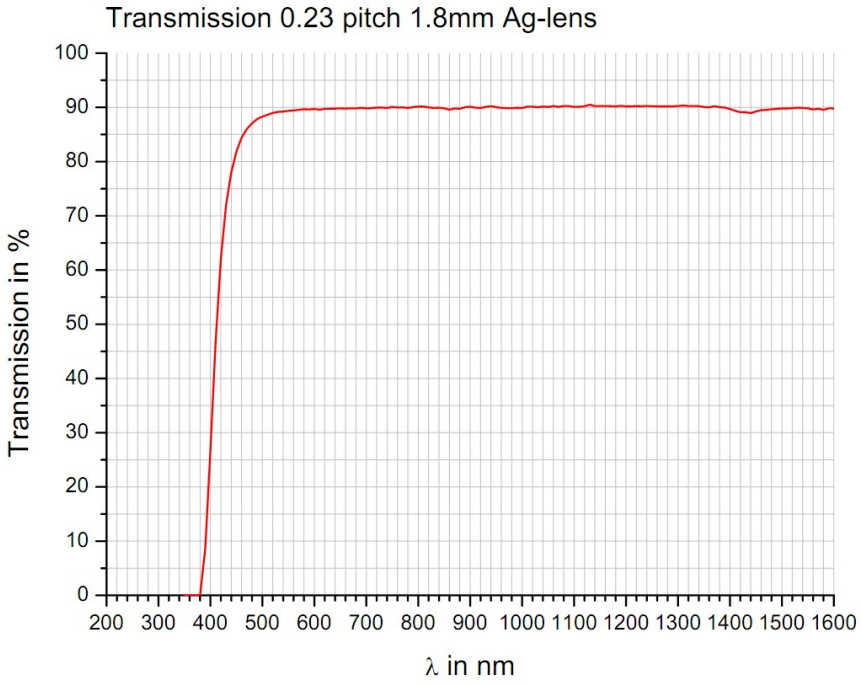

Figure 7.5.: Transmission spectrum for the GRIN rod lens (image source: GrinTech)

In the transmission spectrum for the GRIN rod lenses, shown in Figure 7.5, it can be seen, that the GRIN rod lenses are almost completely untransparent at the excitation spectrum of DAPI. Due to the fact that the second GRIN rod lens is used for both the illumination and the imaging, it is obvious that a complete optical system for DAPI can not be build with the GRIN rod lenses. Therefore the design, which is presented here, is laid out for the fluorophore EGFP, which has its emission peak at $507nm$ and its excitation peak at $488nm$.

The arrangement of the single components is depicted in Figure 7.6: The observed cell cultures are lying on a glass substrate with a thickness of $160\mu m$. The field of view is $400\mu m$. After a distance of $0.8mm$ the first GRIN rod lens, which has a diameter of $2mm$, is placed to collimate the light in such a way that the beam splitter functions properly. This lens is located on a $500\mu m$ thick glass substrate, on which the holding structures reside. The next component in the design is the beam splitter layer with a length of $2mm$. This is followed by a glass substrate with a thickness of $500\mu m$ for the holding structures and the second GRIN rod lens, which focuses the collimated beam, making the imaging system complete. The object side NA is set to 0.3, which represents an aperture behind the first GRIN lens.

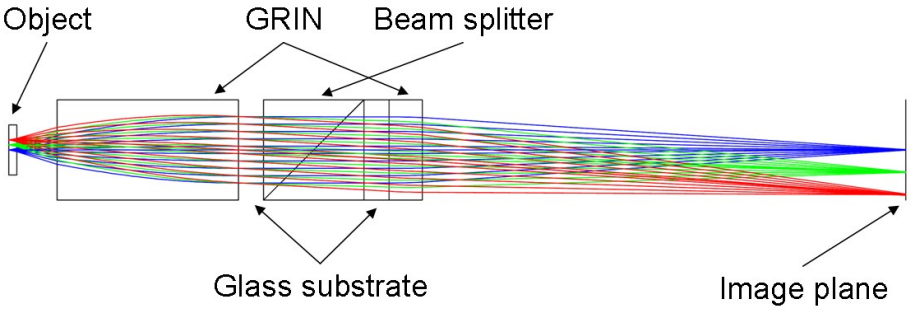

Figure 7.6.: Layout of the imaging path for EGFP

The simulation is carried out in two steps. In the first step the first GRIN rod lens is optimized to collimate the light for the proper use of the beam splitter. Therefore, the components behind the first GRIN rod lens are deactivated and the spot radius is optimized at infinity, which represents a collimated light beam. The optimization parameters are the length of the GRIN rod lens and its manufacturing parameter nr_4. After the optimization the manufacturing parameter nr_4 of the GRIN rod lens is 0.0032 and the length is $3.619mm$.

In the second step all components are activated and the optimization parameters are the length and the manufacturing parameter nr_4 of the second GRIN rod lens and the distance between the second GRIN rod lens and the image plane. The optimization goal is a magnification of 4.5. The optimized length is $666\mu m$ and the manufacturing parameter nr_4 is 0.0053. The distance of the image plane is $9.639mm$.

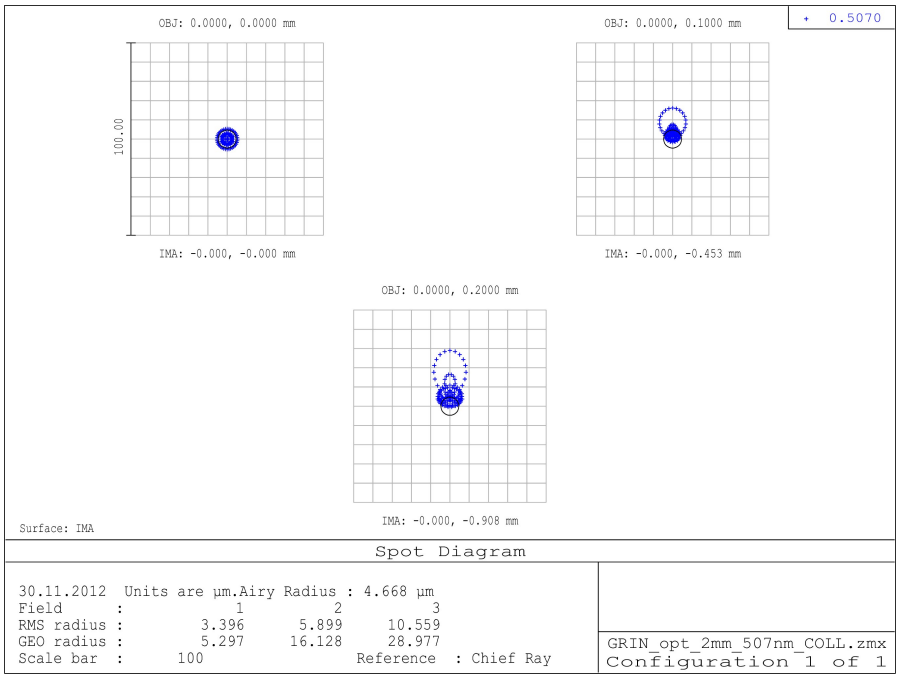

Figure 7.7.: Spot diagram of the imaging path for EGFP

The spot diagram in Figure 7.7 shows, that the root-mean-square value of the spot radius at the outer bound of the field of view is $10.559\mu m$. The airy radius is $4.668\mu m$. On the optical axis the root-mean-square value of the spot radius is $3.396\mu m$.

When after the steps in the above-mentioned simulation one optimization cycle with both GRIN lenses is performed, which is attended by a lower quality of the collimation, a diffraction limited design is reached (Figure 7.8). Then the root-mean-square value of the spot radius at the outer bound is $3.464\mu m$ (airy radius is $4.630\mu m$). As the rays are almost collimated at the beam splitter layer (Figure 7.9), this design could also be used but this depends on the angle sensitivity of the dichroic beam splitter.

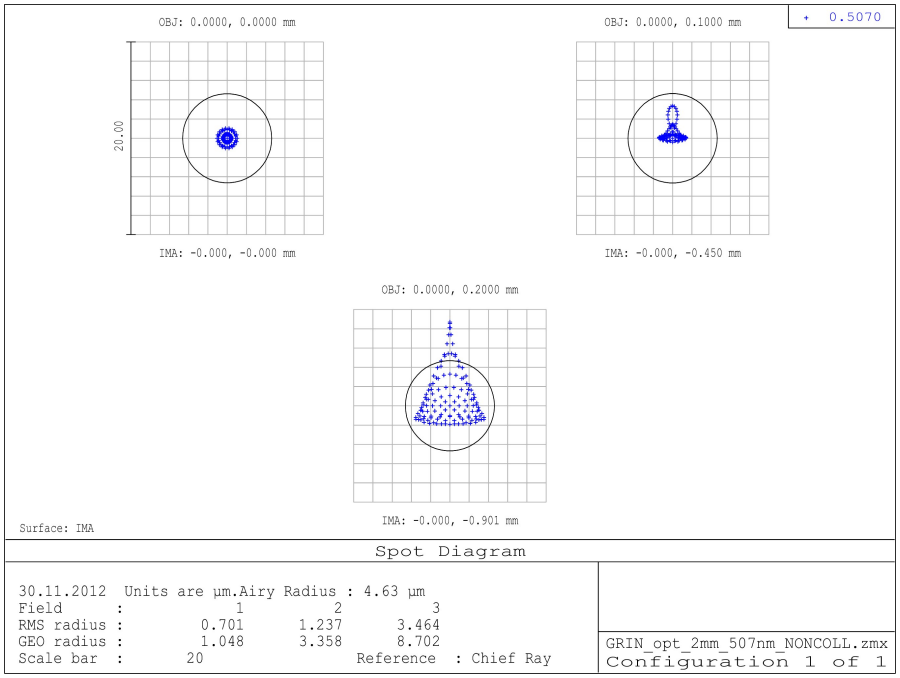

Figure 7.8.: Spot diagram of the imaging path for EGFP (without perfect collimation)

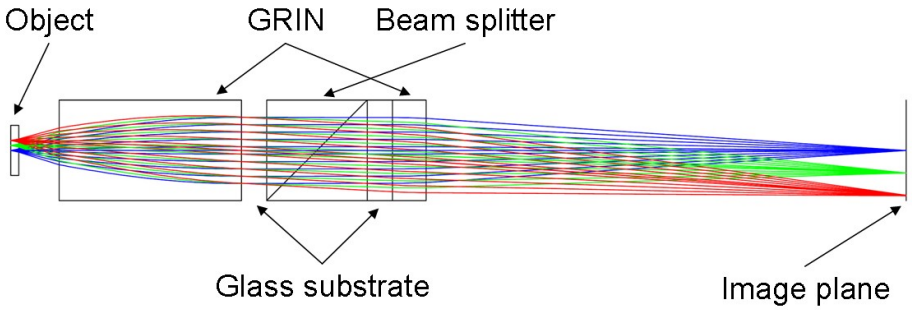

Figure 7.9.: Layout of the imaging path for EGFP (without perfect collimation)

7.5.3. Simulation of the Illumination Path

The illumination path is designed for the fluorophore EGFP, which has its excitation maximum at $488nm$. The field of view, which has to be illuminated, has a diameter of $400\mu m$. Figure 7.10 shows the illumination path from the light source to the object plane.

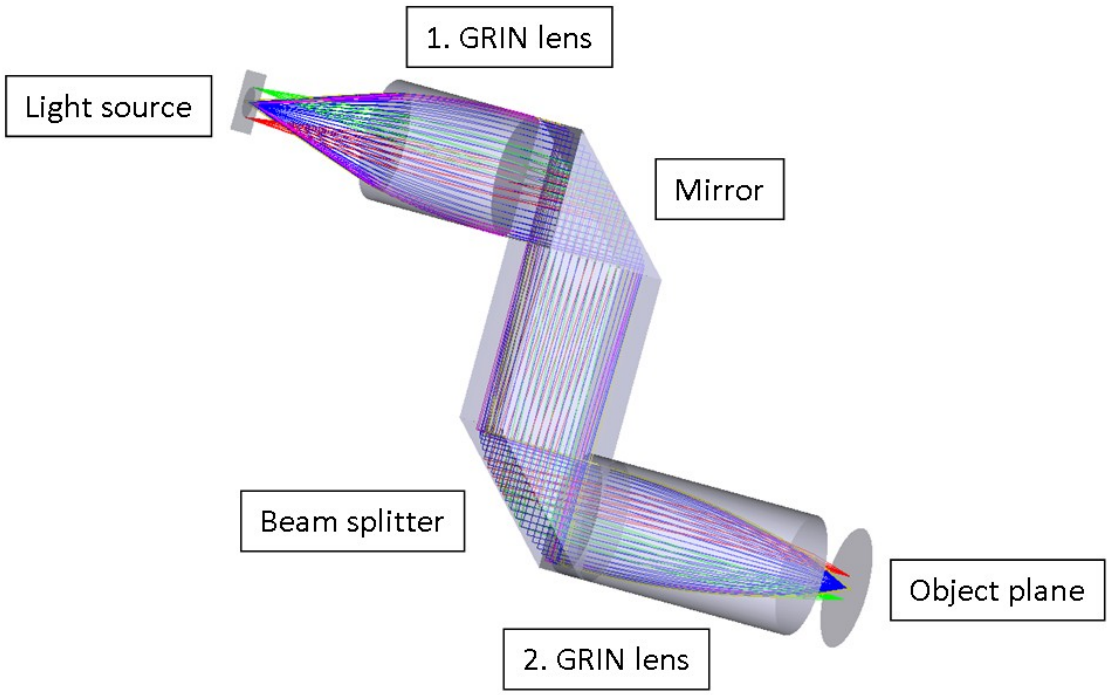

Figure 7.10.: Layout of the illumination path

As a light source a square Lambertian radiator with a length of the edge of $0.5mm$, a wavelength of $488nm$ and a power of $1mW$ is used.

The optimization goals are homogeneous illumination and low energy loss. An additional constraint is that the light has to be almost collimated in the beam splitter layer. The optimization parameters are the length of the first GRIN lens and the distance of the light source. The GRIN lens on the object side is specified by the imaging path. After the optimization the length of the GRIN lens is $2.369mm$. The optimized distance of the light source is $2.427mm$.

Figure 7.11 depicts the simulated intensity distribution in the object plane. Considering the reflection and transmission loss, the energy efficiency is about 33%.

Due to the light source's characteristics, a homogeneous illumination of the field of view can only be reached by using additional optical components. The main part of the energy loss is produced by the beam splitter, which is essential for combining the

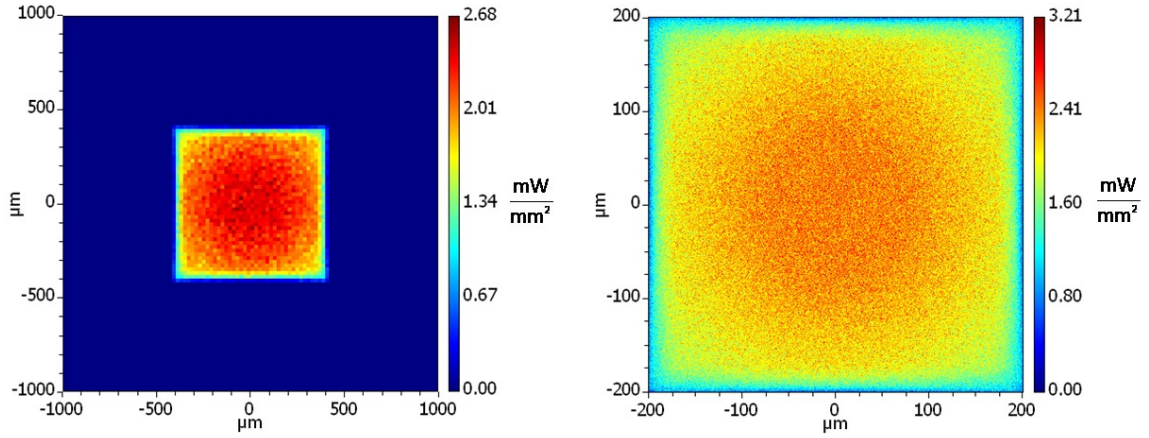

(a) Object plane

(b) Detail view of the field of view

Figure 7.11.: Intensity distribution

illumination and imaging paths. Nevertheless an energy efficiency of about 33% can be reached, which is enough to realize an illumination system using LEDs with high optical output power.

7.5.4. Chromatic Aberrations

GRIN lens systems are strongly sensitive to wavelength changes as the wavelength spectrum which can be used to obtain an acceptable image quality is smaller than $10nm$ [Wohlfeld 2009]. This is caused by the wavelength dependency of the refractive index (dispersion). Therefore it is essential to add chromatic correction to the system. To minimize the chromatic aberrations of the GRIN lens system, a diffractive optical element is suggested [Wohlfeld 2009].

7.5.5. Beam Splitter Layer

A negative master (Figure 7.12(a)) made of $AlMg_3$ is used to replicate the beam splitter in an UV-curable polymer (Figure 7.12(b)). The design, properties and manufacturing process for the beam splitter layer is described in [Wohlfeld 2009].

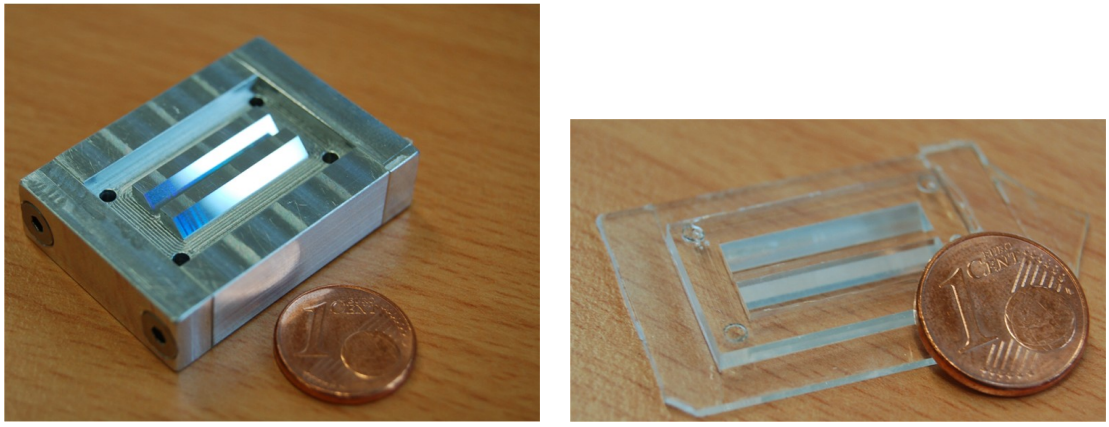

(a) Metal master (b) Replication

Figure 7.12.: Beam splitter layer

8. Demonstrator

8.1. Introduction

In order to analyze the image quality and the assembly of the layers, a demonstrator for the imaging path was set up. In this chapter the design of the demonstrator is illustrated and simulation results of the optical system are shown. This is followed by the description of the assembly as well as the experimental setup and the experimental results.

8.2. Design

8.2.1. Wavelength

The demonstrator is designed for the fluorophore DAPI, which has its emission peak wavelength at $461nm$. Due to the fact that chromatic aberrations are not corrected in this design, a monochromatic light source is needed to get exploitable data from the experimental setup. Therefore the wavelength used in the simulation was set to $473nm$, which is the wavelength of available lasers and is close enough to the emission peak of DAPI.

8.2.2. Geometry

The geometry of the demonstrator is chosen in such a way, that a maximum count of objectives can be tested. The constraints for this are the minimum side length of the camera sensor S_{min}, the diameter of the GRIN rod lenses D_L, the spacing between the optical axes of the GRIN rod lenses d_L, the magnification of the optical system m and the size of the field of view FOV. The count of objectives N is calculated as follows:

$$N = \left\lfloor \frac{S + D_L - d_L}{mFOV + d_L - D_L} \right\rfloor \tag{8.1}$$

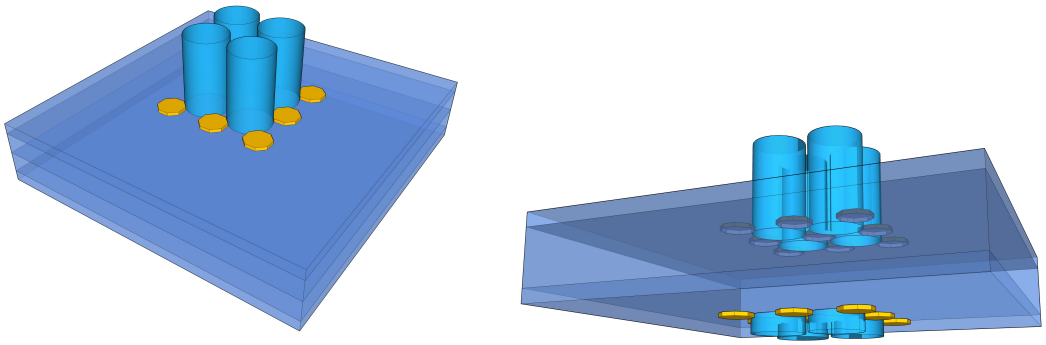

(a) Object side (b) Image side

Figure 8.1.: Optical system of the demonstrator

Assuming that $d_L = D_L$, which means that there is no spacing between the GRIN rod lenses, the maximum count of objectives N_{max}, which can be tested is:

$$N_{max} = \left\lfloor \frac{S}{mFOV} \right\rfloor \tag{8.2}$$

With a given camera and a given optical system, the only free parameter is the spacing between the optical axes d_L. As a larger distance is favorable for the assembly and gives the opportunity to have larger and therefore more stable holding structures, Equation 8.1 is solved for the maximum allowed distance d_L and N is substituted by the previously calculated N_{max}:

$$d_{L,max} = \frac{S - N_{max}\,(mFOV)}{N_{max} - 1} + D_L$$

The camera sensor's minimum side length is $S = 4,28mm$, the diameter of the GRIN rod lenses $D_L = 2mm$, the magnification $m = 4.29$ and the size of the field of view $0.4mm$. With these specifications N_{max} is 2 and $d_{L,max}$ is $2.848mm$. A d_L of $2.25mm$ is chosen to have tolerance in the setup. The side length of the glass substrates is chosen to $14.6mm$.

8.3. Simulations

Two optical systems were simulated. One with optimized manufacturing parameters of the GRIN rod lenses, including an aperture on the back face of the first GRIN rod lens, and a second with off-the-shelf GRIN rod lenses. As the optimized GRIN rod lenses with apertures are only available when ordering them in large amounts, the second simulated system was realized in the experimental setup.

For both simulations the arrangement of the single components is the same as in 7.5.2. For the substrates holding the GRIN lenses glass AF32 from the company Schott is used. The glass substituting the beam splitter is B270 from Schott, which features almost the

same refractive index at this wavelength as the polymer which is used to fabricate the beam splitter [Wohlfeld 2009].

8.3.1. The Optimized Optical System

The layout of the optimized system is shown in Figure 8.2.

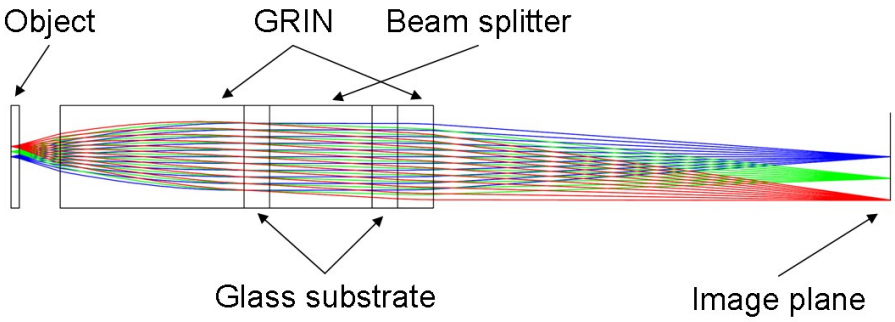

Figure 8.2.: Layout of the optimized system

To simulate an aperture behind the first GRIN lens, the object side NA is set to 0.3. The optimization goal is a small root-mean-square value of the spot radius and a magnification of 4.25. The optimization parameters are the length of the GRIN lenses, their manufacturing parameters nr_4 and the distance between the second GRIN lens and the image plane. After the optimization the length of the first GRIN lens is $3.592mm$ and its manufacturing parameter nr_4 is 0.00237. The resulting parameters of the second GRIN lens are for the length $0.700mm$ and for nr_4 0.00645. The distance to the image plane is $8.93mm$. In this simulation both GRIN lenses were optimized with regard to the image quality, thus the light in the beam splitter is not perfectly collimated.

The simulation of an objective with optimized manufacturing parameters and an aperture behind the first GRIN rod lens shows diffraction limited spots even at the border of the image plane (Figure 8.3). The root-mean-square value of the spot radius at the border is $3.260\mu m$ which is below the airy radius of $4.08\mu m$.

8.3.2. The Realized Optical System

The layout of the realized system is shown in Figure 8.4. It does not have an aperture behind the first GRIN rod lens and the manufacturing parameter nr_4 is not optimized. The simulation was performed by Robert Buschlinger [Buschlinger 2010] in three steps. The first two steps are the same as described in 7.5.2. Due to the manufacturing accuracy of the GRIN lenses their lengths are rounded to the second decimal place after the first two steps and an optimization concerning the root-mean-square value of the spot radius

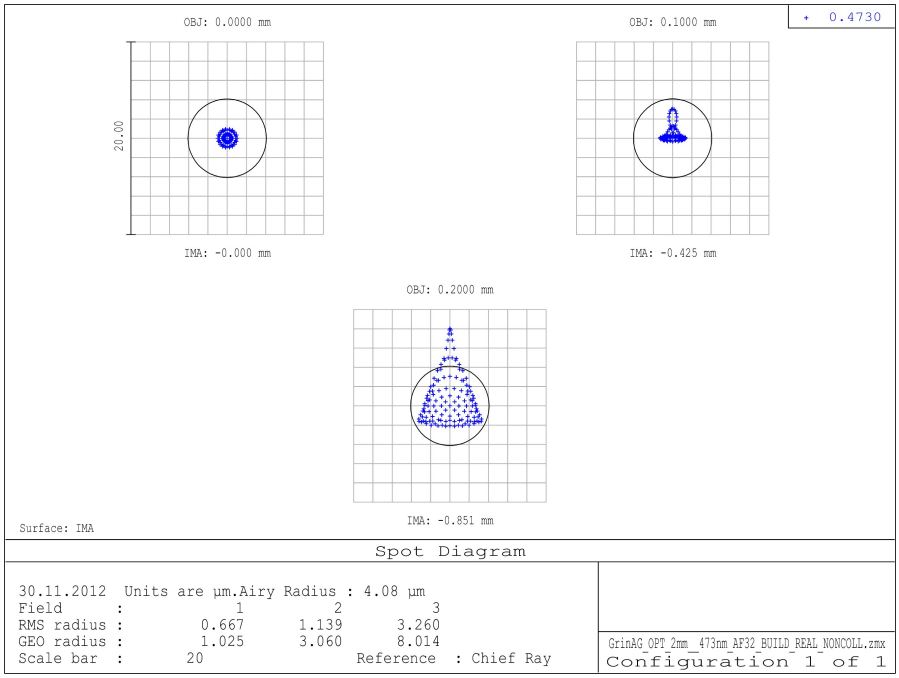

Figure 8.3.: Spot diagram of the optimized system

is performed again. The optimization parameters are now the object and the image distances. The length of the first GRIN lens is $3.58mm$ and of the second GRIN lens $0.70mm$. The optimized distance of the image plane is $8.863mm$ and the distance of the object plane is $0.807mm$. The resulting NA in the object space of this system is 0.44 and the magnification 4.29.

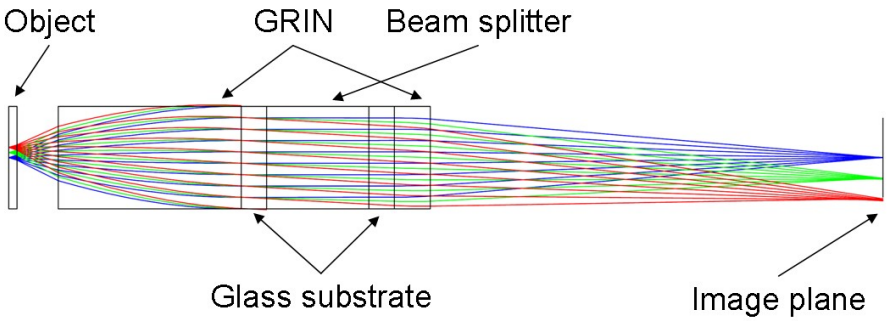

Figure 8.4.: Layout of the realized system

The spot diagram of the realized system is depicted in Figure 8.5. The diffraction limit of the system (airy radius) is $2.662\mu m$. While the spot diagram shows a diffraction limited root-mean-square value of the spot radius of $0.992\mu m$ at the optical axis, the root-mean-square value of the spot radius at the border of the field of view is only $24.973\mu m$.

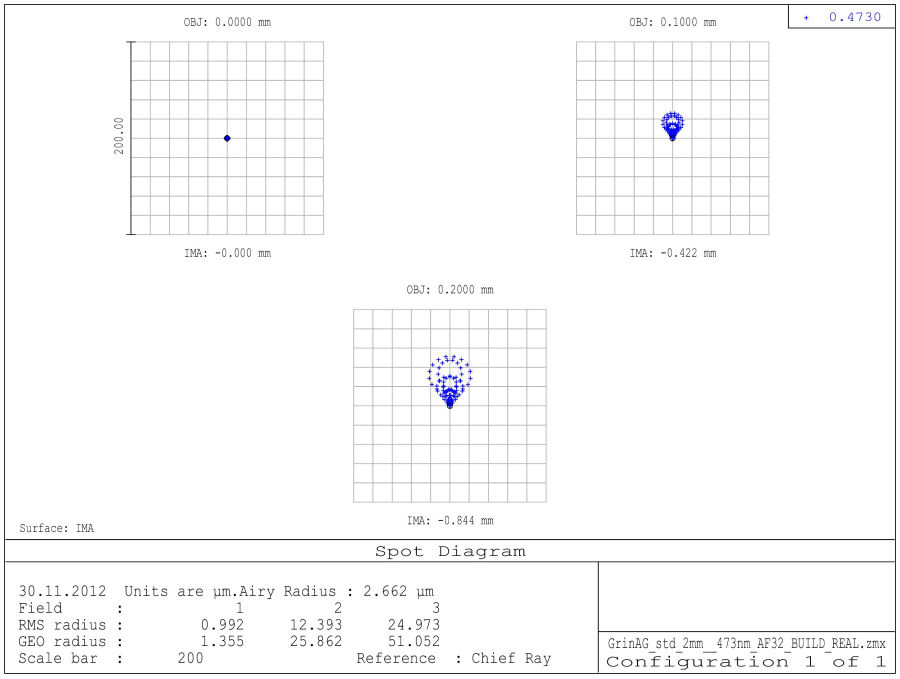

Figure 8.5.: Spot diagram of the realized system

8.4. Assembly of the Optical System

The assembly of the demonstrator's optical system poses mainly two critical challenges: The fixation of the GRIN rod lenses on the glass substrate and the alignment of the layers.

8.4.1. Fixation of the GRIN Rod Lenses

The holding structures for the GRIN rod lenses are octagons made from photoresist SU-8. A software tool was written to generate masks for the holding structures on both sides of the optical system. The tool takes into account all the different parameters such as number of lens systems in both lateral directions, the sizes of the components and the distance between mirror and beam splitter. Figure 8.6 shows the mask used to fabricate the SU-8 structures for the demonstrator on a glass substrate. The diameter of the space between the holding structures is designed larger by $40\mu m$ than the diameter of the GRIN lenses in order to balance deviations of the GRIN lens diameter and deviations of the holding structures due to thermal shrinking or expanding.

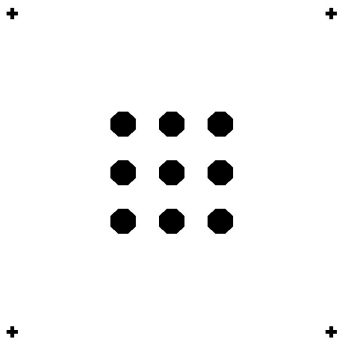

Figure 8.6.: Mask for the GRIN rod lenses' holding structure

The detailed manufacturing process including the preparation of the substrate, the process parameters of the lithography and the development of the photoresist are described in [Buschlinger 2010]. The GRIN rod lenses are fixed with an UV-curable adhesive. In a first step the GRIN rod lenses are put in place on the holding structures, which are self-aligning due to their form and arrangement. In the second step the adhesive is applied at one side of the GRIN rod lens. As the adhesive has a high viscosity, it then flows underneath the GRIN rod lens, building a thin film. This has the advantage that there is an index matching between GRIN rod lens and substrate and it is assured that there is no air in between them. As the adhesive is now part of the optical system, it must have optical quality. The used adhesive NOA 61 from the company Norland was developed to glue optical components together and features over 90% transmission between $350nm$

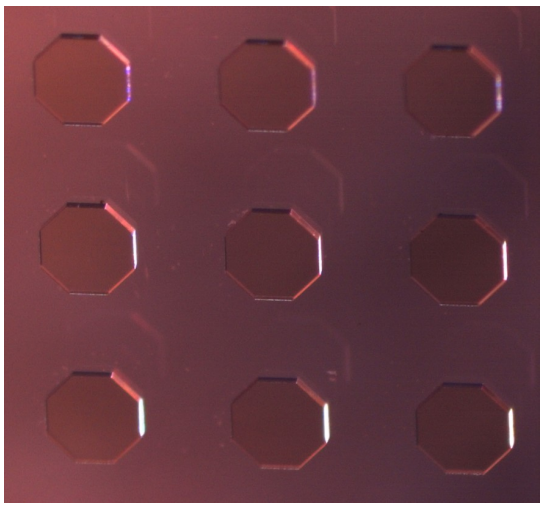

Figure 8.7.: Holding structure for the GRIN rod lenses

and 2000nm wavelenght [Norland Products Incorporated 2012]. Figure 8.8 shows the holding structures with the fixed GRIN rod lenses.

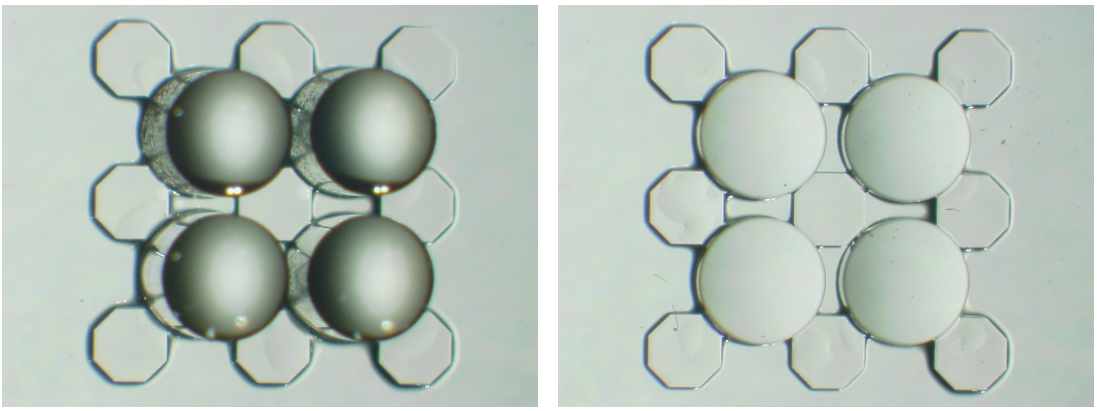

(a) Object side (b) Image side

Figure 8.8.: GRIN rod lenses with SU-8 holding structures, fixed with NOA 61

8.4.2. Alignment of the Layers

The optical system consists of three layers: one glass substrate with fixed GRIN rod lenses for the object side, the beam splitter substitute and a glass substrate with fixed GRIN rod lenses on the image side. The glass substrates with the GRIN rod lenses must be aligned precisely so that both optical axes coincide. To ensure this, cut marks are added in the mask for the lithographic process with SU-8, which gives a precise alignment of the GRIN rod lenses and the edge of the glass substrate. The glass substrates are then cut at the cut marks with a programmable wafer saw. Now the alignment of the layers

is accomplished by a holder, manufactured with high precision, which ensures that the edges of the substrates are in the same plane without rotation. To make the insertion of the glass substrate into the holder possible, the corners are cut off with a manual driven wafer saw. This has no influence on the alignment precision. Figure 8.9 shows the holder with the inserted layers. To achieve the proper object distance a spacer is inserted on top of the glass substrate on the object size, on which the test images are positioned (Figure 8.9(a)).

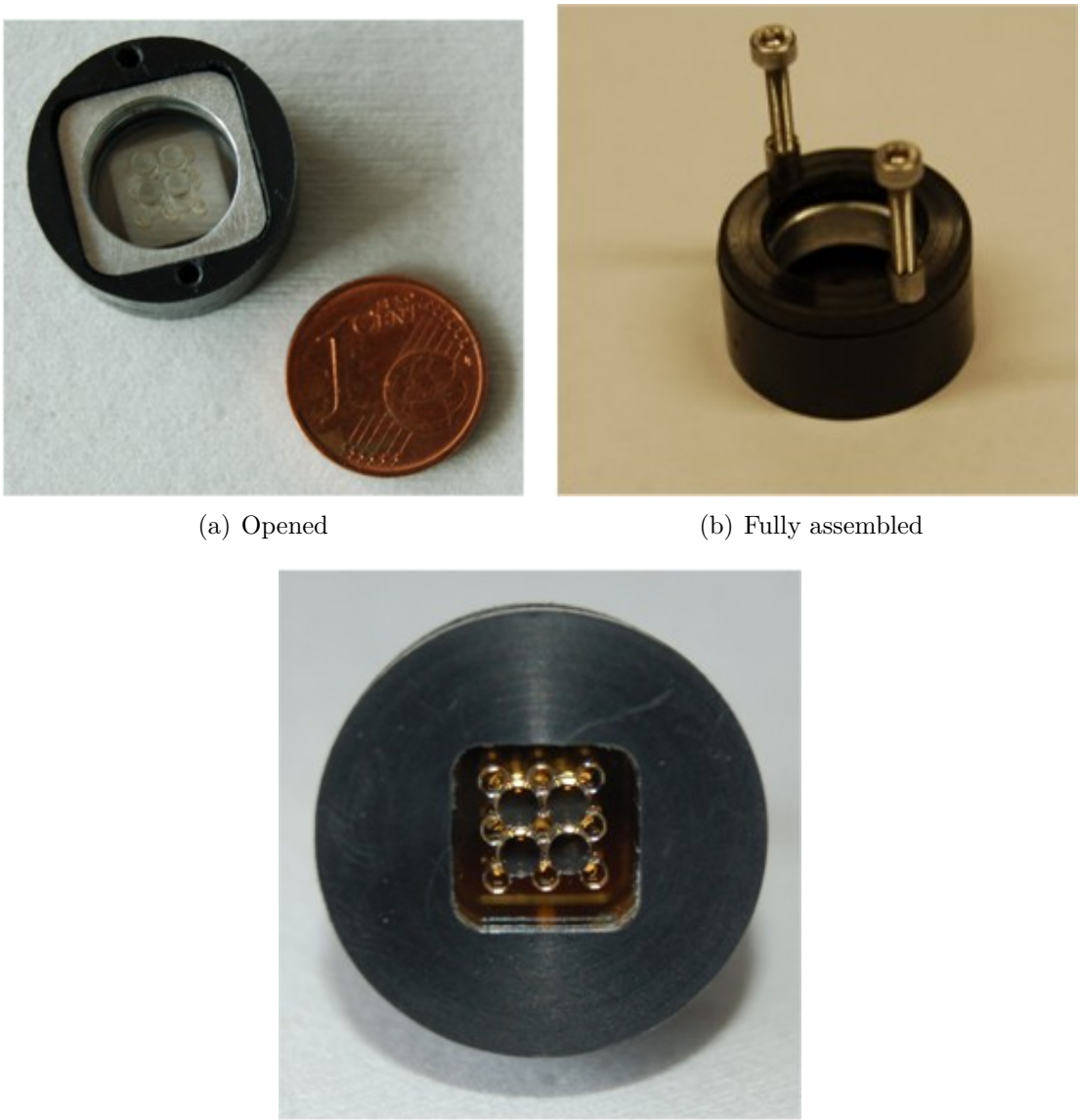

(a) Opened

(b) Fully assembled

(c) Fully assembled, image side

Figure 8.9.: Holder for the optical system

8.4.3. Experimental Setup

The optical system in its holder is mounted on a camera with a modified Linos Microbench component providing a C-MOUNT connector (Figure 8.10). The camera which is used in this setup is the monochrome camera Guppy from the company Allied Vision Technologies. It features a CMOS-sensor with a pixel size of $2.2\mu m$ x $2.2\mu m$. As the magnification of the optical system is 4.29 and in consideration of the Nyquist–Shannon sampling theorem, object features down to almost $1\mu m$ can be resolved. The illumina-

Figure 8.10.: Camera with mounted holder

tion of the test images is done by using a laser pointer with a wavelength of $473nm$, whose beam is expanded by a microscope objective lens.

The experimental setup is shown in Figure 8.11.

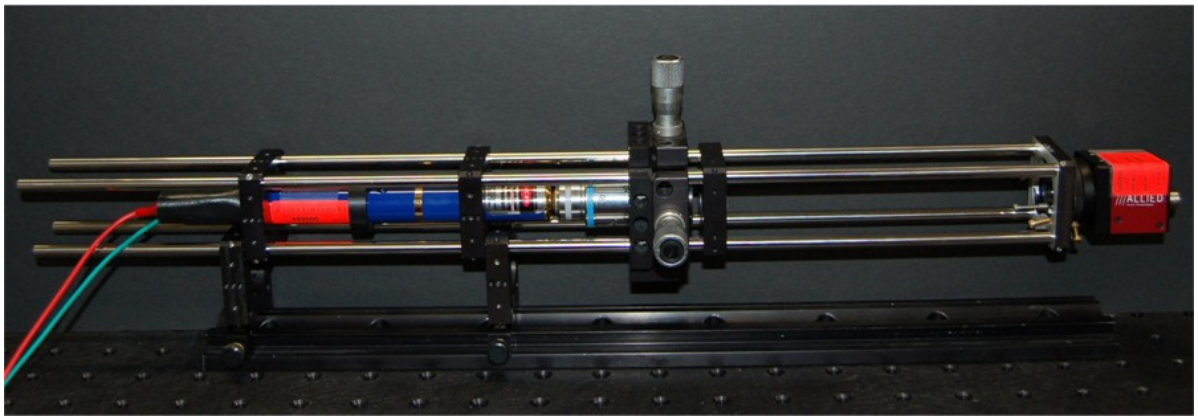

Figure 8.11.: Experimental setup of the demonstrator

8.5. Experimental Results

Chrome masks with different patterns are used as test images for the demonstrator. One mask consists of four equal test patterns with a diameter of $400\mu m$ (size of the field of view), each centered at the optical axis of one objective. In order to get an impression of the reachable image quality, the patterns were also propagated through the system in Zemax.

The test patterns are:

- Dot pattern with $25\mu m$ period and a diameter of $10\mu m$ (Figure 8.12)
- Grid with $25\mu m$ period and $2\mu m$ line width (Figure 8.13)
- Grid with $12.5\mu m$ period and $2\mu m$ line width (Figure 8.14)
- Lines with $8\mu m$ period and $4\mu m$ line width (Figure 8.15)

The inhomogeneities have their origin in the light distribution of the laser pointer used. The images show a good agreement between the simulation and the experiment. As expected, the finest test structures – line pairs with $8\mu m$ period and $4\mu m$ line width – are resolved precisely. This correlates to $125\frac{linepairs}{mm}$ in object space. When comparing the images from the demonstrator with the simulated images it can be seen that the demonstrator produces sharper images than the simulation predicts, even at the border of the field of view.

Figure 8.16 shows the complete camera image with the images of the four objectives. The single structures are overlapping. One reason for this is that the GRIN lenses are not planar on the substrate so that they are tilted. This problem can be resolved by making the holding structures thicker. Another reason is a lateral offset resulting from the $40\mu m$ tolerance at the space between the holding structures. And the third reason is the small object distance. Slight deviations of this distance result in deviations of the image distance, which then cause a change in the magnification as it can be seen in Figure 8.16.

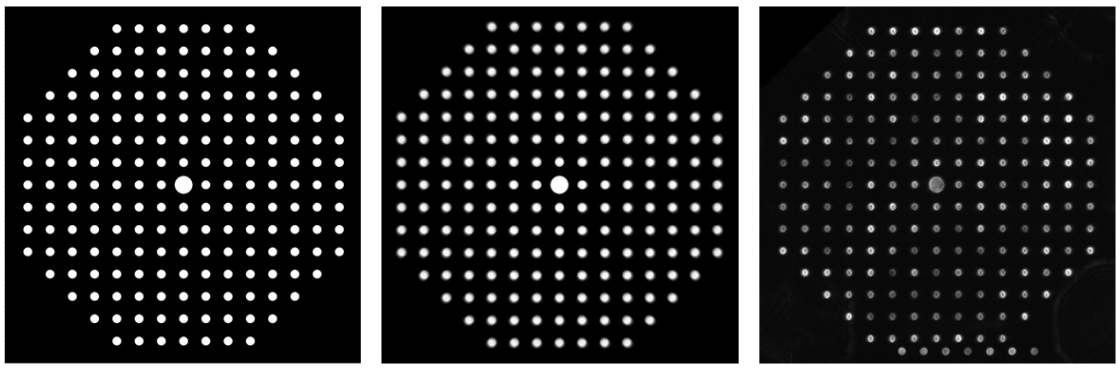

(a) Original (b) Simulation (c) Demonstrator

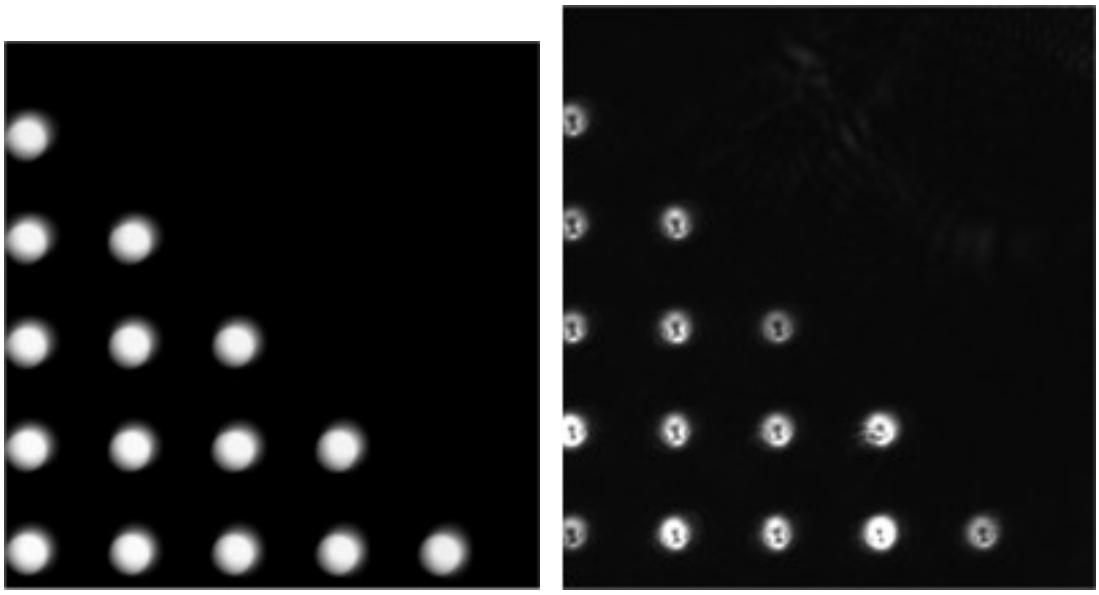

(d) Simulation (Detail) (e) Demonstrator (Detail)

Figure 8.12.: Dots with $25\mu m$ period and $10\mu m$ diameter

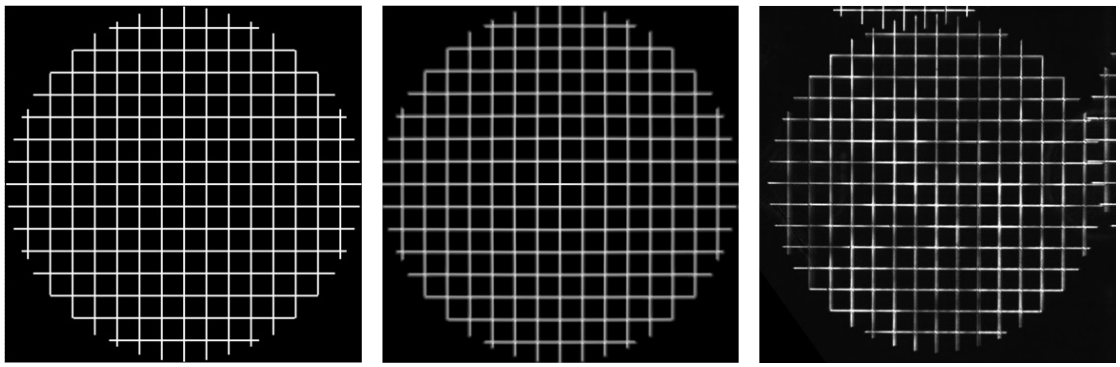

(a) Original (b) Simulation (c) Demonstrator

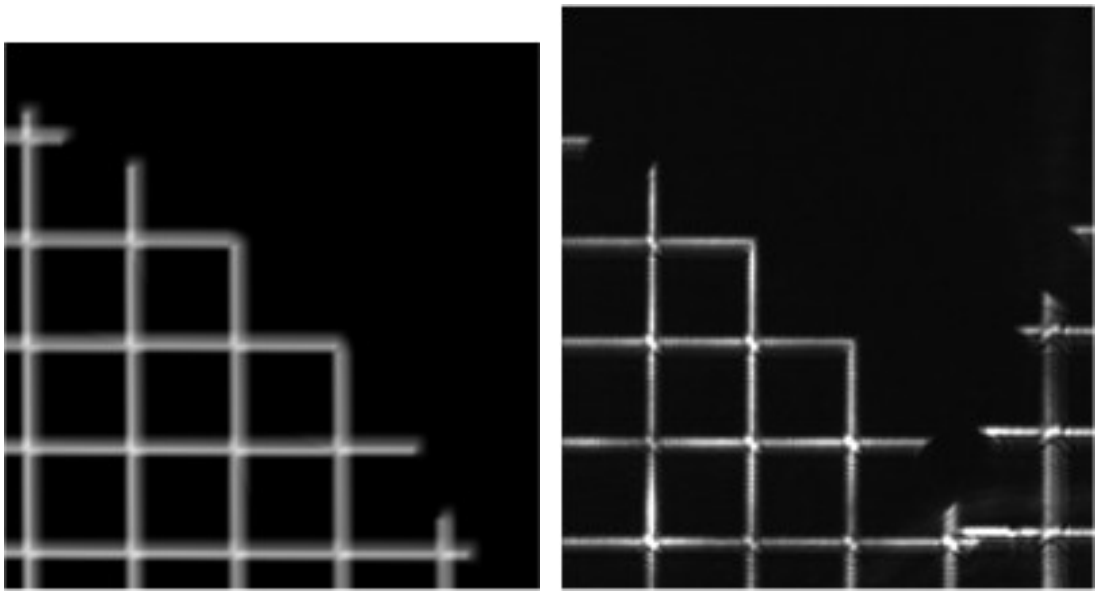

(d) Simulation (Detail) (e) Demonstrator (Detail)

Figure 8.13.: Grid with $25\mu m$ period and $2\mu m$ line width

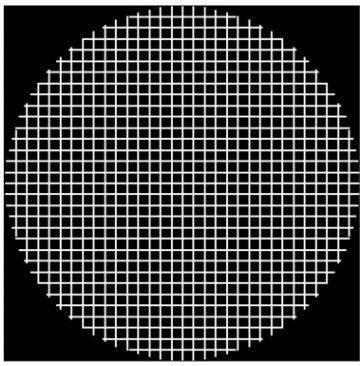

(a) Original

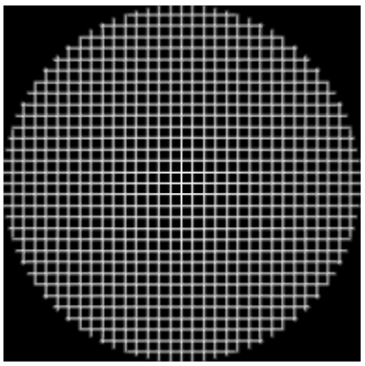

(b) Simulation

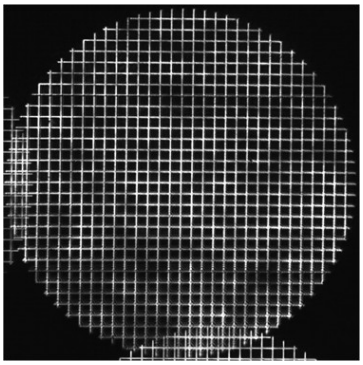

(c) Demonstrator

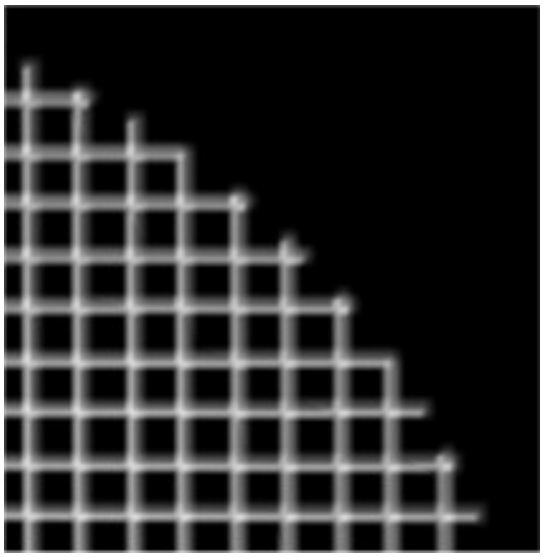

(d) Simulation (Detail)

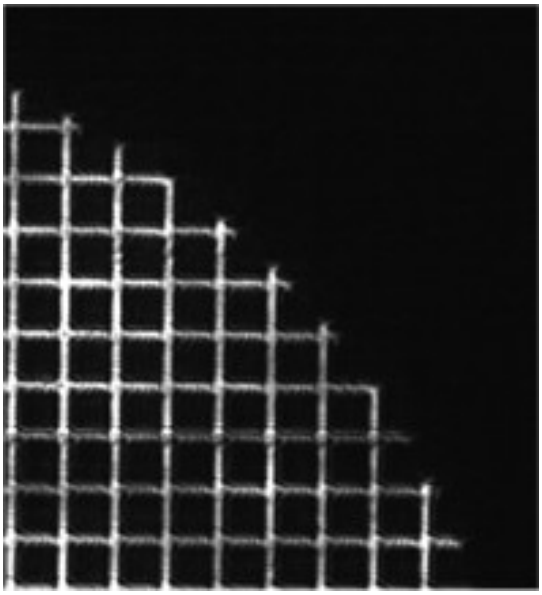

(e) Demonstrator (Detail)

Figure 8.14.: Grid with $12.5\mu m$ period and $2\mu m$ line width

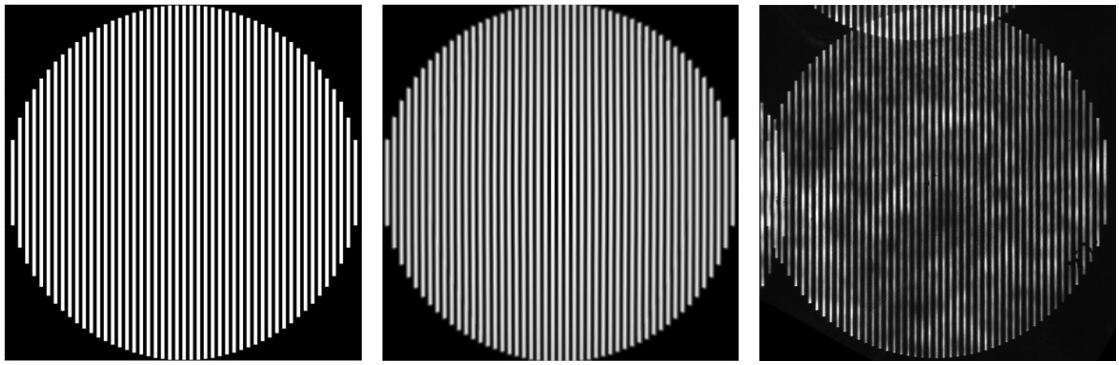

(a) Original (b) Simulation (c) Demonstrator

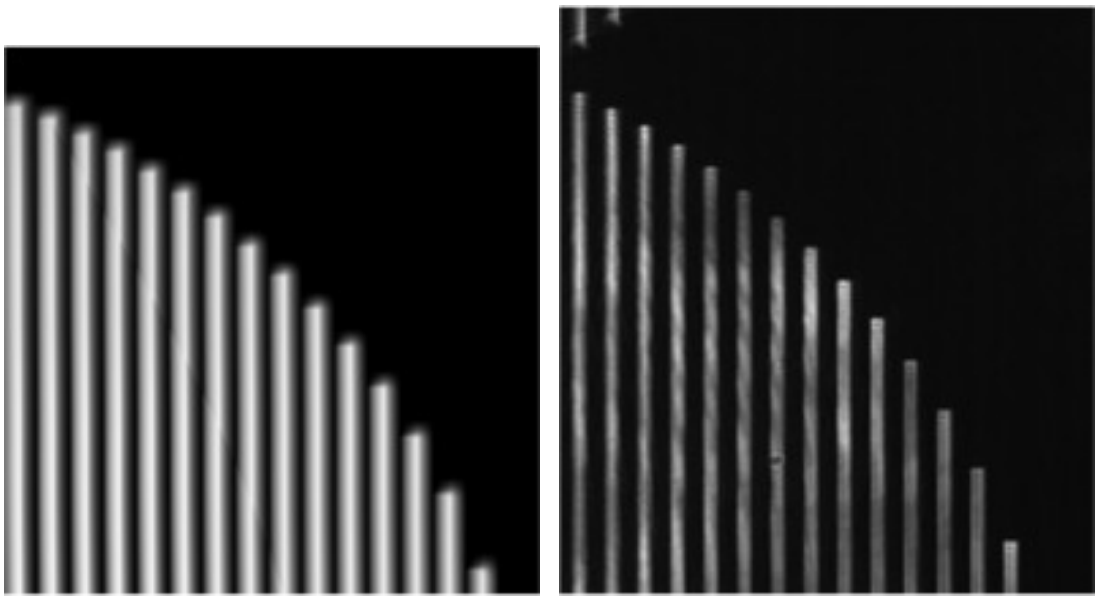

(d) Simulation (Detail) (e) Demonstrator (Detail)

Figure 8.15.: Lines with $8\mu m$ period and $4\mu m$ line width

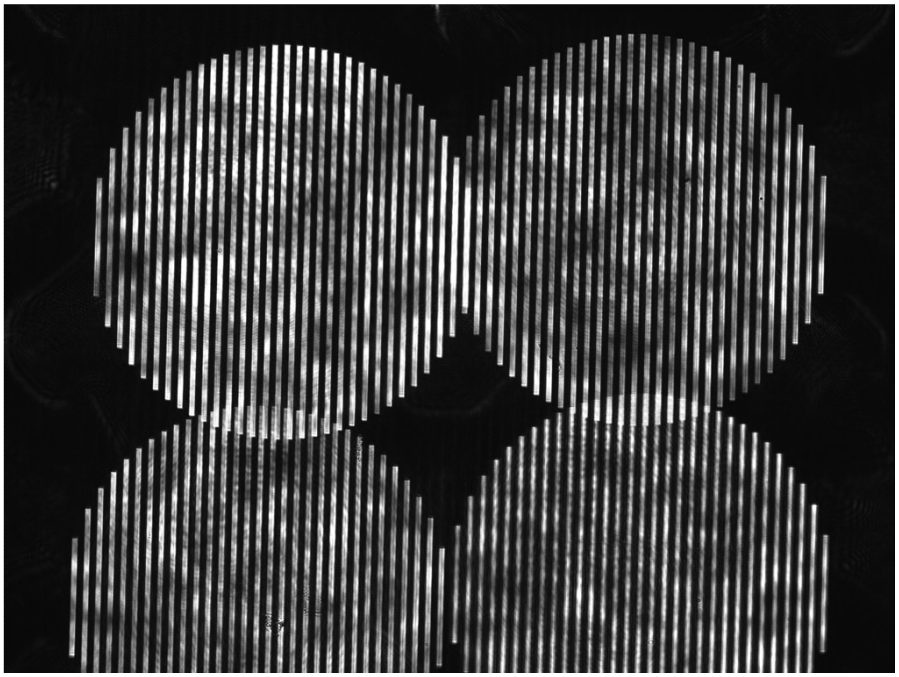

Figure 8.16.: Complete camera image

9. Summary

The concept of the highly miniaturized parallel fluorescence microscope, which is presented here, has a great potential to speed up the image acquisition. Since GRIN rod lenses, which have flat end faces, are used as imaging components the integration and assembly is simplified compared to micro lenses. Due to the small sizes of the GRIN rod objectives, a high packing density can be achieved, which makes the image acquisition of a whole substrate in one scan possible.

The simulations show that a diffraction limited design with GRIN rod lenses can be achieved, when both GRIN rod lenses are optimized for the image quality. Then the light at the beam splitter is not perfectly but almost sufficiently collimated. This design can be used, if the tolerances of the beam splitter with regard to the incident angle match the collimation quality in the design.

With the implementation of the demonstrator it was proven that the image quality is sufficient to detect interesting features, which can then be studied in detail with higher resolution microscopes. The integration of a chromatic aberration correcting element is essential, as other options like inserting an aperture to increase the depth of focus or a narrow bandpass filter are accompanied by a huge loss of intensity.

Conclusion

In this thesis three approaches to significantly speed up the image acquisition in fluorescence microscopy are presented. With the elimination of the focus search by a deflectometric measurement of the substrate's height distribution, the main bottleneck in the image acquisition of the existing microscopy with standard automated wide-field microscopes is overcome. The measurement of the height distribution can be carried out in a step before the microscopy so that an automated workflow chain can be built, where the height deviations of one substrate is measured while the previous measured substrate is observed in the microscope.

The microscopy system with macro-optical standard components increases the image acquisition rate by using two domains of parallelization. The virtue of the spatial parallelization is evident. The spectral parallelization, which means the possibility of observing four different fluorophores at the exact same point in time, decreases the observation time as no filter wheel movements are necessary and the exposure times are not summed up as it usually happens in the standard automated microscopes and fluorescence slide scanners [Hamamatsu 2010]. The synchrony of the image acquisition of the four channels is a benefit, especially when performing screens with living cells. Due to the highly optimized standard objectives in this system the image quality is the same as with the standard microscopes.

Scanning microscopy with a high degree of spatial parallelization using an array of micro-optical objectives offers the largest potential of the presented approaches, as it makes the image acquisition of a whole substrate possible within seconds. The presented design with GRIN rod lenses as objectives can be implemented for different fluorophores and then be combined in one setup to feature almost the same broad spectrum of usable fluorophores as it is available with standard fluorescence microscopes.

Bibliography

Abbyad, Paul, William Childs, Xinghua Shi, and Steven G. Boxer (2007). "Dynamic Stokes shift in green fluorescent protein variants". In: *Proceedings of the National Academy of Sciences* 104.51, pp. 20189–20194.

Biostatus Limited. *DRAQ5™ spectral profile*. URL: `http://www.biostatus.com/product/draq5/spectral_profile/` (visited on 11/19/2012).

Brenner, Karl-Heinz (2007). *Grundlagen der Optik*. Lecture notes.

– (2008). "Shifted Base Functions: An Efficient and Versatile New Tool in Optics". In: *Journal of Physics: Conference Series* 139.1, p. 012002.

– (2012). *Computational Optics*. Lecture notes.

Bronstein, I. N., K. A. Semendjajew, G. Musiol, and H. Mühlig (1999). *Taschenbuch der Mathematik*. fourth. Verlag Harri Deutsch.

Buschlinger, Robert (2010). "Untersuchungen zur miniaturisierten Mikroskopie für die Systembiologie". MA thesis. University of Heidelberg.

Campbell, Robert E., Oded Tour, Amy E. Palmer, Paul A. Steinbach, Geoffrey S. Baird, David A. Zacharias, and Roger Y. Tsien (2002). "A monomeric red fluorescent protein". In: *Proceedings of the National Academy of Sciences* 99 (12), pp. 7877–7882.

Day, Richard N. and Michael W. Davidson (2009). "The fluorescent protein palette: tools for cellular imaging". In: *Chem. Soc. Rev.* 38 (10), pp. 2887–2921.

Egner, Alexander, Stefan Jakobs, and Stefan W. Hell (2002). "Fast 100-nm resolution three-dimensional microscope reveals structural plasticity of mitochondria in live yeast". In: *Proceedings of the National Academy of Sciences* 99.6, pp. 3370–3375.

Hamamatsu (2010). *Multichannel and Multicolor Fluorescence Module for Tissue Imaging*. Product Brochure.

Hell, Stefan and Ernst H. K. Stelzer (Dec. 1992). "Properties of a 4Pi confocal fluorescence microscope". In: *J. Opt. Soc. Am. A* 9.12, pp. 2159–2166.

Invitrogen (2006). *DAPI Nucleic Acid Stain*.

Kapuscinski, Jan (1995). "DAPI: a DMA-Specific Fluorescent Probe". In: *Biotechnic & Histochemistry* 70.5, pp. 220–233.

Klar, Thomas A., Egbert Engel, and Stefan W. Hell (Nov. 2001). "Breaking Abbe's diffraction resolution limit in fluorescence microscopy with stimulated emission depletion beams of various shapes". In: *Phys. Rev. E* 64 (6), p. 066613.

Knauer, Markus Christian, Jürgen Kaminski, and Gerd Häusler (2004). "Phase measuring deflectometry: a new approach to measure specular free-form surfaces". In: *Proc. SPIE*. Vol. 5457, pp. 366–376.

Latt, Samuel A. and James C. Wohlleb (1975). "Optical studies of the interaction of 33258 Hoechst with DNA, chromatin, and metaphase chromosomes". In: *Chromosoma* 52 (4), pp. 297–316. ISSN: 0009-5915.

Lohmann, Adolf W. (1989). "Scaling laws for lens systems". In: *Appl. Optics* 28, pp. 4996–4998.

Meschede, Dieter, ed. (2006). *Gerthsen Physik*. 23rd ed. Springer-Lehrbuch. Springer.

microscopel objective/lens positioning system MIPOS500 (2011). Piezosysteme Jena.

MP79E User Manual (2007). Physik Instrumente.

MP81E User Manual (2007). Physik Instrumente.

Neumann, B, M Held, U Liebel, H Erfle, P Rogers, R Pepperkok, and J Ellenberg (2006). "High-throughput RNAi screening by time-lapse imaging of live human cells". In: *Nature Methods* 3.5, pp. 385–90.

Njoh, Kerenza L., Laurence H. Patterson, Mire Zloh, Marie Wiltshire, Janet Fisher, Sally Chappell, Simon Ameer-Beg, Yanhong Bai, Daniel Matthews, Rachel J. Errington, and Paul J. Smith (2006). "Spectral analysis of the DNA targeting bisalkylaminoanthraquinone DRAQ5 in intact living cells". In: *Cytometry Part A* 69A.8, pp. 805–814. ISSN: 1552-4930.

Norland Products Incorporated. *Norland optical adhesive 61*. URL: `https://www.norlandprod.com/adhesives/noa%2061.html` (visited on 12/02/2012).

Olszak, Artur G. and Chen Liang (Jan. 2011). *Multi-spectral whole-slide scanner*. United States Patent No. US7864379.

Schmidt, Roman, Christian A Wurm, Stefan Jakobs, Johann Engelhardt, Alexander Egner, and Stefan W Hell (2008). "Spherical nanosized focal spot unravels the interior of cells". In: *Nature Methods* 5.6, pp. 539–544.

Seßner, Rainer and Gerd Häusler (2004). "Richtungscodierte Deflektometrie (RCD)". In: *DGaO-Proceedings 2004, ISSN: 1614-8436*.

Shaner, Nathan C, Robert E Campbell, Paul A Steinbach, Ben N G Giepmans, Amy E Palmer, and Roger Y Tsien (2004). "Improved monomeric red, orange and yellow fluorescent proteins derived from Discosoma sp. red fluorescent protein". In: *Nature Biotechnology* 22 (12), pp. 1567–1572.

Simpson, Jeremy C., Cihan Cetin, Holger Erfle, Brigitte Joggerst, Urban Liebel, Jan Ellenberg, and Rainer Pepperkok (2007). "An RNAi screening platform to identify secretion machinery in mammalian cells". In: *Journal of Biotechnology* 129.2, pp. 352–365.

Simpson, Jeremy C., Brigitte Joggerst, Vibor Laketa, Fatima Verissimo, Cihan Cetin, Holger Erfle, Mariana G. Bexiga, Vasanth R. Singan, Jean-Karim Heriche, Beate Neumann, Alvaro Mateos, Jonathon Blake, Stephanie Bechtel, Vladimir Benes, Stefan Wiemann, Jan Ellenberg, and Rainer Pepperkok (2012). "Genome-wide RNAi screening identifies human proteins with a regulatory function in the early secretory pathway". In: *Nature Cell Biology* 14.7, pp. 764–774.

Smith, Paul J, Marie Wiltshire, Sharon Davies, Laurence H Patterson, and Terence Hoy (1999). "A novel cell permeant and far red-fluorescing DNA probe, DRAQ5, for blood cell discrimination by flow cytometry". In: *Journal of Immunological Methods* 229.1–2, pp. 131–139.

User's manual for GigE vision cameras (2011). Basler.

Wohlfeld, Denis (2009). "Simulation, Analysis, and Fabrication of Miniaturized Components with Applications in Optical Interconnects and Parallel Microscopy". PhD thesis. University of Heidelberg.

Wohlfeld, Denis, Eike Slogsnat, and Karl-Heinz Brenner (2009). "Integrated beam splitters for parallel microscopy in life science". In: *DGaO-Proceedings 2009, ISSN: 1614-8436*.

Wolf, David E. (2007). "Fundamentals of Fluorescence and Fluorescence Microscopy". In: *Digital Microscopy, 3rd Edition*. Ed. by Greenfield Sluder and David E. Wolf. Vol. 81. Methods in Cell Biology. Academic Press, pp. 63–91.

Yuste, Rafael (2005). "Fluorescence microscopy today". In: *Nature Methods* 2.12, pp. 902–904.

Zhang, Zhengyou (2000). "A flexible new technique for camera calibration". In: *IEEE Transactions on Pattern Analysis and Machine Intelligence* 22.11, pp. 1330–1334.

Acknowledgments

First and foremost, I would like to express my gratitude to my supervisor, Prof. Dr. Karl-Heinz Brenner, for constantly supporting me during my research, for his helpful advice and for the inspiring discussions.

I would like to thank Prof. Dr. Cornelia Denz for the second opinion on my thesis and Prof. Dr. Reinhard Männer for being a member of the examination board.

I thank all my colleagues at the chair for optoelectronics for the productive discussions and the relaxed atmosphere in which they took place. Additionally, I want to thank Wolfgang Stumpfs for his technical assistance in my experiments and Sabine Volk for her organizational support.

I would also like to thank the group of Nathan Brady, PhD, at the DKFZ in Heidelberg for preparing the cell probes.

About the Author

Eike Slogsnat studied computer engineering at the University of Mannheim and obtained his diploma in 2007. His subjects of study include optoelectronics, hardware design and VLSI design. The title of his diploma thesis is: “Entwurf und Charakterisierung von optischen Mikrostrukturen für die Taktverteilung in integrierten Schaltkreisen”. Following this he began his PhD work at the chair of optoelectronics hold by Prof. Dr. Karl-Heinz Brenner at the University of Mannheim (now University of Heidelberg).

List of Publications

- Eike Slogsnat, Karl-Heinz Brenner [2006]. “Wellenoptische Analyse von Multimode-Wellenleitern Vergleich BPM/WPM”. in: *9. Workshop Optik in der Rechentechnik, ISSN 1437-8507*, pp. 28–34

- Eike Slogsnat, Karl-Heinz Brenner [2008]. “Selbstkonsistentes iteratives Verfahren zur Bestimmung glatter Oberflächen”. In: *DGaO-Proceedings 2008, ISSN: 1614-8436*

- Eike Slogsnat, Karl-Heinz Brenner [2009]. “Non-stereoscopic Method for Deflectometric Measurement of Reflecting Surfaces”. In: *DGaO-Proceedings 2008, ISSN: 1614-8436*

- Denis Wohlfeld, Eike Slogsnat, Karl-Heinz Brenner [2009]. “Integrated beam splitters for parallel microscopy in life science”. In: *DGaO-Proceedings 2009, ISSN: 1614-8436*

- Eike Slogsnat, Robert Buschlinger, Karl-Heinz Brenner [2010]. “Miniaturisierte parallele Mikroskopie in der Systembiologie”. In: *DGaO-Proceedings 2010, ISSN: 1614-8436*

- Eike Slogsnat, Karl-Heinz Brenner [2011]. “Design des Beleuchtungspfads für ein miniaturisiertes paralleles Fluoreszenz-Mikroskop”. In: *DGaO-Proceedings 2011, ISSN: 1614-8436-urn:nbn:de:0287-2011-P001-1*

- Eike Slogsnat, Lars Lehmann, Peter Fischer, Karl-Heinz Brenner [2012]. “Concept and Implementation of a Compact Multi-Channel Fluorescence-Microscope Unit”. In: *DGaO-Proceedings 2012, ISSN: 1614-8436-urn:nbn:de:0287-2012-P002-9*